

DISS. ETH NO. 24216

# **Test-beam measurements and simulation studies of thin pixel sensors for the CLIC vertex detector**

A thesis submitted to attain the degree of

DOCTOR OF SCIENCES of ETH ZURICH

(Dr. sc. ETH Zurich)

presented by

Niloufar Alipour Tehrani

*ing. él. dipl. EPF, EPF Lausanne*

born on 11.08.1989  
citizen of Meyrin (Genève)

accepted on the recommendation of

**Prof. Dr. Günther Dissertori**

**Prof. Dr. Rainer Wallny**

**Dr. Dominik Dannheim**

2017



# Abstract

---

The multi- TeV  $e^+e^-$  Compact Linear Collider (CLIC) is one of the options for a future high-energy collider for the post-LHC era. It would allow for searches of new physics and simultaneously offer the possibility for precision measurements of standard model processes. The physics goals and experimental conditions at CLIC set high precision requirements on the vertex detector made of pixel detectors: a high pointing resolution of  $3\text{ }\mu\text{m}$ , very low mass of  $0.2\% X_0$  per layer,  $10\text{ ns}$  time stamping capability and low power dissipation of  $50\text{ mW/cm}^2$  compatible with air-flow cooling. In this thesis, hybrid assemblies with thin active-edge planar sensors are characterised through calibrations, laboratory and test-beam measurements. Prototypes containing  $50\text{ }\mu\text{m}$  to  $150\text{ }\mu\text{m}$  thin planar silicon sensors bump-bonded to Timepix3 readout ASICs with  $55\text{ }\mu\text{m}$  pitch are characterised in test beams at the CERN SPS in view of their detection efficiency and single-point resolution. A digitiser for AllPix, a GEANT4-based simulation framework, has been developed in order to gain a deeper understanding of the charge deposition spectrum and the charge sharing in such thin sensors. The AllPix framework is also used to simulate the beam telescope and extract its tracking resolution. It is also employed to predict the resolution that can be achieved with future assemblies with thin sensors and smaller pitch. For CLIC, a full coverage of the vertex detector is essential while keeping the material content as low as possible. Seamless tiling of sensors, without the need for overlaps, by the active-edge technology allows for extending the detection capability to the physical edge of the sensor and thereby minimising the inactive regions. Thin-sensor prototypes containing active edges with different configurations are characterised in test-beams in view of the detection performance at the sensor edge. Technology Computer-Aided Design (TCAD) finite-element simulations are implemented to reproduce the fabrication and the operation of such devices. The simulation results are compared to data for different edge terminations.



## Résumé

---

Le Collisionneur Linéaire Compact (CLIC), ou le Compact Linear Collider, est un accélérateur de particules qui permet d'effectuer des collisions entre des électrons et des positrons à des énergies de l'ordre de quelques TeV. Le CLIC, est considéré comme l'une des options qui pourrait être complémentaire aux expériences du LHC pour la découverte de la physique au-delà du modèle standard et de réaliser des mesures plus précises sur le boson de Higgs. Afin d'atteindre les objectifs de découvertes pour CLIC, un détecteur de vertex composé de détecteurs à pixel de haute précision est en cours de développement. Certaines exigences requises par le détecteur de vertex pour CLIC sont: une haute résolution spatiale de  $3\text{ }\mu\text{m}$ , une légère masse de  $0.2\% \text{ }X_0$  par couche de détection, un marquage en temps de  $10\text{ ns}$ , une basse dissipation de puissance de l'ordre de  $50\text{ mW/cm}^2$  et une compatibilité avec un refroidissement à air. Dans cette étude, nous nous concentrons sur les assemblages de détecteur à pixel hybride en silicium à bords minces et actifs qui vont permettre de satisfaire les exigences requises par le détecteur de vertex pour CLIC. Ces assemblages sont caractérisés à travers la calibration et des mesures dans un faisceau de particules à haute énergie du SPS au CERN. Ces prototypes contiennent une couche de détecteur planaire mince avec des épaisseurs qui varient entre  $50\text{ }\mu\text{m}$  et  $150\text{ }\mu\text{m}$ . Ces détecteurs sont interconnectés aux puces de lecture Timepix3 avec des pixels de taille de  $55\text{ }\mu\text{m}$ . Des simulations basées sur Geant4 (AllPix) ont été développées pour une meilleure compréhension du fonctionnement et de la résolution spatiale de ces détecteurs. AllPix est aussi employé pour la simulation du télescope de faisceau et il est ainsi possible d'extraire ses capacités pour la reconstruction des traces. Ces simulations servent aussi à prédire la résolution que pourraient atteindre les futurs détecteurs minces avec des pixels plus petits. Pour CLIC, une couverture intégrale du détecteur de vertex est essentielle tout en minimisant le contenu matériel. En effet, les détecteurs à bords minces permettent de couvrir intégralement les surfaces du détecteur de vertex en réduisant les zones inactives sans créer des chevauchements entre les modules des détecteurs à pixel. Des prototypes, avec des configurations différentes aux bords, sont testés en test faisceau de haute énergie afin de qualifier l'efficacité du bord actif. Des simulations TCAD, basées sur une méthode des éléments finis, sont mises en place pour reproduire la fabrication et l'opération de ces dispositifs. Les mesures sont comparées avec le résultat des simulations.



# Contents

---

<b>1</b>	<b>Introduction</b>	<b>1</b>
<b>2</b>	<b>CLIC: the Compact Linear Collider</b>	<b>3</b>
2.1	Physics potential of CLIC . . . . .	3
2.2	The CLIC accelerator . . . . .	6
2.2.1	Beam-induced backgrounds . . . . .	8
2.3	The CLIC detector . . . . .	8
2.3.1	Requirements for the vertex-detector . . . . .	9
2.4	Flavour-tagging performance at CLIC . . . . .	10
<b>3</b>	<b>Semiconductor detectors</b>	<b>15</b>
3.1	Basic properties of semiconductor material . . . . .	15
3.1.1	Silicon . . . . .	16
3.1.2	Doping . . . . .	17
3.2	Charge generation in silicon . . . . .	17
3.2.1	Bethe-Bloch formula . . . . .	18
3.2.2	Energy-loss spectrum in silicon . . . . .	18
3.2.3	The Landau distribution . . . . .	19
3.2.4	The Bichsel model . . . . .	20
3.2.5	Multiple scattering . . . . .	20
3.3	Transport of charge carriers in silicon . . . . .	21
3.3.1	pn-junction in thermal equilibrium . . . . .	22
3.3.2	Reverse-biased pn-junction . . . . .	23
3.4	Pixelated silicon sensors . . . . .	26
3.4.1	Charge collection and Ramo's theorem: induced charge . . . . .	28
3.4.2	Position measurement . . . . .	29
3.4.3	Hit position reconstruction using the $\eta$ -correction method . . . . .	33
<b>4</b>	<b>Pixel readout ASICs and assembly calibration</b>	<b>35</b>
4.1	The Timepix3 hybrid readout ASICs . . . . .	35
4.1.1	SPIDR readout system for Timepix3 . . . . .	37
4.2	Timepix3 assemblies . . . . .	38
4.3	Electronic noise . . . . .	38
4.4	Threshold dispersion and equalisation . . . . .	39
4.5	Operating threshold . . . . .	40
4.6	Calibration . . . . .	40
4.6.1	Threshold-energy calibration . . . . .	41
4.6.2	TOT-energy calibration . . . . .	43

4.7	Summary	44
<b>5</b>	<b>Simulation and reconstruction software frameworks</b>	<b>45</b>
5.1	GEANT4	45
5.2	AllPix simulation framework	46
5.2.1	Coordinate system	46
5.2.2	Geometry of the pixel detector	47
5.2.3	Geometry of the simulation scenario	47
5.2.4	Digitisation	48
5.3	TCAD simulations	49
5.4	Reconstruction and analysis software frameworks	50
5.4.1	EUTelescope	50
5.4.2	pyEudetAnalysis	52
<b>6</b>	<b>The Timepix3 beam telescope</b>	<b>55</b>
6.1	Experimental setup at the CERN SPS	55
6.2	Components of the telescope	55
6.2.1	Coordinates system	55
6.2.2	Sensors and mechanics	56
6.2.3	Data acquisition system	57
6.3	The telescope performance	57
6.3.1	Timepix3 telescope simulation in AllPix	57
6.3.2	Single-hit resolution on the telescope planes	58
6.3.3	Biased residuals on each telescope plane	59
6.3.4	Tracking resolution on the DUT	62
6.4	Summary	63
<b>7</b>	<b>Thin sensors studies</b>	<b>65</b>
7.1	Thin-sensor assemblies	65
7.1.1	Operating conditions	65
7.2	Experimental and simulated results for thin sensors	66
7.2.1	Calibrated test beam data	66
7.2.2	Measurement of the depletion voltage	66
7.2.3	Cluster size distribution	67
7.2.4	Charge sharing as a function of the track position	69
7.2.5	Single-point resolution	71
7.2.6	Detection efficiency	73
7.3	Extrapolation to smaller pixels	73
7.4	Summary	74
<b>8</b>	<b>Active edge sensors</b>	<b>77</b>
8.1	The active-edge technology processing	77
8.1.1	Process flow for sensor production by the manufacturer	78
8.1.2	Layout parameters of produced assemblies	80
8.1.3	Process flow for the simulation of the active-edge designs	81
8.2	Electrical measurements and simulations	83

8.3	Edge performance in data and simulations . . . . .	86
8.3.1	TCAD simulation of the detector response . . . . .	86
8.3.2	Conventions used for the presentation of the results . . . . .	86
8.3.3	The performance of 50 $\mu\text{m}$ thick sensors . . . . .	87
8.3.4	The performance of 100 $\mu\text{m}$ and 150 $\mu\text{m}$ thick sensors . . . . .	90
8.4	Summary . . . . .	92
<b>9</b>	<b>Conclusions</b>	<b>95</b>
<b>Bibliography</b>		<b>97</b>
<b>A Pixel readout ASICs and assembly calibration</b>		<b>105</b>
<b>B Telescope</b>		<b>107</b>
<b>C Thin Sensors</b>		<b>111</b>
C.1	Depletion voltage . . . . .	111
C.2	Cluster size distribution . . . . .	112
C.2.1	Cluster size distribution as a function of the bias voltage . . . . .	112
C.2.2	Cluster size distribution as a function of the operating threshold . . . . .	113
C.3	Charge sharing as a function of the track position . . . . .	114
<b>D Active edge sensors</b>		<b>115</b>
<b>List of Figures</b>		<b>117</b>
<b>List of Tables</b>		<b>123</b>
<b>Acknowledgements</b>		<b>125</b>



# CHAPTER 1

---

## Introduction

---

The Compact Linear Collider (CLIC) concept [1] for a future linear  $e^+e^-$  collider is under development by the international CLIC collaboration. Its physics programme has the potential to complement the measurements done by the LHC experiments. With proposed centre-of-mass energies of 380 GeV, 1.5 TeV and 3 TeV and with an instantaneous luminosity up to  $6 \times 10^{34} \text{ cm}^{-2}\text{s}^{-1}$ , this lepton collider allows for high precision measurements of Standard Model physics and of new physics potentially discovered at the 13 TeV LHC, as well as searches for Beyond Standard Model (BSM) physics.

For the CLIC experiment, a detector system is under development which takes into account the precision physics requirements and experimental conditions [2]. The innermost sub-detector, located closest to the interaction point, is a silicon pixel detector with three double layers both in the barrel and the endcap regions. Its main goal is to distinguish heavy quarks from light-flavoured quarks through a precise measurement of their displaced decay vertices. The precision physics requirements set challenging demands for the vertex detector in terms of spatial resolution, material budget with efficient heat removal from sensors and readout and also timing resolution. The CLIC vertex detector R&D programme studies different detector technologies and takes into account constraints from mechanics, power delivery and cooling. In order to reduce multiple scatterings to profit from the good impact parameter resolution, a low total material budget of  $\sim 0.2\% X_0$  per vertex detector layer is required including readout, support and cabling. The goal is to achieve a single-point resolution of  $3 \mu\text{m}$  with  $50 \mu\text{m}$  thick sensors coupled to  $50 \mu\text{m}$  thick readout ASICs with  $25 \mu\text{m}$  pixel pitch.

In this thesis, the feasibility of thin pixelated planar silicon sensors for operation in the CLIC vertex detector is studied. Planar silicon technology is already well known and widely used in the pixel detectors of the modern high-energy physics experiments. Assemblies with  $50 \mu\text{m}$  to  $150 \mu\text{m}$  thick sensors are bump bonded to Timepix3 readout ASICs [3] with a pixel size of  $55 \mu\text{m}$ . These assemblies are tested during test-beam campaigns at the CERN SPS. Data are used for the characterisation of the thin sensors in terms of energy deposition, charge sharing and spatial resolution. A GEANT4-based [4] simulation of the signal formation in planar silicon sensors has been developed and is used to gain a better understanding of thin sensors. After being validated with data, the simulation is used to investigate the possible performance of sensors with smaller pixels where no experimental data is yet available.

Active-edge sensors allow for seamless tiling of pixel sensors by depleting the sensors up to their physical edges. In a vertex detector, this allows for high coverage without creating overlaps between the pixel sensors and therefore reduces the material content. Efficiency measurements in test-beams on prototypes and corresponding finite-element TCAD simulations are performed to compare the performance of different active-edge sensor layouts, resulting in a proposal for a suitable layout.

This thesis is structured as follows. Chapter 2 describes the CLIC experiment. The accelerator concept

based on a novel 2-beam acceleration scheme is briefly introduced. The requirements on the CLIC detector, with a focus on the vertex detector, are given. The flavour-tagging performance is studied for different geometries of the vertex detector.

General working principles of the semiconductor detectors are presented in Chapter 3.

The Timepix3 readout ASIC is introduced in Chapter 4. The tested assemblies are presented and their readout noise is measured. The calibration methods for these assemblies are discussed.

The simulation and reconstruction software frameworks are described in Chapter 5.

The Timepix3 pixel beam-telescope used for testing the Timepix3 assemblies is described in Chapter 6. Its performance is investigated in data and simulations.

The performance of thin sensors is studied in Chapter 7 and simulations are validated with test-beam data. The spatial resolution of a 50  $\mu\text{m}$  thin detector with 25  $\mu\text{m}$  pitch (as well as smaller pixel pitches) is estimated using the simulation model.

The performance of active-edge sensors is discussed in Chapter 8. Different designs for the guard ring at the edge are considered and the results obtained in the test beams are compared to TCAD simulations.

Chapter 9 summarises the obtained results and gives conclusions.

## CHAPTER 2

---

# CLIC: the Compact Linear Collider

---

Today, the Large Hadron Collider (LHC) is the largest particle accelerator being able to collide two opposing particle beams of protons with a center-of-mass energy up to 13 TeV. So far, the main result of the LHC is the observation of the Higgs boson and the determination of its mass in 2012. However, the experiments at the LHC can not fully answer the questions on the nature of this particle. Several options of lepton colliders, providing complementary precision measurements, are under study.

The energy loss due to the synchrotron radiation in a circular accelerator limits the center-of-mass energy  $\sqrt{s}$  reached with electron beams. The synchrotron power loss is inversely proportional to the square of the bending radius of the accelerator and the forth power of the particle mass. The proposed Compact Linear Collider (CLIC) [1, 2], as a future linear particle collider for electrons ( $e^-$ ) and positrons ( $e^+$ ), can avoid synchrotron radiation losses and therefore attain higher center-of-mass energies than the Large Electron-Positron Collider (LEP). In the post-LHC era, CLIC will allow to determine the properties of the Higgs boson with a very high precision. CLIC can measure collisions with center-of-mass energies  $\sqrt{s}$  from 380 GeV up to 3 TeV.

The FCC-ee study [5], as a part of the Future Circular Collider (FCC) project, is another option for a future Higgs factory. It aims to achieve center-of-mass energies of  $\sqrt{s}$  from 90 GeV to 350 GeV in a high-precision  $e^+e^-$  circular collider. It is foreseen to be built in a new 80-100 km tunnel in the Geneva area.

In this chapter, we will briefly discuss the standard model of particle physics and attempt to understand how CLIC can determine more precisely the properties of the Higgs boson. Subsequently, the CLIC accelerator, detector and its components are described. The focus is set on the vertex detector, its requirements and its flavour-tagging performance.

### 2.1 Physics potential of CLIC

In particle physics, the Standard Model (SM) [6–9] is a theoretical framework that describes how the interaction between elementary particles is governed by three out of the four known fundamental forces. This theory, developed in the early 1970s, explains most of the experimental results.

According to the Standard Model, matter is made of elementary particles which can be regrouped into two basic kinds: quarks and leptons. The interaction between the particles is done through fundamental forces corresponding to the exchange of force-carrying particles known as gauge bosons as shown in Figure 2.1 [10].

Today, the Standard Model is the best theory describing the subatomic world. However, it does not answer questions like the nature of dark matter. This theory also predicts the existence of the Higgs

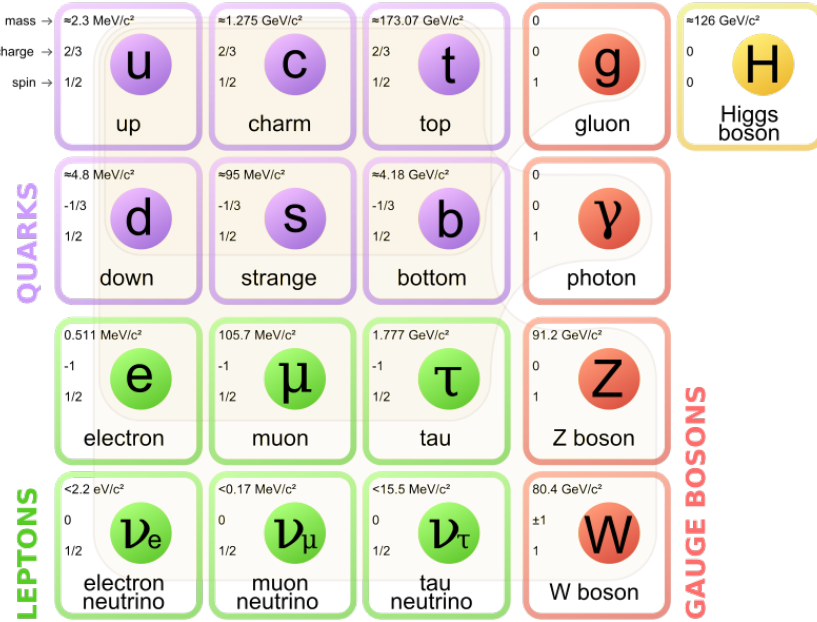


Figure 2.1: The building blocks of matter according to the Standard Model [11].

boson which gives the mass to all particles. It was experimentally observed in 2012 by the ATLAS [12] and CMS [13] experiments at CERN.

The weak and the electromagnetic forces are closely related to each other and can be unified as the *electroweak* interaction and the equations describing the unification predict the force-carrying particles (the photon, the W and Z bosons). All force-carrying particles are described as being massless which is true for the photon, but the W and Z bosons have a mass about 100 times larger than that of the proton. To solve this problem, the Brout-Englert-Higgs mechanism was introduced which suggests that the Higgs boson gives the mass to the W and Z boson by interaction with a Higgs field.

The Higgs boson can be produced in a particle collider by collisions between highly energetic particles. Heavy particles, like the Higgs boson, are occasionally produced and detected by a particle detector. The most important parameters of a particle collider are its center-of-mass energy, determining the types of particles that can be studied or discovered, and its instantaneous luminosity, determining the event rates. For a given process, the cross section is a measure of quantum mechanical probability for interaction and it depends on the fundamental physics. Therefore, the observed number of events for a given process depends on the integrated luminosity over the operation time of the collider and the cross section of the process. The Standard Model predicts different mechanisms to produce the Higgs boson and the cross section is very small. For example, in LHC only 1 Higgs boson is produced per 10 billion collisions.

An electron-positron collider allows to perform precision measurements by colliding beams made of elementary particles. With elementary particles, the center-of-mass energy and the polarisation of the colliding particles can be selected precisely. Unlike proton-proton collisions at the LHC experiments, there is no underlying event from proton remnants. The complicated environment of a hadron machine makes the measurements of the fundamental properties of the Higgs boson very hard. The added value of an electron-positron collider would be to measure in great details the Higgs mass and its total decay width, its spin-parity quantum numbers, its couplings to fermions and gauge bosons and also its self couplings that allows for the reconstruction of the scalar potential that is responsible of electroweak symmetry breaking [2].

CLIC is foreseen to be built and operated in three stages with center-of-mass energies of 380 GeV, 1.5 TeV and 3 TeV as shown in Figure 2.2 [14]. The site studies have shown that CLIC could be placed near CERN underground. For each stage, to increase the center-of-mass energy, more accelerating modules will be needed, making the accelerator longer. The site length for 3 TeV will be 50 km.

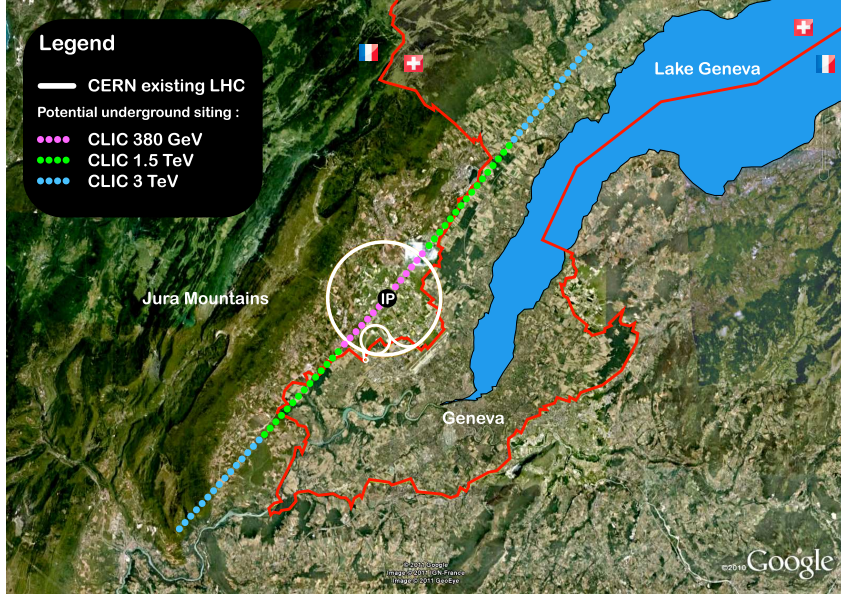


Figure 2.2: The three implementation stages of CLIC near CERN with center-of-mass energies of 380 GeV, 1.5 TeV and 3 TeV [14].

The different energy stages at CLIC allow for maximising the luminosity performance and physics potential for high precision measurements of Standard Model physics (e.g. Higgs, top) as well as new physics potentially discovered at the 13 TeV LHC.

The first energy stage allows for studying the Standard Model Higgs physics and top-quark physics with the possibility to perform a  $t\bar{t}$  threshold scan. This stage gives the possibility to perform model-independent cross-section measurements [15]. The second energy stage provides direct sensitivity to many physics beyond the SM (BSM) models. With larger Higgs statistics, rare processes such as  $t\bar{t}H$  and double Higgs production can be measured. Finally, the third energy stage provides the best sensitivity to new physics, the double-Higgs production and allows for improving the measurements of the Higgs self-coupling and HHWW quartic coupling. Figure 2.3 shows different mechanisms to produce the Higgs boson at CLIC.

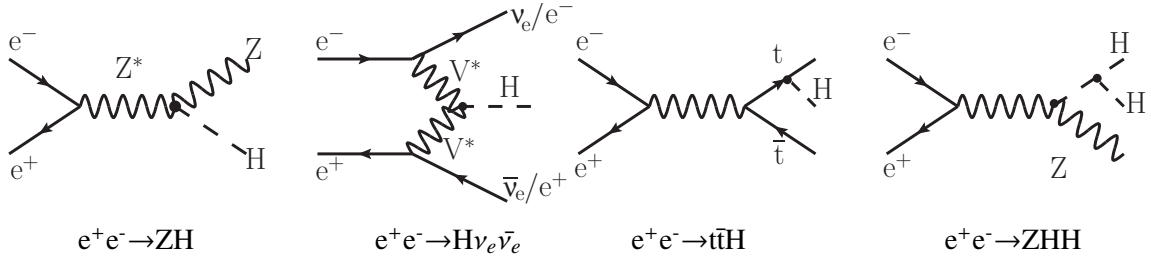


Figure 2.3: Standard Model Higgs boson production mechanisms at CLIC [2].

The cross sections to produce a Higgs with a mass of  $M_H = 126$  GeV as a function of the center-of-mass energy  $\sqrt{s}$  are given in Figure 2.4. Below  $\sqrt{s}$  of  $\sim 500$  GeV, the HZ mechanism is dominant. For higher energies, the  $H\nu_e\bar{\nu}_e$  mechanism dominates.

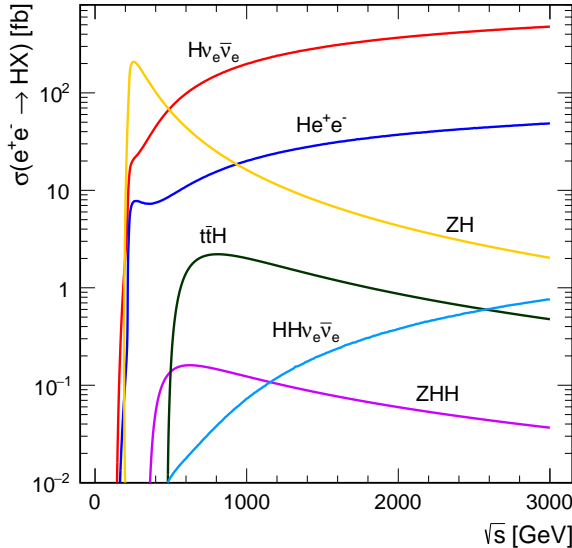


Figure 2.4: Cross sections for the main Higgs production mechanisms for a  $M_H = 126$  GeV Higgs boson as a function of the  $e^+e^-$  center-of-mass energy in a lepton collider. These values correspond to unpolarised beams and the effect of beamstrahlung is not included [14].

Final states with heavy quark flavours are important in many physics channels, such as the Higgs and the top. The identification of the heavy quarks is performed through the measurement of the displaced vertices and the vertex detector has a crucial role in these measurements as described in the following chapters.

## 2.2 The CLIC accelerator

The schematic layout of the CLIC accelerator complex at  $\sqrt{s} = 3$  TeV is shown in Figure 2.5. The electron and positron beams are accelerated on a linear trajectory and collide in the central region (at the interaction point), where the CLIC detector is placed. Each linac is fed by a drive-beam generation complex.

To limit the length of the accelerator, the accelerating field has to be as high as possible. The accelerating gradient is chosen to be 100 MV/m. This leads to the use of copper cavities at room temperature instead of superconducting cavities since the latter have an intrinsically limited maximum field. The copper cavities are fed with radio frequency (RF) power at a very high frequency of 12 GHz to generate the high accelerating field. This leads to a total RF peak power of 9.2 TW for both linacs. Since maintaining such high power levels is not possible for very long, the duration of the bunch train is limited to 156 ns with a repetition frequency of 50 Hz.

Traditionally, klystrons are used in accelerators to provide the RF power to the main beam. However, for CLIC, klystrons are not directly used to accelerate the main beam since a large number of them would be needed and their efficiency would be too low at 12 GHz. A two-beam acceleration scheme is used to reach the nominal collision energy. A drive beam is running in parallel to the main beam. The drive

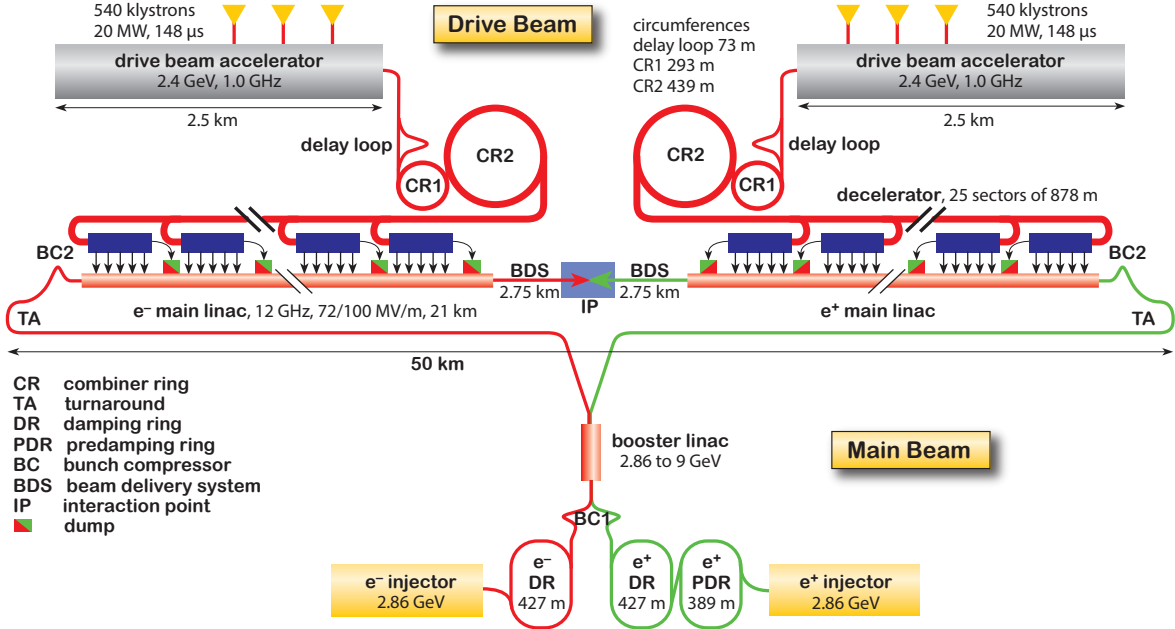


Figure 2.5: Schematic layout of the CLIC accelerator complex at  $\sqrt{s} = 3$  TeV. Each linac is fed by a drive-beam generation complex [14].

beam has a low energy of 2.4 GeV and a high current of 100 A. It is used to transfer the energy of the klystrons to the main beam which has a lower current and higher energy. Power Extraction and Transfer Structures (PETS) are special RF devices which extract the power of the drive beam by decelerating the beam. The extracted energy is then provided to the main beam. CLIC is divided into sectors with an average length of 878 m and each section accelerates the main beam by  $\approx 62$  GeV.

Table 2.1 summarises the nominal beam parameters for the 3 TeV CLIC and 13 TeV LHC. An instantaneous luminosity  $\mathcal{L}$  of a few  $10^{34} \text{ cm}^{-2}\text{s}^{-1}$  insures a sufficient amount of data collected in a reasonable amount of time. The beam sizes at the interaction point of CLIC have to be extremely small in order to achieve the desired luminosity. The RF pulse duration limits the number of bunches and the bunch-crossing separation. CLIC and LHC have similar luminosity despite the differences in beam parameters.

Table 2.1: Nominal beam parameters for CLIC at  $\sqrt{s} = 3$  TeV and LHC at  $\sqrt{s} = 13$  TeV.

	CLIC at $\sqrt{s} = 3$ TeV	LHC at $\sqrt{s} = 13$ TeV
Colliding particles	electron-positron	proton-proton
Instantaneous luminosity $\mathcal{L}$	$6 \times 10^{34} \text{ cm}^{-2}\text{s}^{-1}$	$1 \times 10^{34} \text{ cm}^{-2}\text{s}^{-1}$
Bunch-crossing separation	0.5 ns	25 ns
Bunches per train	312	Not applicable
Train duration	156 ns	Not applicable
Train repetition	50 Hz	Not applicable
IP size in x / y / z directions	45 nm / 1 nm / 44 μm	15 μm / 15 μm / 5 cm

### 2.2.1 Beam-induced backgrounds

The small beam sizes at CLIC cause strong electromagnetic radiation (Beamstrahlung) from the electron and positron bunches in the field of the opposite beam. The generation of Beamstrahlung photons leads to a reduction of the available centre-of-mass energy  $\sqrt{s}$  of the  $e^+e^-$  collisions. The interactions of Beamstrahlung photons produce lepton pairs and hadrons at low polar angles which are mostly contained in the beam-pipe [16]. In the inner detector layers, incoherently produced electron-positron pairs ( $\sim 60$  particles per bunch crossing) and  $\gamma\gamma \rightarrow$ hadrons events ( $\sim 54$  particles per bunch crossing) are the dominant backgrounds.

The electron-positron pairs produced at low polar angles have very small transverse momentum. The occupancies in the innermost layers of the detector can be reduced to an acceptable level by optimising the inner and forward detector regions. The beam-pipe walls have to be placed outside of the high-rate region. The inner detectors have to be shielded from the backscattered particles which originate from the forward region.

The  $\gamma\gamma \rightarrow$ hadrons interactions produce particles with a higher transverse momentum spectrum and a more central polar-angle distribution. This results in large rates of background particles reaching the outer detector layers. In each train, at most one interesting physics event is expected along with  $\sim 1000$  hadronic background events.

Hit time stamping on the level of 1 to 10 ns in all sub-detectors is needed in order to separate the physics from the background events.

The exposure to radiation of the main detector elements is expected to be small compared to high-energy hadron-colliders.

## 2.3 The CLIC detector

To cover the CLIC physics potential, a detector concept is under development. The physics goals set challenging requirements on the design of the detector. Simulation tools are crucial for the design, development as well as the optimisation of the detector model.

The experimental conditions due to the beam-induced background (see Section 2.2.1), set the most demanding requirements at the highest collision energy. Therefore, the detector model is mainly optimised for the 3 TeV CLIC.

Figure 2.6 shows the CLIC detector model as implemented in simulations. The overall length and height of the detector are 11.4 m and 12.9 m respectively. It is composed of several sub detectors. The vertex detector is the closest to the IP and consists of pixelated silicon detectors. It is followed by the main tracker which is also a silicon-based detector. After the tracking systems, fine grained calorimeters are used: the silicon-tungsten electromagnetic calorimeter (ECAL) and the steel hadronic calorimeter (HCAL). The superconducting coil surrounds the calorimeters to provide a magnetic field of 4 T to deflect the trajectory of charged particles. The tracking detectors use the radius of curvature to measure the momentum of charged particles. In the very forward region, the luminosity calorimeter (LumiCal) is used to reconstruct precisely the energy and angle of electrons and positrons obtained from Bhabha events and employed for the luminosity measurements [17]. The beam calorimeter (BeamCal) is used for electron tagging by the identification of high energy electrons [18]. Finally the iron yoke surrounds the whole detector and is instrumented for the identification of muons.

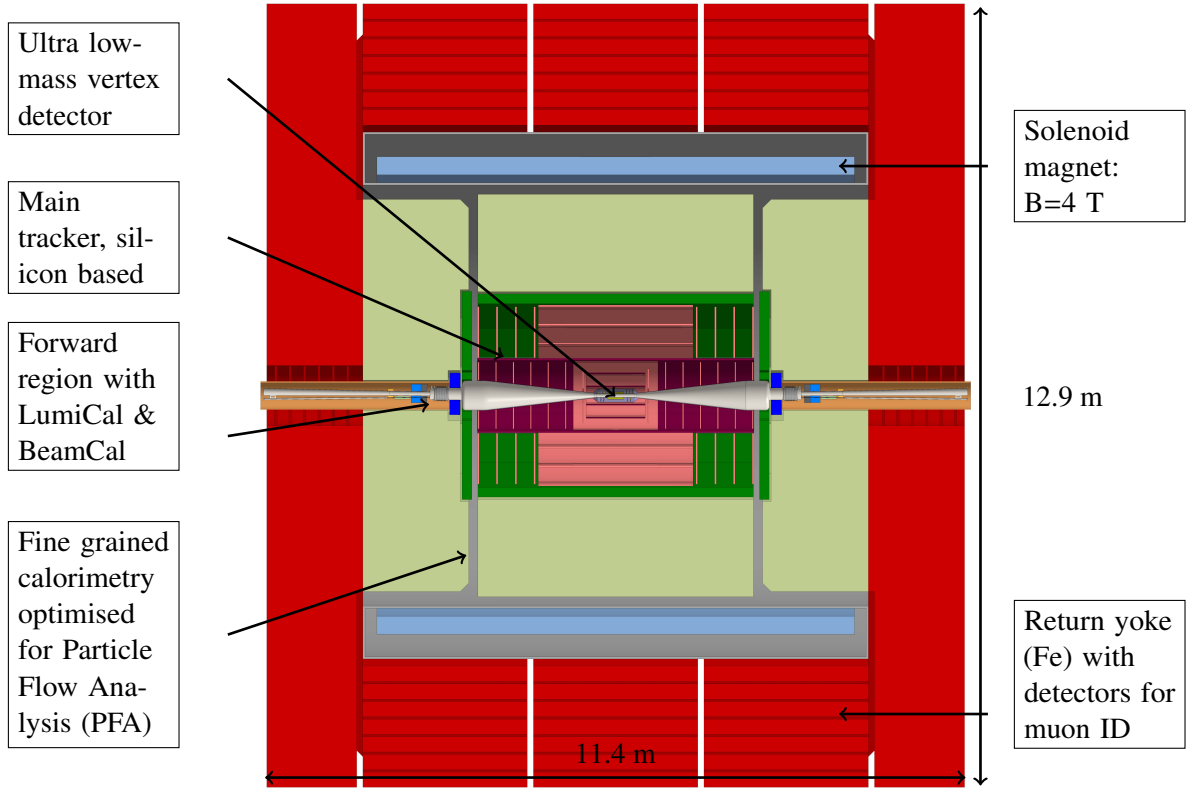


Figure 2.6: Schematic layout of the CLIC detector concept [19].

### 2.3.1 Requirements for the vertex-detector

The main goal of the CLIC vertex detector is the efficient tagging of heavy quarks through the precise measurement of the displaced vertices. To achieve this goal, Monte Carlo simulations have shown that a high-momentum term in the transverse impact-parameter resolution of  $a \approx 5 \mu\text{m}$  and a multiple-scattering term of  $b \approx 15 \mu\text{m}$  are needed using the canonical parametrisation [2]:

$$\sigma(d_0) = \sqrt{a^2 + b^2 \cdot \text{GeV}^2 / (p^2 \sin^3 \theta)}, \quad (2.1)$$

where  $p$  is the momentum of the particle and  $\theta$  is the polar angle with respect to the beam axis.

To meet these requirements, a multi-layer barrel and endcap pixel detector with an inner radius of  $\approx 30 \text{ mm}$  with a geometrical coverage extending down to low polar angles ( $\theta_{\min} \approx 8^\circ$ ) is needed. For the beam-pipe and for each of the detection layers a material budget of  $\approx 0.2\%$  of a radiation length ( $X_0$ ) is considered. Sensors with a single-point resolution of  $\approx 3 \mu\text{m}$  operating in a magnetic field of 4 T are required.

In the innermost layers, an occupancy of  $\approx 3\%$  due to the beam-induced backgrounds is expected [16]. To separate these backgrounds from physics events, a time slicing of the hits with an accuracy of  $\approx 10 \text{ ns}$  is required. To achieve this precise time stamping, hybrid detectors (where sensors and electronics are separately manufactured and later combined) are preferred since they provide more advanced timing measurement technologies.

In comparison to the current pixel detectors in the LHC experiments, the expected radiation level in the region of the CLIC vertex detector is moderate. For the inner-detector layers a total 1 MeV

neutron-equivalent fluence of less than  $10^{11}$  neq/cm $^2$ /year and a total ionising dose of less than 1 kGy are expected [16].

The aim of the vertex detector R&D is to achieve the required single-point resolution with pixels of size  $\approx 25\text{ }\mu\text{m} \times 25\text{ }\mu\text{m}$  with 50  $\mu\text{m}$  thick sensors coupled to 50  $\mu\text{m}$  thick readout ASICs with pulse-height measurement capability. The constraint on the material budget implies no active cooling elements can be placed inside the vertex detector. To limit the maximum power dissipation of the readout electronics to  $\approx 50\text{ mW/cm}^2$ , forced air-flow cooling and power pulsing (i.e. turning off most components on the readout chips during the 20 ms gaps between bunch trains) are foreseen.

## 2.4 Flavour-tagging performance at CLIC

The precision physics measurements require excellent flavour-tagging performance of the CLIC vertex detector. Different vertex detector geometries have been studied for CLIC [20, 21]. This section presents the impact of the geometry on the flavour-tagging performance in simulations. This study has been published in [21].

A first geometry designed for the CLIC vertex detector is shown in Figure 2.7. It contains 5 layers in the barrel and 4 disks in the endcap region. Since forced airflow cooling is foreseen for CLIC as illustrated in Figure 2.8(a), a spiral arrangement for the modules in the endcap regions has been implemented instead of disks, allowing the air to flow through the vertex detector.

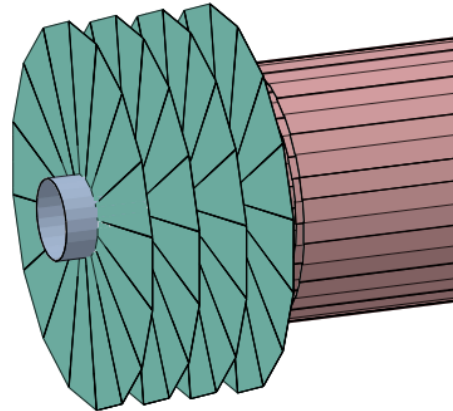


Figure 2.7: The schematic view of the disks geometry with 5 single-sided layers in the barrel region and 4 single-sided disks in the endcap region.

The physics performance of the geometries described in Table 2.2 and illustrated in Figure 2.8 have been studied in simulations.

The multi-variate LCFIPlus flavour-tagging package [22] is used to assign each jet category with a beauty (b) and charm (c) probability. The fake rates of separating the charm and beauty jets from each other and from light flavour (LF) jets have been investigated.

The detector models in simulation consider the single-point resolution of the sensors ( $\sim 3\text{ }\mu\text{m}$ ) and include layer thicknesses based on constraints from an engineering model of the mechanical support and the air cooling system [20].

The performance of the flavour tagging depends on the jet energy and polar angle: dijet events with different center-of-mass energies,  $\sqrt{s}$ , having polar angles of  $10^\circ \leq \theta \leq 90^\circ$  with a uniform distribution

Table 2.2: Vertex detector geometries implemented in simulations.

Geometry	Barrel layers	Endcap layers	Material budget
<i>spirals</i> (Figure 2.8(b))	5 single-sided	4 single-sided	0.1% $X_0$ per single-sided layer
<i>double_spirals</i> (Figure 2.8(c))	3 double-sided	3 double-sided	0.2% $X_0$ per double-sided layer
<i>double_spirals_v2</i>	3 double-sided	3 double-sided	0.4% $X_0$ per double-sided layer

Figure 2.8 consists of three parts: (a) A sketch showing the airflow cooling strategy within the vertex detector, with arrows indicating air flow through the barrel and endcap regions. (b) A schematic view of the vertex detector for the *spirals* geometry, showing a cross-section of the barrel with green spiral-shaped layers. (c) A schematic view of the vertex detector for the *double\_spirals*(*v2*) geometry, showing a cross-section of the barrel and endcap with green double-sided layers. Below part (c), a diagram shows a 2 mm thick double-sided layer with two blue horizontal bars labeled "Silicon" and "Carbon".

Figure 2.8: (a) Sketch showing the airflow cooling strategy within the vertex detector [23]. (b) Schematic view of the vertex detector for the *spirals* geometry. (c) Schematic view of the vertex detector for the *double\_spirals*(*v2*). In the GEANT4 simulations [4], a double-sided layer is implemented as two silicon sensors on top of each other with an overall thickness of 2 mm. From [21].

in azimuthal  $\phi$  angles are considered. Initial state radiation (ISR) and beamstrahlung (BS) were switched off during the event generation and hence the final-state quarks are in a back-to-back configuration. For each jet flavour, energy and angle, 80000 events are used for the following processes:  $e^+e^- \rightarrow b\bar{b}$ ,  $c\bar{c}$ ,  $u\bar{u}$ ,  $d\bar{d}$ ,  $s\bar{s}$ . The boosted decision tree (BDT) classifiers are trained using 50% of the generated events and the other 50% are used for testing the performance of the flavour tagging.

Figure 2.9 shows the dependence of the flavour-tagging performance on the jet polar angle in the *disks* geometry for jets in dijet events at  $\sqrt{s} = 200$  GeV. Figure 2.9(a) shows the fake rate of recognising beauty jets as charm jets versus the beauty-tagging efficiency. For dijet events at  $\theta = 40^\circ$ , for a  $b$ -tagging efficiency of 80%, the probability to misidentify charm quarks as beauty quarks is  $\sim 5\%$ . Figure 2.9(b) shows the fake rate of recognising charm jets as beauty jets versus the charm-tagging efficiency. As expected, the  $b$ -tagging performance is better than the  $c$ -tagging performance. However, CLIC allows for a higher charm tagging performance compared to the LHC experiments.

The flavour-tagging performance for the different vertex detector geometries as shown in Figure 2.8 is summarised in Figure 2.10 where the fake rate of recognising charm and light flavour jets as beauty jets is plotted versus the  $b$ -tag efficiency.

The *spirals* and *disks* have a similar flavour-tagging performance except for jets at  $\theta = 40^\circ$  (see Figure 2.10(a)), which corresponds to the transition between the vertex endcaps and the barrel region, where the beauty-tagging performance is up to 20% worse using the *spirals* geometry (compared to *disks*). With the spiral configuration, the number of sensitive layers becomes dependent on the azimuthal angle  $\phi$  and fewer layers can be hit in certain ranges of  $\phi$ . The performance degradation caused by this  $\phi$  dependence can be mitigated by increased  $\phi$  overlap in future geometry implementations.

The performance of the *spirals* and the *double\_spirals* is very similar as shown in Figure 2.10(b). The *double\_spirals\_v2* geometry is a more realistic version of the *double\_spirals* geometry, taking into

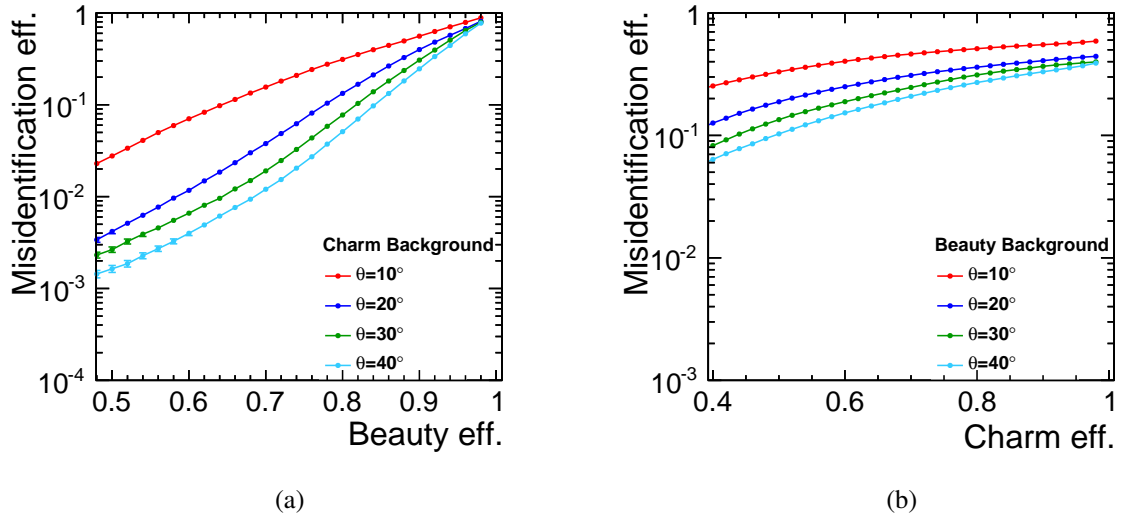


Figure 2.9: (a) b-tag and (b) c-tag efficiency for jets in dijet events at  $\sqrt{s} = 200$  GeV with different polar angles for the *disks* geometry [20].

account the material used for the mechanical support of the sensors and also for the cables. As shown in Figure 2.10(c), the misidentification probability increases by  $\sim 35\%$  due to the increased material.

A detector model for CLIC is under development which takes into account the progressing engineering studies. The spiral arrangement of the modules in the vertex endcaps allows to use airflow cooling which has the potential to reduce the material budget significantly. Double-sided modules provide more sensitive layers with the same amount of support material as single-sided modules. The overall results show that the implemented geometries are similar in terms of the flavour-tagging performance for simulated dijet events. The impact of a spiral arrangement of the modules in the endcap region remains similar to the disks. The amount of material, on the other hand, was found to have a large impact on the performance.

The following chapters focus on the R&D of the pixel detectors in the vertex detector with high-resolution and very low material budget in order to achieve high flavour-tagging performance as required by the precision physics to be measured at CLIC.

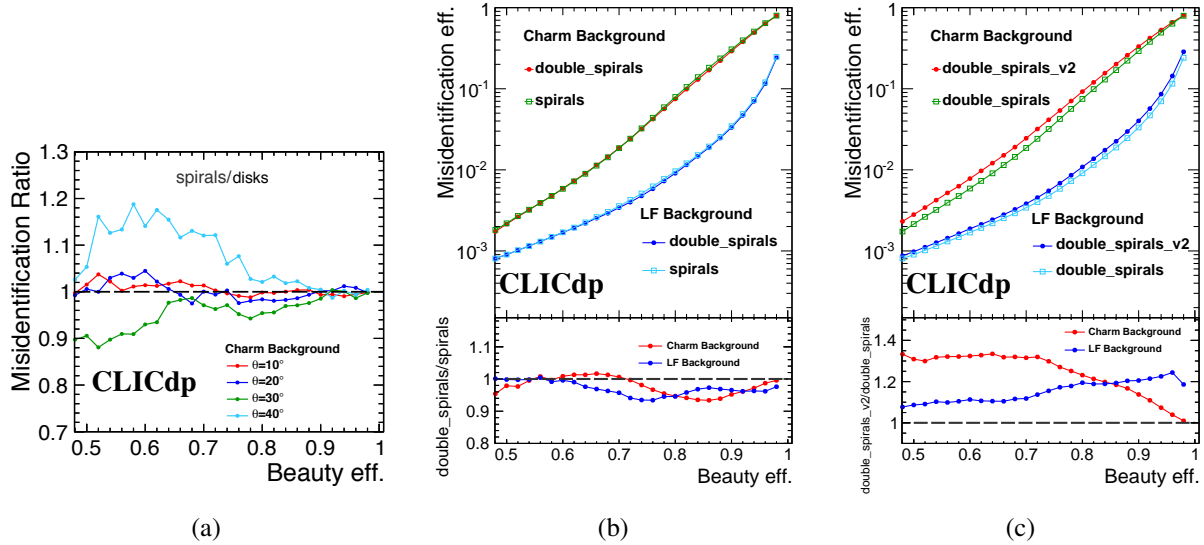


Figure 2.10: Beauty-tagging performance for dijet events at 200 GeV. (a) Comparison between *disks* and *spirals* in terms of the ratio of the misidentification probabilities for charm background. (b) Comparison of the beauty-tagging performance between the *spirals* and *double\_spirals* geometries. (c) Comparison of the beauty-tagging performance between the *double\_spirals* and *double\_spirals\_v2* geometries. For (a) the misidentification ratio for each polar angle is shown separately. For (b) and (c), dijet events with a mixture of polar angles between  $10^\circ$  and  $90^\circ$  are considered. From [21].



# CHAPTER 3

---

## Semiconductor detectors

---

Semiconductor materials have a great advantage in many radiation detection applications. The main benefits are the high energy resolution due to the large number of free charge carriers that are created by a given incident radiation, their compact sizes, fast timing, while the effective thickness can be adapted to the requirements of the applications. Though, they show some limitations for smaller sizes and their performance can degrade from radiation induced damages. Among semiconductor materials, silicon detectors are predominant for tracking systems in modern particle physics experiments. The energy deposited by high energetic particles in silicon detectors can be used for the track position reconstruction and provide high tracking resolutions.

In this chapter, we will review the basic properties of semiconductor material, charge generation in silicon and the transport of charge carriers through drift and diffusion. Pixel detectors are presented. The charge collection and position measurement for hits in pixels are explored.

### 3.1 Basic properties of semiconductor material

Due to the periodic lattice of crystalline materials, electrons within the solid have allowed energy bands. The energy of the electrons is confined to one of the energy bands and the bands may be separated by gaps of forbidden energies.

Figure 3.1 schematically illustrates the bands in insulators, semiconductors and metals. In the *valence band*, the electrons are bonded to specific lattice sites within the crystal. The electrons in the *conduction band* are free to move through the crystal and contribute to the electrical conductivity. The *bandgap* ( $E_g$ ) separates the valence from the conduction band and allows to classify whether the material is a semiconductor, an insulator or a metal. In the absence of thermal excitation, the valence band for the semiconductors and insulators is completely full and the conduction band empty. Therefore they are not electrically conductive. Metals are highly electrically conductive since the fermi energy level ( $E_F$ ) lies in the conduction band and the electrons are free to migrate through the material even at very low temperatures. However, for insulators and semiconductors the electrons must cross the bandgap to become conductive. The bandgap for semiconductors ( $\sim 1$  eV) is much lower than for insulators ( $\sim 5$  eV). If an electron in the valence band gains enough thermal energy to cross the bandgap and reach the conduction band, it leaves behind a vacancy (a hole) in the valence band. The electron-hole pair can move under the influence of an external electric field (electrons in the opposite direction of the holes). This motion creates conductivity in the material. This property is exploited in silicon detectors to detect radiation and is developed more in the coming sections.

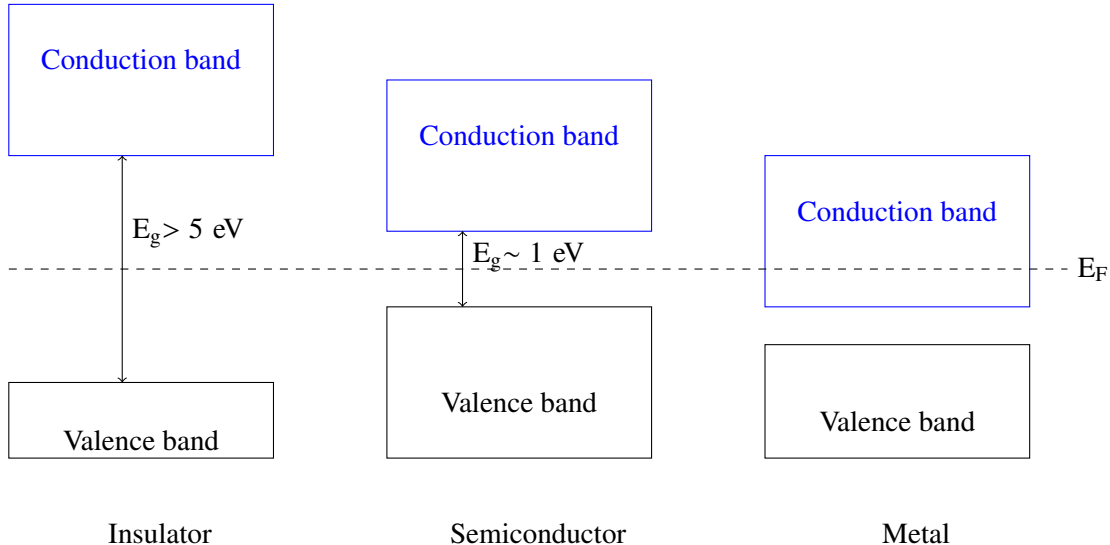


Figure 3.1: Illustration of the band structures for electron energies in insulators, semiconductors and metals.  $E_F$  represents the Fermi energy level and  $E_g$  the bandgap.

### 3.1.1 Silicon

In semiconductors, the excitation energy is defined by the periodicity of the crystal lattice. Silicon is a semiconductor with a *diamond* lattice as illustrated in Figure 3.2. The dimension  $a$  is the lattice constant and is 5.34 Å in silicon.

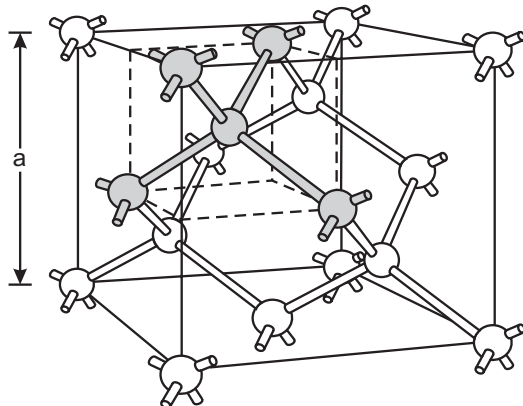


Figure 3.2: Lattice structure of silicon. The building block of the lattice is formed by a central atom bonded to four equidistant neighbours as shown in shaded gray. From [24].

In the periodic table, silicon is a group four element as it has four valence electrons and which combine with four neighbours to build covalent bonds and close the outer shell. At 0 K, no electrical conduction is possible since all the electrons fill completely the valence band. An incident radiation can break a bond and excite an electron into the conduction band. This leaves a *hole* or a vacant state in the valence band and the electron can freely move in the conduction band. The hole can also move in the valance band by the indirect mechanism where an electron from a neighbouring atom fills it and creates another hole.

An external electric field can direct the motion of the electrons and holes created. Holes are treated as positive charge carriers.

In silicon, the bandgap  $E_g$  is 1.12 eV and the ionisation energy (or the average energy deposition required to produce an electron-hole pair) is about 3.6 eV. The ionisation energy is higher than the bandgap. Only a fraction of the absorbed energy creates the signal charge and the rest goes into phonon excitation which will be dissipated as thermal energy.

### 3.1.2 Doping

By introducing impurities, the conductivity of semiconductors can be controlled. Typical concentration ranges between  $10^{12} - 10^{18} \text{ cm}^{-3}$ . In semiconductors, the conductivity comes from either electrons (n-type) or holes (p-type).

In *n-type doping*, a silicon atom is replaced with an atom having five valence electrons, for example phosphorus as illustrated in Figure 3.3(a). This creates an excess in electrons into the lattice and is called a donor. The donor electron is lightly bound to the impurity atom. As a consequence, the ionisation probability is increased and mobile electrons are introduced into the conduction band.

In *p-type doping*, by introducing a group three atom into the silicon lattice such as the boron, one impurity valence electron is left as schematically shown in Figure 3.3(b). This type of dopant is called an acceptor: the dopant borrows an electron from a neighbouring atom and the holes can move freely throughout the crystal.

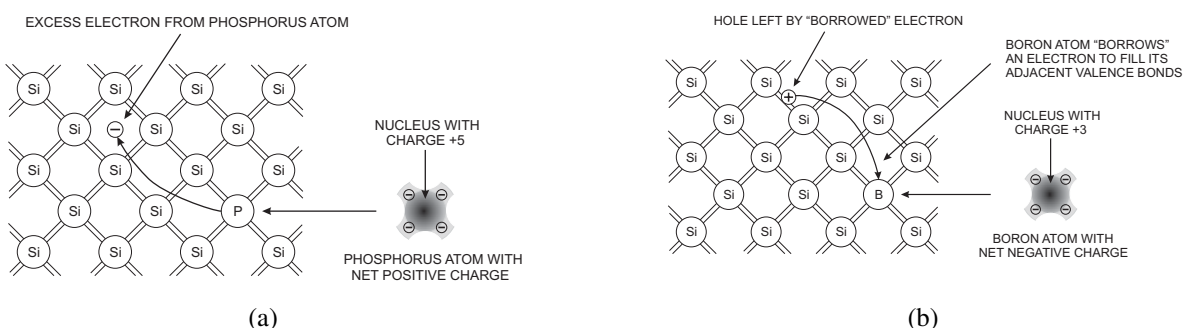


Figure 3.3: (a) Introducing a group five impurity, such as phosphorus, creates a lightly bound electron that can move under the influence of an electric field. (b) Introducing a group three impurity, such as boron, creates an unpaired silicon bond which can attract a neighbouring electron and results in a hole moving throughout the silicon lattice. From [24].

## 3.2 Charge generation in silicon

The interaction of incident radiation with a silicon sensor is the basis for detection of charged particles. Part of the energy of the particle is absorbed by a silicon sensor and creates electron-hole pairs. The generated pairs can be detected as electrical signals. In this section we focus on the amount of charge generated by high-energy particles in silicon.

### 3.2.1 Bethe-Bloch formula

In silicon, free charge carriers are generated due to thermal effects and lead to leakage current. A current is also generated due to the interaction of charged particles with silicon and can be detected. Part of the absorbed energy generates electron-hole pairs through scattering processes with the shell electrons of silicon and can be collected by the readout electronics. The number of electron-hole pairs produced, as well as the total energy loss of the particle in the detector are stochastic quantities.

The energy loss along the particle track is described by the Bethe-Bloch formula [25]:

$$-\langle \frac{dE}{dx} \rangle = 4\pi N_A r_e^2 m_e c^2 z^2 \frac{Z}{A} \frac{1}{\beta^2} \left[ \frac{1}{2} \ln \frac{2m_e c^2 \beta^2 \gamma^2 T_{max}}{I^2} - \beta^2 - \frac{\delta(\beta\gamma)}{2} \right], \quad (3.1)$$

where the variables are summarised in Table 3.1.  $\beta = \frac{v}{c}$  is the velocity of the particle in units of the speed of light  $c$ ,  $\gamma = 1/\sqrt{1-\beta^2}$  is the Lorentz factor. Relativistic particles with an energy loss near the minimum of the Bethe-Bloch formula are considered as minimum ionising particles (MIPs).

Table 3.1: Summary of the variables used in the Bethe-Bloch formula. From [25].

Symbol	Definition	Units or value
$N_A$	Avogadro's number	$6.0221415(10) \times 10^{23} \text{ mol}^{-1}$
$r_e$	Classical electron radius	$2.817\ 940\ 325(28) \text{ fm}$
$m_e c^2$	Electron mass $\times c^2$	$0.510\ 998\ 918(44) \text{ MeV}$
$z$	Charge of the traversing particle	Units of the electron charge
$Z$	Atomic number of the medium	-
$A$	Atomic mass of the medium	-
$T_{max}$	Maximum kinetic energy that a particle can transfer to a shell electron	eV
$\delta(\beta\gamma)$	Density effect correction to ionisation energy loss	-
$K$	$4\pi N_A r_e^2 m_e c^2$	-
$I$	Mean excitation energy	eV

### 3.2.2 Energy-loss spectrum in silicon

Ionisation is also subject to statistical fluctuations and Equation (3.1) gives its average value. It can be described by a probability density function called *straggling function* and characterised by the most probable energy loss ( $\Delta_p$ ) and full-width-at-half-maximum ( $w$ ). Figure 3.4 shows examples of this distribution in thin sensors. If a particle is not stopped in the sensor, the energy deposition varies around the peak of the distribution with a large tail for high signals. The manifestation of  $\delta$ -rays contributes also to the highly-skewed energy-loss distribution. The  $\delta$ -rays correspond to the electrons which acquire higher ionisation energy by interaction and themselves become ionising particles. The  $\delta$ -rays not only make the average value of the energy-loss higher than the most probable value ( $\Delta_p$ ) of the distribution, but also create big clusters and thus degrade the spatial resolution of the detector. This is the reason why the Bethe Equation (3.1) is ill-defined experimentally and not used for applications where the energy loss for single particles is described.

The fluctuations around  $\Delta_p$  increase for thinner sensors and should be taken into account for the design of the dynamic range of the readout electronics.

In literature, several approaches address the calculation of the straggling functions. The Landau and the Bichsel models, two of the most widely used models, are described in Sections 3.2.3 and 3.2.4.

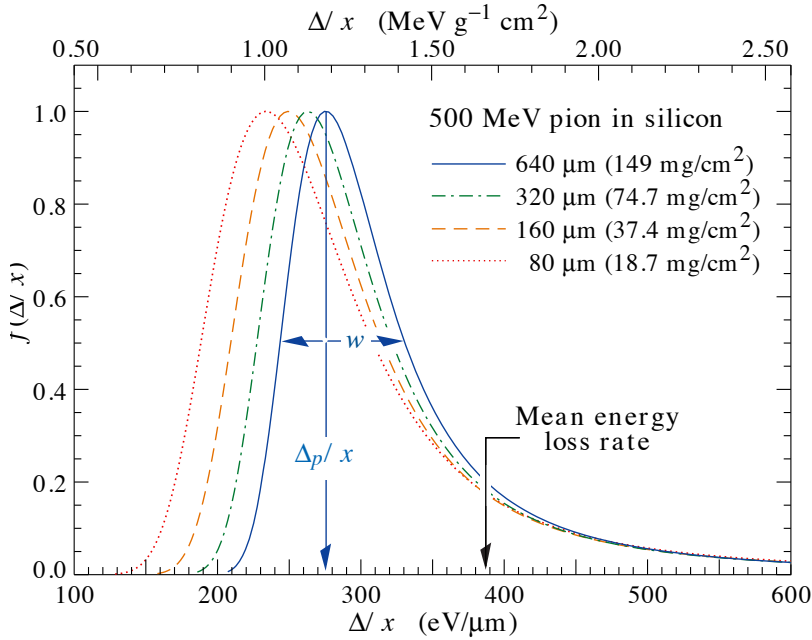


Figure 3.4: Straggling function in silicon for 500 MeV pions, normalized to unity at the most probable value  $\Delta_p$ .  $w$  is the full-width-at-half-maximum [25]. This calculation is based on the Bichsel method (see Section 3.2.4).

The probability of the occurrence of collisions and the probability for a particular energy loss  $E$  are considered for the calculation of the straggling functions. To obtain correct straggling functions, the accurate determination of the collision cross section as function of energy loss,  $\sigma(E)$ , is necessary.

### 3.2.3 The Landau distribution

The energy loss probability in a detector with a moderate thickness can be modeled with the highly skewed Landau distribution. The most probable value  $\Delta_p$  of the distribution is given by the Landau-Vavilov method [26, 27]:

$$\Delta_p = \xi \left[ \ln \frac{2mc^2\beta^2\gamma^2}{I} + \ln \frac{\xi}{I} + 0.200 - \beta^2 - \delta(\beta\gamma) \right], \quad (3.2)$$

where  $\xi = (K/2)\langle Z/A \rangle (x/\beta^2)$  in MeV for a detector of moderate thickness  $x$  in  $\text{g cm}^{-2}$  and other parameters are described in Table 3.1. For thick material, the width of the distribution is given as  $4\xi$ .

For  $\gamma \gg 100$ , Equation (3.2) is simplified to [28]:

$$\Delta_p(\text{keV}) = t(0.1791 + 0.01782 \ln(t)), \quad (3.3)$$

where  $t$  (in  $\mu\text{m}$ ) is the thickness of the silicon sensor.

The Landau-Vavilov calculation defines adequately the  $\Delta_p$  but does not describe correctly the width  $w$  of the energy-loss spectrum especially for thin silicon sensors where the distribution is more skewed [25]. This model is commonly used since it provides an analytical expression of the spectrum with the well-known Landau distribution. However, in data, the energy-loss spectrum for thin sensors is fitted using a

convolution of a Landau distribution with a Gaussian to get a better agreement of the width  $w$ .

### 3.2.4 The Bichsel model

The Bichsel model [28] takes into account the binding of atomic electrons to find a better agreement between data and theory. In this model, experimental and theoretical data for dielectric functions, x-ray absorption coefficients and generalised oscillator strengths are used to reproduce accurately the observed energy loss spectrum over a wide range of incident particle velocities and silicon thicknesses, including very thin silicon sensors. But no analytical description of the straggling function is provided.

Bichsel provides an approximation of  $\Delta_p$  and  $w$  (in eV) as function of the thickness  $t$  (in  $\mu\text{m}$ ) of silicon detectors for particles with charge  $\pm 1e$  and  $\beta\gamma > 500$  as listed in Equations (3.4) to (3.6):

- For  $13 < t < 110 [\mu\text{m}]$ :

$$\Delta_p = t \cdot (100.6 + 35.35 \cdot \ln(t)) , \quad (3.4)$$

- For  $110 < t < 3000 [\mu\text{m}]$ :

$$\Delta_p = t \cdot (190 + 16.3 \cdot \ln(t)) , \quad (3.5)$$

- For  $30 < t < 260 [\mu\text{m}]$ :

$$w = t \cdot (259.6 - 28.41 \cdot \ln(t)) . \quad (3.6)$$

- For  $260 < t < 2560 [\mu\text{m}]$ :

$$w = 71.3t \left(1 + 39.4/t^{0.8}\right) \quad (3.7)$$

Table 3.2 summarises the  $\Delta_p$  and  $w$  for detectors thicknesses at our disposal and tested at test beams with the results presented in the following chapters.

Table 3.2: Calculated  $\Delta_p$  and  $w$  for silicon sensors with various thicknesses using Equations (3.4) to (3.7).

Thickness [ $\mu\text{m}$ ]	$\Delta_p$ [keV]	$w$ [keV]	$\Delta_p/w$
50	11.9	7.42	1.6
100	26.34	12.88	2.045
150	40.75	17.59	2.32

### 3.2.5 Multiple scattering

In addition to energy loss, when a particle goes through the detector, its trajectory is deflected by small-angle scatters. The deflection is mainly due to the Coulomb interaction of the charged particle with the nuclei. For hadrons, there is also a contribution from the strong interaction. When leaving the detector, the scattering angle of most of the particles ( $> 98\%$ ) can be approximated with a Gaussian distribution having an RMS given by [29]:

$$\theta^{\text{RMS}} = \frac{13.6 \text{ MeV}}{\beta p c} z \sqrt{\frac{x}{X_0}} \left[ 1 + 0.038 \ln\left(\frac{x}{X_0}\right) \right], \quad (3.8)$$

where the angle  $\theta$  is in radians, the particle momentum  $p$  in MeV,  $z$  the charge number of the particle and  $x/X_0$  the thickness of the absorption medium in units of the radiation length.

In high-energy physics applications, the amount of material in pixel detectors is minimised in order to have the smallest scattering angles possible.

### 3.3 Transport of charge carriers in silicon

In this section, we review the motion of charge carriers in silicon. First the motion in intrinsic silicon is studied. Then, a pn-junction is described and the motion of charge carriers in silicon detectors is sketched.

In silicon detectors, the movement of the charge carriers (holes and electrons) leads to signal pulses in the electrical contacts which can be detected by the readout electronics. In the absence of any external electric field, free charge carriers move randomly and are scattered due to their collisions with the crystal lattice or other impurities. On average, in equilibrium conditions, the traveled distance averaged over charges is zero. In addition to the statistical movement, two other mechanisms can affect the transport of charge carriers: diffusion (due to a gradient in concentration) and drift (in the presence of an external electric field).

The diffusion implies that a carrier is more probable to move from a high-concentration region to a low-concentration region. The diffusion current per unit area is given by [30]:

$$\begin{aligned} J_{n,diff} &= -\frac{kT}{e}\mu_n \nabla n && \text{for electrons ,} \\ J_{p,diff} &= \frac{kT}{e}\mu_p \nabla p && \text{for holes ,} \end{aligned} \quad (3.9)$$

where  $k$  is the Boltzmann constant,  $T$  the absolute temperature,  $e$  the elementary charge,  $\mu$  the mobility of the charge carriers,  $\nabla n$  and  $\nabla p$  are the gradients of the electron and hole concentrations.

Charge carriers are accelerated between two random collisions in the presence of an external electric field in the direction of the field, leading to an average drift velocity given by [30]:

$$\begin{aligned} v_n &= -\mu_n \mathbf{E} && \text{for electrons ,} \\ v_p &= \mu_p \mathbf{E} && \text{for holes ,} \end{aligned} \quad (3.10)$$

where  $v$  is the average drift velocity,  $\mathbf{E}$  the electric field and  $\mu$  the mobility of the charge carriers. The mobility is a function of the electric field. For higher electric fields, the charge carriers gain more acceleration and the number of collisions per unit time increases. This leads to a saturation of the drift velocity  $v_s$ . The dependence of the mobility on the electric field is described by [31]:

$$\mu(E) = \frac{v_s/E_c}{[1 + (E/E_c)^\beta]^{1/\beta}} , \quad (3.11)$$

where the parameters are described in Table 3.3.

Table 3.3: Parameters for the mobility as described in Equation (3.11) with  $T$  the absolute temperature and  $E$  the absolute value of the electric field.

Parameter	Electrons	Holes	unit
$v_s$	$1.53 \times 10^9 \times T^{-0.87}$	$1.62 \times 10^8 \times T^{-0.52}$	cm/s
$E_c$	$1.01 \times T^{1.55}$	$1.24 \times T^{1.68}$	V/cm
$\beta$	$2.57 \times 10^{-2} \times T^{0.66}$	$0.46 \times T^{0.17}$	-

Figure 3.5 shows the mobility for electrons and holes as a function of the electric field. For a low

electric field, the mobility for intrinsic silicon at 300 K is:

$$\begin{aligned}\mu_n &= 1415 \pm 46 \quad \text{cm}^2/(\text{Vs}), \\ \mu_p &= 480 \pm 17 \quad \text{cm}^2/(\text{Vs}).\end{aligned}$$

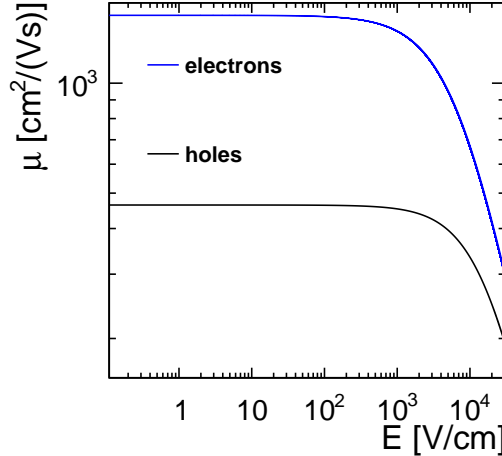


Figure 3.5: Mobility for electrons and holes as a function of an applied electric field calculated with Equation (3.11).

Holes are three times less mobile than electrons which make them more likely to be trapped in impurities. This is of particular importance after radiation exposure [30].

### 3.3.1 pn-junction in thermal equilibrium

By joining a p-type with an n-type material, a pn-junction is obtained. The p and n-type regions are initially electrically neutral. Due to thermal diffusion, the holes and the electrons are driven across the junction. This implies that electrons move from the n-type material to the p-regions leaving a positive net charge in n-regions, while the p-type region gets negatively charged. A potential is built up when the electrons diffuse to the p-region. This potential limits the diffusion depth when it exceeds the available energy for thermal diffusion and is called the built-in potential  $V_{bi}$  between the p and n-regions. The built-in potential depends logarithmically on the doping levels [24]:

$$V_{bi} = \frac{kT}{e} \log \left( \frac{N_a N_d}{n_i^2} \right), \quad (3.12)$$

where  $N_a$  and  $N_d$  are the acceptor and donor concentrations and  $n_i$  is the intrinsic silicon carrier concentration. For a typical detector diode  $V_{bi} \approx 0.5$  V.

The diffusion of the holes and electrons across the junction to the oppositely-doped regions leads to a region free of mobile carriers called the depletion region. As seen previously,  $V_{bi}$  limits the diffusion depth and therefore the width of the depletion region.

Applying an external potential breaks down the thermal equilibrium. By applying a reverse bias potential, i.e. negative potential to the p-region and positive potential to the n-region, the potential barrier and the depletion width are increased.

Under a forward bias on the pn-junction, the diode current increases rapidly with the voltage. A reverse bias, on the other hand, causes a quick saturation of the current flow within the junction. The pn-diode

can therefore be used as a rectifier. The reverse bias mode with large depletion depth is used for the detection of radiation in silicon detectors as described in the next section.

### 3.3.2 Reverse-biased pn-junction

The application of a reverse bias voltage to a pn-junction is crucial in the detection of radiation in silicon detectors. It increases the depletion width. This forms a capacitor depleted of charge carriers where the undepleted p and n-regions are the electrodes and the depletion region is the dielectric. An electric field due to the bias voltage is established in the depletion region. The charges generated due to the incident radiation follow the electric fields and are collected by the readout electrode.

Here, we derive the depletion width, the electric field distribution, the drift and the diffusion within a pn-junction reverse-biased at a voltage of  $V_B$ .

The potential  $\varphi$  at each point is described by Poisson's equation [32]:

$$\nabla^2 \varphi = -\frac{\rho}{\epsilon}, \quad (3.13)$$

where  $\epsilon$  is the dielectric constant of the medium and  $\rho$  the net charge density. The electric field  $E$  due to the electric potential is obtained by:

$$E = -\text{grad } \varphi. \quad (3.14)$$

To simplify, as illustrated in Figure 3.6, we assume an abrupt junction where the charge densities on the p and n-regions are given by:

$$\rho(z) = \begin{cases} eN_d, & \text{if } 0 \leq z < z_n \\ -eN_a, & \text{if } z_p \leq z < 0 \end{cases}. \quad (3.15)$$

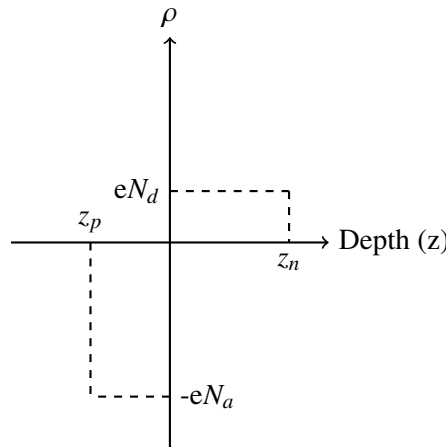


Figure 3.6: Charge density distribution for a simplified pn-junction where  $N_a$  and  $N_d$  are the acceptor and the donor concentrations.

In one dimension, Poisson's equation is simplified to:

$$\frac{d^2 \varphi(z)}{dz^2} = -\frac{\rho(z)}{\epsilon}. \quad (3.16)$$

First, considering the n-side, the first and second integrations of the Poisson equation give:

$$\frac{d\varphi(z)}{dz} = -\frac{eN_d}{\epsilon}(z - z_n) \quad \text{for } 0 \leq z < z_n , \quad (3.17)$$

$$\varphi(z) = -\frac{eN_d}{\epsilon} \frac{z^2}{2} + \frac{eN_d z z_n}{\epsilon} + V_j \quad \text{for } 0 \leq z < z_n , \quad (3.18)$$

where  $V_j$  is the potential at the interface where the n- and the p-sides join. At the boundary of the depletion region  $z = z_n$  the bias voltage  $V_B$  is applied:

$$\varphi(z_n) = V_B = \frac{eN_d z_n^2}{2\epsilon} + V_j . \quad (3.19)$$

At the p-side, the external bias voltage is 0 V. Using this constraint in the p-region, the  $V_j$  is given by:

$$V_j = \frac{eN_a z_p^2}{2\epsilon} . \quad (3.20)$$

The total potential across the pn-junction is given by:

$$V_B = \frac{e}{2\epsilon} (N_d z_n^2 + N_a z_p^2) . \quad (3.21)$$

The charge density in the p- and n-regions should be the same to maintain the overall charge neutrality:

$$N_d z_n = N_a z_p . \quad (3.22)$$

Using the neutrality condition, the reverse bias potential can be expressed as:

$$V_B = \frac{e}{2\epsilon} \left( 1 + \frac{N_a}{N_d} \right) N_a z_p^2 = \frac{e}{2\epsilon} \left( 1 + \frac{N_d}{N_a} \right) N_d z_n^2 . \quad (3.23)$$

The depletion widths on the n- and p-sides of the junction are given by:

$$z_n = \sqrt{\frac{2\epsilon V_B}{eN_d(1 + N_d/N_a)}} \quad (3.24)$$

$$z_p = \sqrt{\frac{2\epsilon V_B}{eN_a(1 + N_a/N_d)}} .$$

The total depletion width  $W$  is given by:

$$W = z_n + z_p = \sqrt{\frac{2\epsilon V_B (N_a + N_d)}{eN_a N_d}} . \quad (3.25)$$

Considering an asymmetrical junction with  $N_d \ll N_a$  for which the junction potential is equal to the potential of the p-contact:

$$V_j = \left( \frac{N_d}{N_a} \right) \frac{V_B}{(1 + N_d/N_a)} \underset{N_d \ll N_a}{\approx} \frac{N_d}{N_a} V_B . \quad (3.26)$$

Let's consider a pixel detector with asymmetric junction with a highly doped surface  $N_c$  concentration and a lightly doped bulk  $N_b$  ( $N_b \ll N_c$ ).  $N_c$  and  $N_b$  are used for a generalisation of the doping regions

and each can consist of donors or acceptors. The bulk resistivity  $\rho_b$  is expressed in terms of the doping concentration:

$$\rho_b = \frac{1}{e\mu_b N_b} , \quad (3.27)$$

where  $\mu_b$  and  $N_b$  are the mobility and the doping concentration of the bulk. The depletion width  $W$  becomes:

$$W = \sqrt{2\epsilon\mu_b\rho_b V_B} . \quad (3.28)$$

By taking into account the built-in reverse bias voltage, Equation (3.28) is written as:

$$W = \sqrt{2\epsilon\mu_b\rho_b (V_B + V_{bi})} = \sqrt{\frac{2\epsilon(V_B + V_{bi})}{eN_b}} . \quad (3.29)$$

The electric field of Equation (3.17), by replacing the depletion width and  $N_d$  by Equation (3.29), can be expressed as:

$$E(z) = \frac{2(V_B + V_{bi})}{W} \left( \frac{z}{W} - 1 \right) . \quad (3.30)$$

The bulk of the detector becomes fully depleted of charge carriers when the depletion width  $W$  equals the thickness of the detector  $d$  ( $W = d$ ). The depletion  $V_D$  voltage can be expressed as:

$$V_D = \frac{eN_b d^2}{2\epsilon} - V_{bi} . \quad (3.31)$$

The built-in voltage has a typical value of  $V_{bi} \approx 0.5$  V. Since  $V_B$  is much higher than  $V_{bi}$ , then  $V_{bi}$  can be neglected. The electric field drops linearly from its maximum value at the junction to zero at the opposite contact. Increasing the bias voltage beyond the needed bias to completely deplete the detector adds a uniform field. The electric field can be written as:

$$E(z) = \frac{V_B - V_D}{d} + \left( 1 - \frac{z}{d} \right) 2 \frac{V_D}{d} . \quad (3.32)$$

The electric field, as calculated in Equation (3.32), is valid for the depleted region where  $0 < z < d(V_B + V_D)/(2 \cdot V_D)$ . If the bias voltage is lower than the depletion voltage, the electric field is 0 in the undepleted region. For this model, the charge generated in the undepleted region is not collected by the readout placed at  $z = 0$  and therefore it is lost.

The charge carriers, under the influence of the electric field, drift through the silicon detector with a velocity as defined by:

$$\vec{v}_{drift} = \mu_c \cdot \vec{E} . \quad (3.33)$$

In one-dimension, and considering  $\mu_c$  constant by neglecting the saturation effect at high electric fields, the drift velocity is written as:

$$v_{drift} = \frac{dz}{dt} = \mu_c \cdot E(z) . \quad (3.34)$$

The drift time required for a charge originating at point  $z$  to reach the point  $z_0$  where the charge is collected is:

$$t_{drift}(z) = \int_z^{z_0} \frac{ds}{\mu_c \cdot E(s)} . \quad (3.35)$$

With the assumptions on the electric field and the mobility, the integral above can be solved analytically. Assuming  $z_0 = 0$  corresponds to the readout electrode, one obtains the drift time for a charge generated

at a depth  $z$  as:

$$t_{drift}(z) = \frac{d^2}{2\mu_c V_D} \ln \left( \frac{V_B + V_D}{V_B + V_D - 2V_D z/d} \right). \quad (3.36)$$

During the drift, the charge carriers do not exactly follow the electric field lines. They also diffuse due to the random thermal motion in the crystal lattice. The spread of the charge carriers at the readout ( $z = 0$ ) and produced at a position  $z$  can be expressed as a Gaussian distribution with a standard deviation  $\sigma_{diffusion}$  of [33]:

$$\sigma_{diffusion}(z) = \sqrt{2D_b t_c} = \sqrt{\frac{kT d^2}{eV_D} \ln \left( \frac{V_B + V_D}{V_B + V_D - 2V_D z/d} \right)}, \quad (3.37)$$

where  $D_b$  is the diffusion constant and related to the mobility via the Einstein equation  $D_b = \mu_c \cdot k_b \cdot T / e$ .

The drift time depends on the mobility of the charge carriers as shown in Equation (3.36). Figure 3.7(a) compares the drift time for n and p-type carriers in a 50 μm thick silicon sensor with a depletion voltage of  $|V_D|=4$  V and biased at  $|V_B|=15$  V for a charge created at a position  $z=\text{depth}$ . The electrons have a higher drift velocity and therefore are faster for readout. Diffusion does not depend on the carrier type as it can be seen in Equation (3.37). Figure 3.7(b) shows the standard deviation for the diffusion at different bias voltages for the n and p-type carriers.

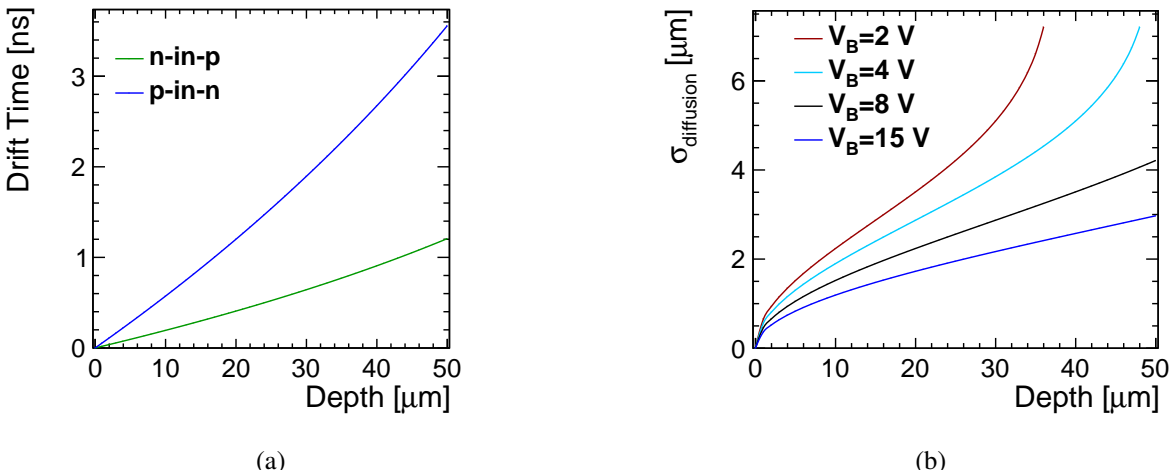


Figure 3.7: (a) Drift time and (b) diffusion standard deviation for n and p-type carriers for a charge created at the depth  $z$  in the sensor. The diffusion is shown for different bias voltages and does not depend on the carrier type. The depletion voltage is  $|V_D|=4$  V and the drift time is calculated considering a bias voltage of  $|V_B|=15$  V.

Figure 3.8 shows the electric field and the mobility distribution as a function of the depth in a 50 μm thick silicon sensor with a depletion voltage of  $|V_D|=4$  V and biased at  $|V_B|=15$  V. The mobility in this case stays almost constant and does not reach the saturation effects due to the electric field since in this case the electric field stays quite low.

### 3.4 Pixelated silicon sensors

Previously, we have reviewed the properties of a pn-junction as it is the building block of pixel detectors. By segmenting the electrodes on a pn-junction a pixel detector is obtained. The highly doped electrodes,

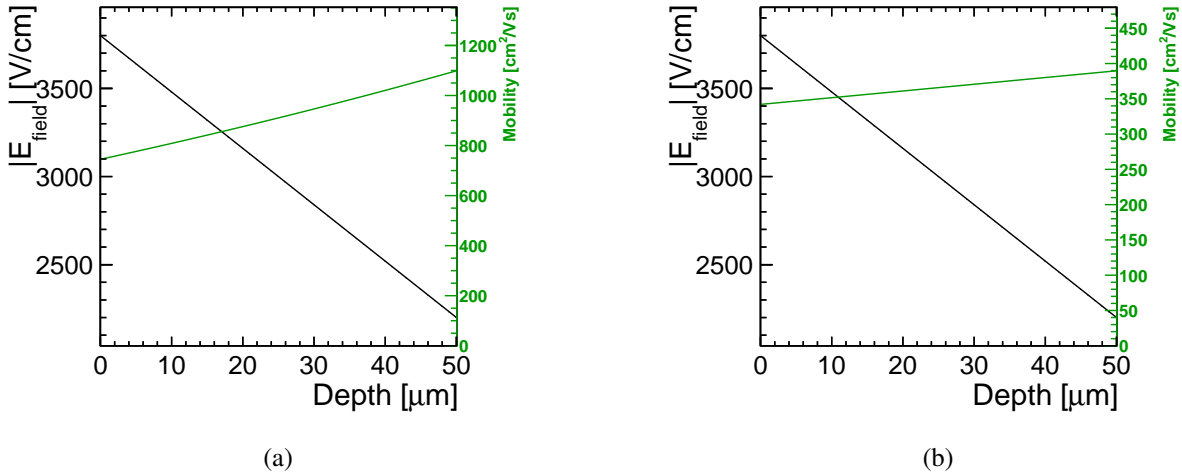


Figure 3.8: The electric field and the mobility as a function of the depth for (a) n-type carriers and (b) p-type carriers.

which can be n or p-type, are introduced through a mask to form a pixel matrix with ion implantation. Each pixel forms an independent pn-junction and the gaps between the pixels are electrically controlled to isolate a pixel from its neighbouring diodes. An aluminum layer deposited on the electrodes provides a signal path to the readout electronics with a low resistance. The backside metallisation, on the bulk side, supplies the external bias voltage.

This thesis focuses on hybrid pixel detectors where the electronics for the readout and sensors are produced separately and mated using bump bonds. Matrices of pixel detectors can be put together to cover larger surfaces. Figure 3.9 illustrates schematically a hybrid pixel detector. An ionising particle traversing the detector creates charges in the depletion region of the sensor. The charge carriers move under the action of the applied electric field. The signal produced is acquired by an integrated circuit for amplification and digitisation. The readout chip is also responsible to discriminate noise levels from the particle hits. This is achieved by comparing the signal amplitude to a discriminating threshold.

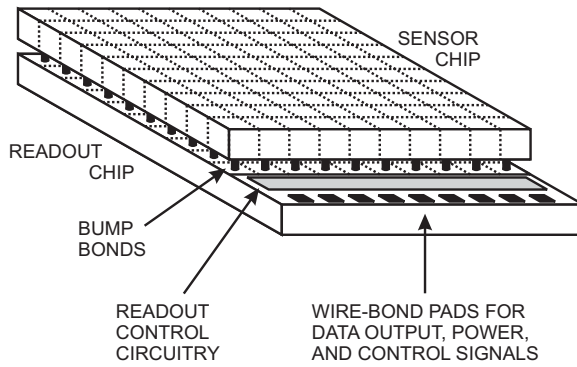


Figure 3.9: Schematic layout of a hybrid pixel detector. A pixellated sensor is bump-bonded to a readout chip. Wire-bonds are used for external connections. From [24].

In the following sections, we introduce Ramo's theorem which describes the induced current at the

readout electrode due to the movement of the charge carriers. Also, an introduction to in-pixel studies done with pixel detectors is given later when studying the spatial resolution for different readout chip configurations. We also explain how pixel detectors can be used for position reconstruction.

### 3.4.1 Charge collection and Ramo's theorem: induced charge

Previously, we have seen that due to incident radiation, a signal is produced by the motion of charge carriers in the detector. We can naively interpret this statement such that the signal is formed with a delay when the charge carriers are collected by the electrodes. But in reality, such a delay does not exist and an induction signal pulse is created immediately after a charge carrier starts its motion to the electrodes. When the last charge carriers arrive at the collecting electrodes, the charge induction process ends and the signal pulse is fully developed. The timing evolution of the signal is important in understanding the timing properties of detectors. In the following, we derive the induced charge in a pixel detector.

For the calculation of the induced charge, we first consider the simple example of a charge  $q$  near an infinitely large electrode with all the electric field lines terminating on the electrode. Gauss's law, for a surface  $S$  surrounding the charge is expressed as [24]:

$$\oint_S \vec{E} \cdot d\vec{a} = q. \quad (3.38)$$

The induced charge obtained by integrating over a Gaussian surface enclosing only the electrode is  $-q$ . Now, let's consider two parallel electrodes with a charge  $q$  in between as shown in Figure 3.10. If the charge is placed midway between the two parallel plates, it induces equal charge of  $-q/2$  on both electrodes as half of the electric field lines end up on the higher and the other half on the lower electrode. When the charge moves closer to a plate rather than the other, the induced charge will be higher for the closer plate.

The induced charge can not be observed directly but its change can be measured when the two electrodes are connected in a closed circuit (like in a pixel detector) as it produces an induced current.

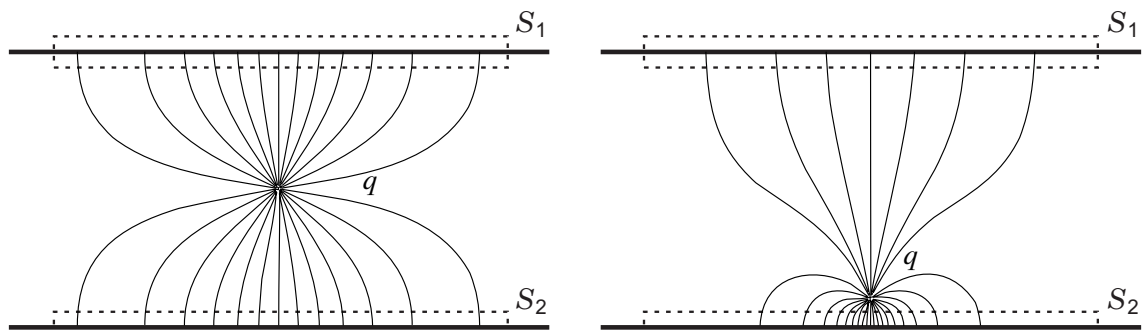


Figure 3.10: The charge induced on two parallel plates for two configurations of the position of a charge  $q$ . From [24].

Ramo's theorem [34] describes the time evolution of the induced current created in a detector. The induced current on the electrodes is described as a function of the weighting potential  $\Phi$  which describes the coupling of a charge to an electrode. The weighting potential is defined for a specific electrode configuration. In Ramo's theorem, it is obtained by setting the potential of the electrode to unit potential and setting all other electrodes to zero potential. Equation (3.39) describes the induced charge  $Q_k$  on electrode  $k$  if a charge  $q$  moves along any path from the originating point  $z_0$  to the readout electrode

position  $z_p$  [24]:

$$Q_k = q \cdot [\Phi_k(z_p) - \Phi_k(z_0)] . \quad (3.39)$$

The instantaneous current on the electrode  $k$  is given by [24]:

$$i_k = q \cdot v \cdot E_k , \quad (3.40)$$

where  $v$  is the velocity of the charge carrier and  $E_k$  the weighting field.

It is important to note that the weighting potential (field) is different from the electric potential (field). The electric field determines the drift trajectory and velocity of the charge carriers whereas the weighting field depends only on the geometry of the electrodes and defines how the charge motion induces a charge to a specific electrode. The induced charge is independent of the trajectory. In the specific case of a two-electrode configuration the electric and the weighting fields are the same.

Figure 3.11 shows the weighting field and potential distributions calculated using TCAD simulations [35] (c.f. Section 5.3). For this study, we consider a p-in-n silicon sensor with 5 pixels (marked out with dashed lines), having a thickness of 200  $\mu\text{m}$  and over-depleted with a bias voltage of 50 V on the back-side. First, 0 V is applied to all the electrodes and then 1 V is applied to the electrode  $k$ . By subtracting the electric field and the electrostatic potential in the two configurations, the weighting field and potential are obtained.

The gradient of the weighting potential gets higher by getting closer to the pixel. This indicates that the pixel is more sensitive to the charges drifting close by. In contrast, the gradient of the weighting potential is relatively flat in the bulk implying that the charges drifting far from the pixel contribute less to the induced signal.

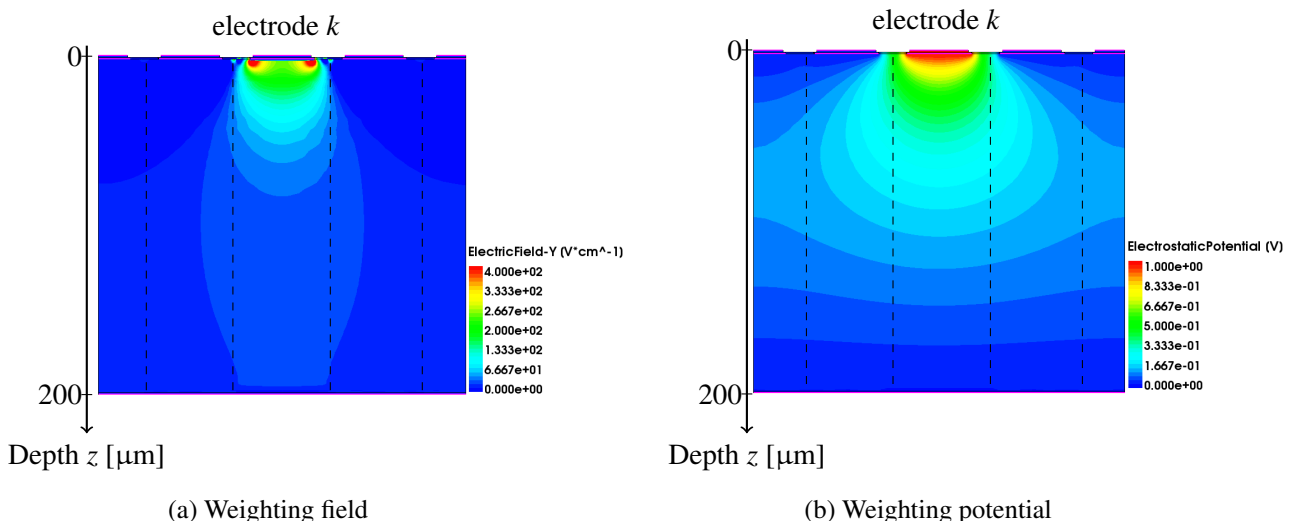


Figure 3.11: The weighting field and potential on electrode  $k$ .

### 3.4.2 Position measurement

A pixel detector is obtained by segmenting the electrodes of a silicon sensor. This provides a two-dimensional information on the position of particle tracks. The magnitude of the signal measured by an electrode depends on the track position within a pixel. If the particle hits close to the edges or corners of a pixel, multiple pixels can detect signals and result in clusters.

The spatial resolution of a pixel detector is mainly determined by the pixel pitch. But it can be improved by the readout choice (binary or analogue with pulse-height information), the detection threshold of the readout, the charge sharing in the sensor, the thickness of the detector and the reconstruction algorithm. The effect of the readout on the spatial resolution is studied in this section.

In the following, the calculations are only done in one-dimension and we assume that tracks pass through the center of the pixel in the other dimension. The spatial resolution is therefore defined by:

$$\sigma_{position}^2 = \frac{\int_{-p/2}^{p/2} (x_r - x_m)^2 D(x_r) dx_r}{\int_{-p/2}^{p/2} D(x_r) dx_r}, \quad (3.41)$$

where  $\sigma_{position}$  is the average distance between the real impact position  $x_r$  and the measured position  $x_m$  of the particle in a pixel.  $D(x)$  is the hit probability density function in a pixel and  $p$  represents the pixel pitch.

### Binary readout

The simplest (and unrealistic) case for the resolution computation is to consider a binary readout with single readout threshold for signal and noise discrimination. For a pixel centered at 0 and having a pitch  $p$  with a hit probability density function as illustrated in Figure 3.12, the following assumptions are considered:

- The threshold is adjusted in a way to fire one pixel per particle track.
- Only hit positions between  $-p/2$  and  $p/2$  trigger a signal in pixel 0.
- A uniform density of particles hit the detector ( $D(x) = 1$ ).

Under these assumptions, the readout electronic noise, the readout threshold dispersion, the diffusion and the energy deposition fluctuations are neglected.

The average difference between the real position ( $x_r$ ) and the measured position ( $x_m = 0$ ) of the particle in a pixel is calculated using Equation (3.41) [30]:

$$\sigma_{position}^2 = \frac{\int_{-p/2}^{p/2} (x_r)^2 1 dx_r}{\int_{-p/2}^{p/2} 1 dx_r} = \frac{p^2}{12}, \quad (3.42)$$

which results in a spatial resolution of:

$$\sigma_{position} = \frac{p}{\sqrt{12}}. \quad (3.43)$$

In this simple model, the resolution achieved is only dependent on the pitch size (geometry of the pixels). In reality, the signal of a particle track is shared between several pixels and depending on the readout threshold more than one pixel can be fired. The resolution is therefore improved as described in the following.

### Binary readout and charge sharing

The threshold of the readout electronics is usually set as low as possible which can result in more than one pixels hit per particle track. In this case, the charge is shared between two or more pixels and result

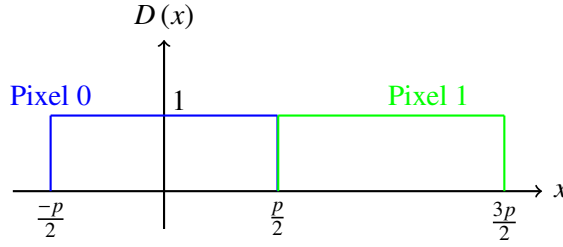


Figure 3.12: The hit probability density function for two neighbouring pixels (pixel 0 and pixel 1) when a binary readout is used to acquire the sensor pulse.

in clusters. Multi-pixel clusters can improve the resolution of Equation (3.43). Figure 3.13 illustrates the charge sharing between two pixels. If a track passes close to the edge of a pixel (within a distance of  $\frac{s}{2}$  close to the edge), the neighbouring pixel is also fired. For events triggering single-pixel events, the spatial resolution in pixel 0 for 1-pixel clusters is given by:

$$\sigma_{position}^2 = \frac{\int_{-(p/2-s/2)}^{(p/2-s/2)} (x_r)^2 1 dx_r}{\int_{-(p/2-s/2)}^{(p/2-s/2)} 1 dx_r} = \frac{(p-s)^2}{12}. \quad (3.44)$$

For two-pixel clusters, the spatial resolution is given by:

$$\sigma_{position} = \frac{s}{\sqrt{12}}. \quad (3.45)$$

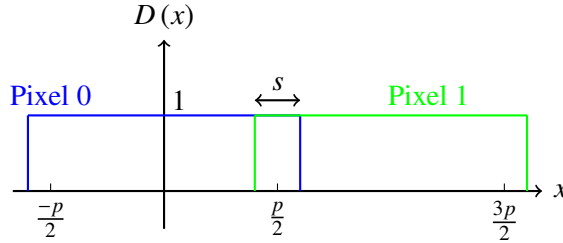


Figure 3.13: The hit probability density function for two neighbouring pixels (pixel 0 and pixel 1) considering charge sharing between the two pixels when a binary readout is used to acquire the sensor pulse as explained in the text.

The average resolution considering single and multi-pixel clusters is given by:

$$\sigma_{Total}^2 = \frac{p^2 - 3ps + 3s^2}{12}. \quad (3.46)$$

The optimal average spatial resolution is obtained for  $s = p/2$  as shown in Figure 3.14 for two pixel pitches of  $p = 25 \mu\text{m}$  and  $p = 55 \mu\text{m}$ . This means that the number of single-pixel and multi-pixel clusters is the same. Note that, in this situation one is not able to distinguish between one track triggering two pixels and two tracks hitting the sensor within  $2p$  for very high rate hits.

For the CLIC pixel detector, the aim is to achieve a resolution of  $3 \mu\text{m}$  with a pixel pitch of  $25 \mu\text{m}$ . With this simple example we see that, in the optimal case of  $s = p/2$ , the resolution achieved would be  $\sim 3.6 \mu\text{m}$ . For this pitch, charge sharing is crucial in order to achieve such a challenging resolution.

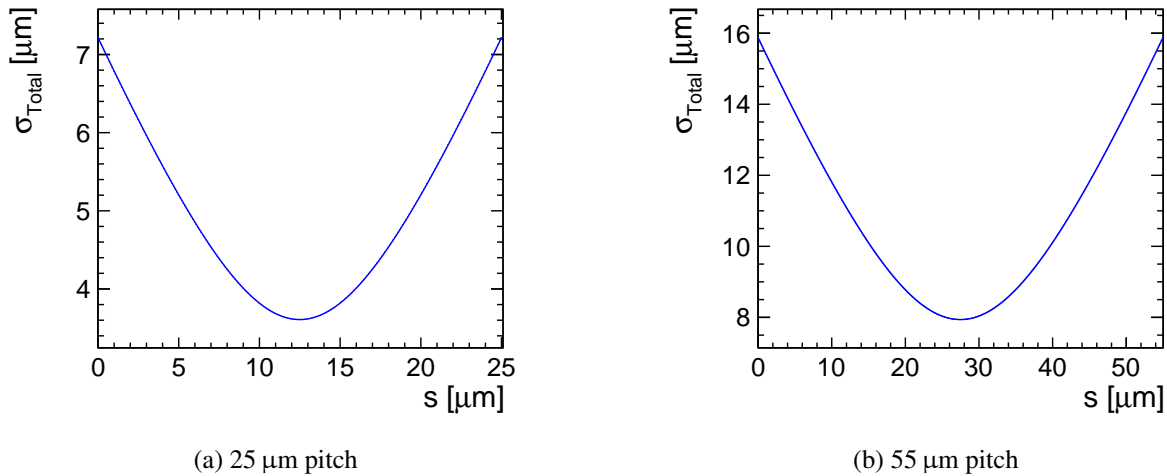


Figure 3.14:  $\sigma_{\text{Total}}$  calculated using Equation (3.46) with a pixel pitch of (a)  $p = 25 \mu\text{m}$  and (b)  $p = 55 \mu\text{m}$  where  $s$  is the width of the charge sharing region as shown in Figure 3.13.

### Analogue readout and charge sharing

The spatial resolution can be significantly improved with an analogue readout which delivers a signal proportional to the collected charge as illustrated in Figure 3.15. In this case, for multi-pixel clusters the  $\eta$ -function [36] (c.f. Section 3.4.3) is used to reconstruct the hit position within the pixels using the charge information. In the region where only one pixel fires, the resolution is still limited to  $\frac{(p-s)}{\sqrt{12}}$ . Therefore the readout threshold should be as low as possible in order to detect the smallest amounts of charge reaching neighbouring pixels.

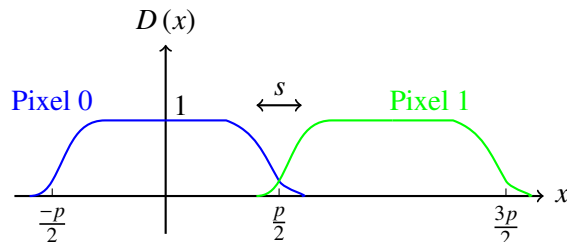


Figure 3.15: The hit probability density function for two neighbouring pixels (pixel 0 and pixel 1) considering charge sharing between the two pixels using an analogue readout to acquire the sensor pulse.

This case is closer to the reality in hybrid pixel detectors with analogue readout. The readout noise plays an important role in the spatial resolution as it affects the operating threshold. The spatial resolution is proportional to the signal-to-noise ratio [37]:

$$\sigma \propto \frac{p}{S/N}, \quad (3.47)$$

where the signal  $S$  is measured as the most-probable-value of the MIPs distribution of clusters and  $N$  the noise of a pixel.

For this realistic case, there is no analytic solution for the calculation of the resolution. Simulations can be done to calculate the spatial resolution numerically. Section 5.2 presents the simulation framework

which allows for the simulation of a sensor and its readout in a pixel detector and therefore obtain the spatial resolution.

### 3.4.3 Hit position reconstruction using the $\eta$ -correction method

Previously, through simple examples, we have seen the benefits of charge sharing on the spatial resolution. In fact, due to the charge sharing, particle tracks create multi-pixel clusters. The amount of charge deposited in each pixel can be measured using an analogue readout. The  $\eta$ -correction method uses the charges in the hit pixels as weights to reconstruct the particle hit position within a pixel. This method takes into account non-linearities in the charge sharing between pixels [36].

This method can be implemented in different ways for the reconstruction of the particle hit within a pixel. In this thesis, the method as described in [38] is used for the data and simulations reconstruction and summarised in the following. The  $\eta$ -correction method calculates the distance with which the hit position moves from the geometric centre of two pixels in a cluster. This shift is calculated as:

$$\text{shift} = \sigma_{EC} \times \text{erf}^{-1}(2 \times Q_{rel} - 1), \quad (3.48)$$

where  $\sigma_{EC}$  is a parameter to be determined and depends on several factors such as the thickness of the silicon sensor and the operating conditions of the assembly. The inverse error function is defined as  $\text{erf}^{-1}(z)$  with:

$$\text{erf}(z) = \frac{2}{\sqrt{\pi}} \int_0^z e^{-t^2} dt. \quad (3.49)$$

In Equation (3.48),  $Q_{rel}$  is the charge of the pixel with the highest charge divided by the total charge of the cluster ( $Q_{max}/Q_{tot}$ ).



# CHAPTER 4

---

## Pixel readout ASICs and assembly calibration

---

One of the key components of the detector systems is the readout electronics. Each experiment, depending on the requirements, has its own specific electronics.

In this chapter, we will review the basic principles and requirements of the Timepix3 hybrid pixel readout chip which is used as a test vehicle to study thin and active-edge sensors as described in the following chapters. The calibration method for the Timepix3 assemblies and also the noise measurements are explored in this chapter.

### 4.1 The Timepix3 hybrid readout ASICs

The hybrid readout chip acquires the short ionisation current pulses generated in the sensor by the passing of a charged particle. For acquiring this short pulse, the time response of the readout must be tailored to optimise the minimum detectable signal, the measurement of energy deposition in the detector, the event rate capability, timing measurement of the signal and the insensitivity of the system to the pulse shape. Finally, the signal is digitised and stored. Robustness to radiation and low power consumption are other important considerations to be addressed amongst others.

The Timepix [3, 39] hybrid pixel detector readout chip family, designed by the Medipix collaboration [40], is a general purpose front-end electronics and can measure precisely the energy deposited in the sensor and also provides accurate timing information. These chips are used in a wide range of applications such as high energy physics and medical imaging. The Timepix3 ASIC is deployed for the CLIC vertex detector R&D to study the feasibility of thin sensors and also active-edge sensors as described in the coming chapters.

Figure 4.1 schematically shows the basic signal flow in a Timepix3-like hybrid pixel detector. Both analogue and digital circuitry are combined for signal processing.

The incident radiation deposits energy in the sensor which is converted to an electrical signal. A high rate of particles can be handled in a semiconductor detector because the sensor pulse is very short (few nanoseconds). A charge sensitive preamplifier is needed to amplify the short signal pulse. As seen in Section 3.2, the amount of signal charge is small and subject to statistical fluctuations. The preamplifier should be designed in a way to minimise the electronics noise (see Section 4.3 for a discussion of the noise sources). The sensor capacitance and the input capacitance of the amplifier play a critical role in the optimisation of the signal-to-noise ratio (SNR): the lower the capacitance, the higher the SNR.

The preamplifier is implemented in a Krummenacher topology [41], where the return to the baseline of the amplified signal is done with a tunable current ( $I_{\text{krum}}$ ). The higher  $I_{\text{krum}}$ , the faster the return and the shorter the pulse. For the Timepix readout chip family, a pulse shaper is embedded in the preamplifier

which outputs a triangular-like pulse shape where the rising edge is imposed by the time response of the preamplifier and the slope of the falling edge dictated by the  $I_{\text{kum}}$  current.

A discriminator is used to compare the signal level to a tunable threshold voltage and to discriminate signal from background noise. Both polarities (electrons and holes) are accepted by the front end.

When the pulse height passes the threshold in the discriminator, counters in the digital part of the readout chip are incremented to measure the energy and the arrival time of the signal.

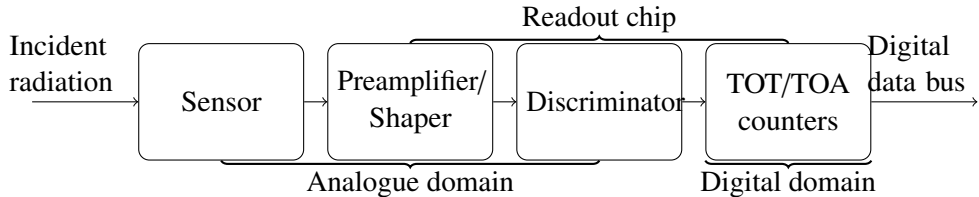


Figure 4.1: Schematic overview of basic signal flow in a Timepix-like hybrid pixel detector. The energy deposited in the sensor by the incident radiation is converted to an electrical signal. The signal is integrated in the preamplifier, shaped by the pulse shaper and compared to a programmable threshold by the discriminator. The digital part of the readout chip digitises the signal for storage and analysis using counters for timing and energy measurements.

An overview of the main parameters of the Timepix3 readout chip is given in Table 4.1. It consists of a  $256 \times 256$  pixel matrix with a pitch of  $55 \mu\text{m}$ . This chip allows for three operation modes: photon counting (PC), Time-over-threshold (TOT) and Time-of-arrival (TOA) measurements. In addition, Timepix3 allows for simultaneous measurement of the TOT and the TOA. In the photon counting mode, a counter is incremented each time a photon hits the pixel and deposits an energy higher than the programmable threshold.

Table 4.1: Overview of the main parameters of the Timepix3 readout ASIC.

Pixel Matrix	$256 \times 256$
Pixel Pitch	$55 \mu\text{m}$
Technology	130 nm CMOS
Measurement Modes	10 bit TOT and 18 bit TOA 18 bit TOA only 10 bit PC and 14 bit integral TOT
Clock speed	Up to 40 MHz for TOT and general TOA 640 MHz for FTOA
Readout Type	Data driven or Frame based
Electronic Noise (without sensor)	< 70 e <sup>-</sup> RMS

Figure 4.2 schematically shows the energy and the timing measurements of the signal. The Time-over-threshold (TOT) allows for the measurement of the energy deposited in a pixel. The time above the programmable threshold of the triangular-like signal pulse is proportional to the energy deposited and during this time, the TOT counter is incremented.

The Time-of-arrival (TOA) measures the arrival time of a hit and is used for a time stamping of the hits. A general TOA counter runs with the general 40 MHz clock. When the amplifier output exceeds the pixel threshold, the discriminator output rises and the fast TOA (FTOA) 640 MHz counter runs until the rising edge of the general clock. A combination of the global TOA counter and the FTOA counters is used to calculate the arrival time of the hits (or the pixel TOA). The FTOA counter is also used to

increase the precision of the TOT measurement.

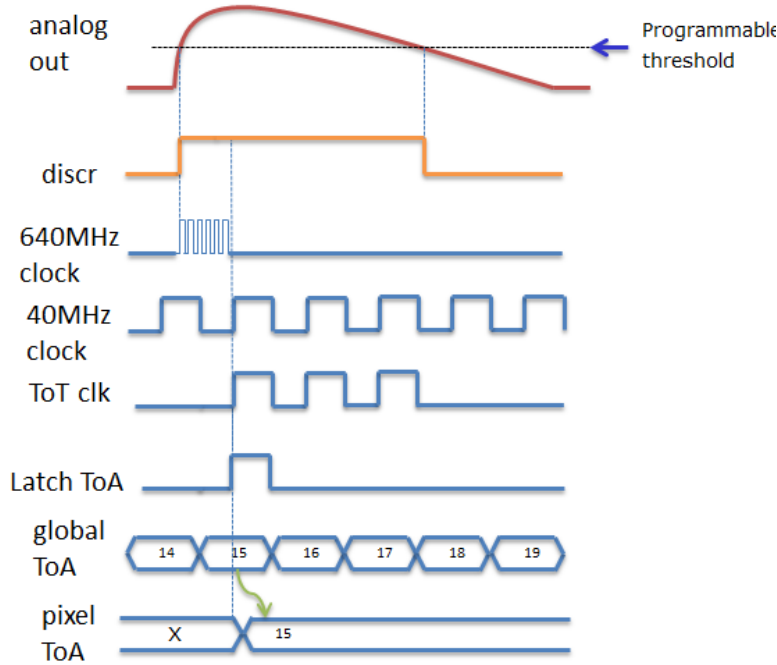


Figure 4.2: Schematic overview of the Time-over-threshold (TOT) and Time-of-arrival (TOA) measurements for the Timepix3 readout chips. From [3].

The Timepix3 readout chip allows for a data-driven zero-suppressed readout mode which can reach higher readout rates than the frame based mode.

In the frame based mode, pixels record hits during the time the shutter is open. After this time, the information of the whole matrix is read at once. During the time the information is being read, the chip is not able to process any hits.

In the data driven mode, after a hit is processed by the pixel, a data packet containing the TOT and the TOA information is immediately sent off the chip. This reduces significantly the dead time of the pixels hit while the other pixels stay active and allows to reach very high readout rates of up to  $40 \text{ Mhits}/(\text{s} \cdot \text{cm}^2)$ .

The different settings of the chip are controlled using programmable DACs such as the  $I_{\text{kum}}$ , threshold, polarity of the sensor and the clock speed.

#### 4.1.1 SPIDR readout system for Timepix3

The SPIDR (Speedy PIxel Detector Readout) readout system [42] is used for the Timepix3 data acquisition. This system is able to handle high rates of data sent by the Timepix3 ASIC at full speed. This is achieved with Xilinx Virtex-7 FPGA [43] and a 10 Gb Ethernet link.

Figure 4.3 shows the Timepix3 chip and the SPIDR readout board. Voltage regulators on the Timepix3 chip board allow to set the voltage of the programmable DACs.

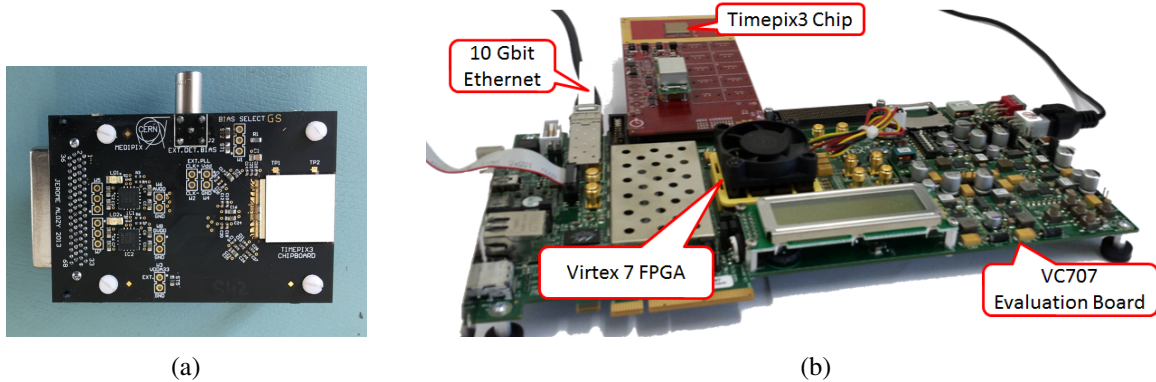


Figure 4.3: (a) Timepix3 chip board and (b) SPIDR readout board (from [3]).

## 4.2 Timepix3 assemblies

A summary of the Timepix3 assemblies used in this study is shown in Table 4.2. Advacam sensors [44] of thickness 50-150  $\mu\text{m}$  are bump-bonded to Timepix3 readout chips.

Table 4.2: Details of different Advacam planar pixel sensors bump-bonded to Timepix3 readout ASICs and studied in calibration and test beams.

Timepix3 ID	Thickness [ $\mu\text{m}$ ]	Type	Bias voltage [V]	Threshold DAC
W19_G7	50	n-in-p	-15	1190
W19_F7	50	n-in-p	-15	1187
W19_L8	50	n-in-p	-15	1133
W19_C7	50	n-in-p	-15	1148
W5_E2	100	n-in-p	-20	1160
W5_F1	150	n-in-p	-30	1153

## 4.3 Electronic noise

Electronic noise places a limit on the minimum detectable signal level. It defines the ability to distinguish signal levels and their precision of measurement. The signal in the detector is overlaid with the front-end electronic noise, during the amplification and pulse shaping. Thermal excitations and sensor leakage currents are important sources for the noise. We do not make a separation between the different sources of noise in this work. The electronic noise can be measured as explained further in Section 4.6.1. For Timepix3 readout chips, the electronic noise before bonding to any sensor is less than 70 e<sup>-</sup> RMS and after bonding it increases to  $\sim 80$  e<sup>-</sup> RMS due to the capacitance of the sensor and its leakage current.

## 4.4 Threshold dispersion and equalisation

In semiconductor electronics, manufacturing imperfections cause variations in the performance of the devices within the same chip. In this regard, the programmable global threshold of the chip is one of the most affected parameters.

A global threshold voltage generated by a programmable DAC (Digital-to-Analogue Converter) in the periphery of the chip is applied to all the pixel discriminators. But the effective threshold of each discriminator varies from one pixel to another. To overcome this dispersion, a 4-bit local threshold adjustment is applied to each pixel in order to achieve a uniform global threshold. The equalisation consists of adjusting this local threshold. Figure 4.4 shows the spread of the threshold before and after equalisation for the assembly W19\_L8.

The chip is operated in a photon counting mode in the procedure. First, the local threshold is set to its minimum value (mask 0000). For each pixel, the global threshold DAC (THL) is scanned from a level of no counts (threshold above the chip noise) to a level where all the pixels count (threshold close to the noise level). This results in an S-shaped curve. The middle of this curve, where the curvature changes, corresponds to the mean value of the noise. The same measurement is then repeated by setting the adjustment bits to their maximum value (mask 1111) and THL is scanned again.

For each pixel, the operation range is thus known. Assuming a linear relationship between the two points, the adjustment threshold is set in such a way that the global threshold will remain uniform across the matrix. After equalisation, the response of the chip becomes more uniform even though some dispersion remains ( $\sim 40$  electrons).

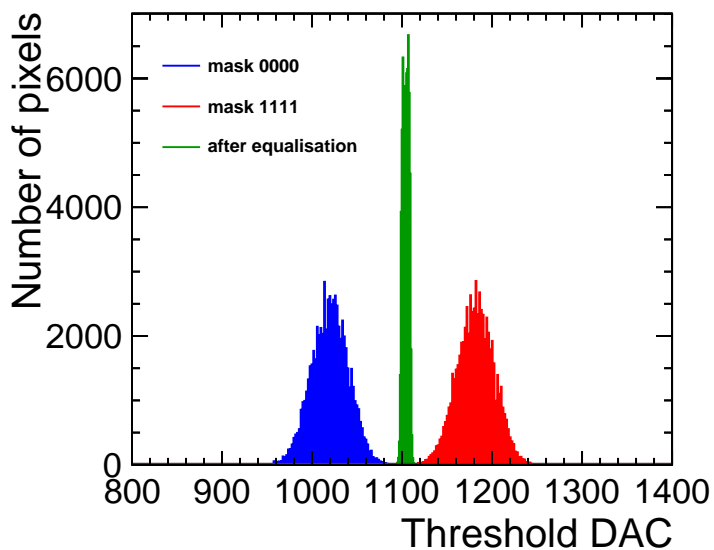


Figure 4.4: Spread of pixel responses for the assembly W19\_L8 during equalisation for the local threshold set at its minimum value (mask 0000), to its maximum value (mask 1111) and after equalisation.

## 4.5 Operating threshold

The electronic noise and the threshold dispersion are important parameters to determine the operating threshold of the readout ASIC. The operating threshold for the Timepix3 chip is set to 6 times the electronic noise RMS added in quadrature to the threshold dispersion. This threshold level significantly reduces the detection of noisy hits. The very low noise of the Timepix3 chip allows for operating the chip at a low threshold of approximately 500 electrons and thereby the detection of small signals. Sometimes, at this threshold a few pixels show a high rate of hits in absence of incident radiation (hot pixels) and they are manually masked to be able to operate the chip at the lowest possible threshold. Table 4.3 shows the number of masked pixels for the tested assemblies. They were masked either after the equalisation due to their baseline which was very different than other pixels or manually since they were noisy at the nominal operating threshold. In total, the number of masked pixels is less than 1% of the matrix.

Table 4.3: The number of masked pixels after the equalisation and the manual adjustment of the threshold.

Assembly	Number of masked pixels
W19_G7	46
W19_F7	35
W19_L8	14
W19_C7	33
W5_E2	41
W5_F1	42

The operating threshold affects significantly the spatial resolution of the device. A lower threshold allows for detecting most of the signal deposited by a charged particle. For this reason, it is important to minimise the electronic noise and the threshold dispersion.

## 4.6 Calibration

The aim of the calibration is to parametrise the measurements done by the readout chip, namely the relationship between the threshold DAC and the TOT with the energy deposited in the sensor. The unit to describe the energy deposited in the sensor can be in keV or the number of electron-hole pairs produced knowing that the average energy required to produce an electron-hole pair is  $\sim 3.6$  eV (see Section 3.1.1).

In this work we focus on the threshold DAC and the TOT calibration and the unit to describe the energy deposition is chosen to be the number of electron-hole pairs generated (or to simplify in number of electrons).

The threshold DAC and TOT calibration can be achieved using two methods. The first one consists of the use of photons with a well defined energy. These photons can either come from radioactive sources with a characteristic decay energy or from X-ray fluorescence (XRF) with a characteristic emission energy [45]. The photon being stopped in the sensor, it deposits its full energy. Since the energy of the photon is known, its relation to the threshold DAC or TOT can be characterised.

The second method consists of the use of an internal analogue test pulse generator. The Timepix3 readout ASICs provide an internal test pulse generator which can be used for calibration. In each pixel, a capacitor allows for injecting a charge by applying a voltage step over it. The injected charge is given by:

$$Q = C \cdot \Delta V , \quad (4.1)$$

where  $Q$  is the injected charge,  $C$  the injection capacitance and  $\Delta V$  the voltage difference applied. The injection capacitance can vary from pixel to pixel and also from chip to chip. From chip design simulations, the metal-to-metal capacitance can be extracted. For the Timepix3 readout chip a capacitance of  $20.2 \text{ e}^-/\text{mV}$  (or about  $3.2 \text{ fF}$ ) is expected. This value has also been cross-checked with X-ray sources and the expected value has been validated [46].

For calibration with the chip bump-bonded to a sensor, the sensor is biased to full depletion to reduce the capacitive noise. In this thesis, the calibrations are performed using the test pulse generator as it provides good results and the calibration is later validated using the test-beam data (see Section 7.2.1).

#### 4.6.1 Threshold-energy calibration

Section 4.5 describes the selection of the operating threshold DAC setting for a Timepix3 readout chip. This threshold can be translated into an effective energy. The counting mode is used for this measurement.

For Timepix3 assemblies, the threshold is calibrated using test pulses at four different heights corresponding to 0, 1000, 3000 and 6000 electrons. For each pulse height, 200 pulses are sent to the pixels in the diagonal of the matrix. For each pixel, the threshold DAC is scanned with a step size of 2 from a level of no counts (threshold above the signal) to a level where the pixel counts all the pulses (or close to the noise level when no pulse is sent) resulting in an S-shaped curve as shown in Figure 4.5(a). The readout electronics noise smears the ideal sharp turn on and generates the S-curve. At the maximum gradient of the S-curve, the threshold DAC corresponds to the pulse amplitude. The S-curve is fitted with a sigmoid function defined as:

$$f(x) = \frac{1}{1 + e^{-x}} . \quad (4.2)$$

The derivative of the S-curve or the sigmoid function is a bell-shaped curve as shown in Figure 4.5(b) with a mean at the maximum gradient of the S-curve.

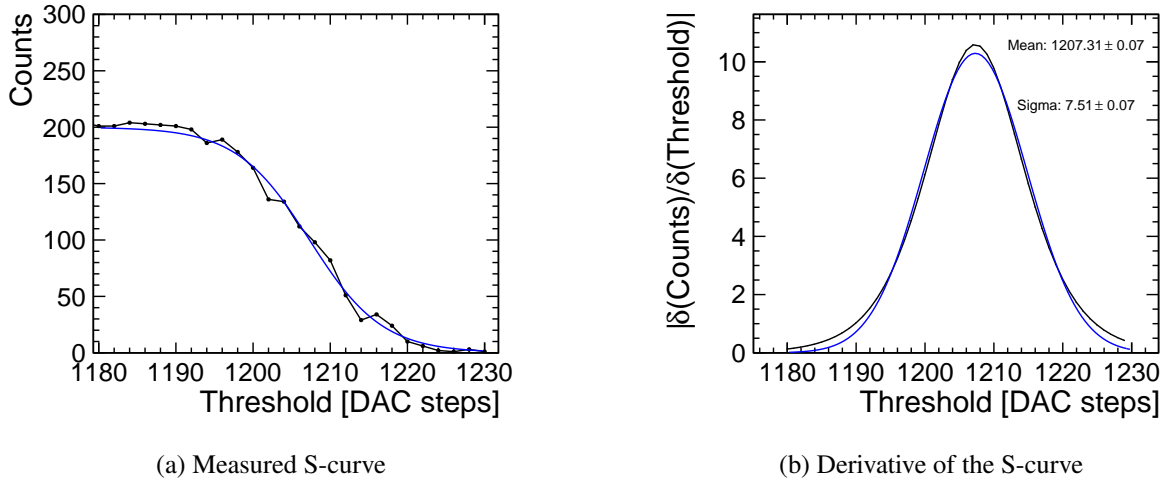


Figure 4.5: (a) An example of a measured S-curve fitted with a sigmoid function and (b) the sigmoid's derivative fitted with a Gaussian function for the assembly W5\_E2 using a pulse height of 1000 electrons for the pixel (0, 0) (see the coordinates system in Figure 5.3). This measurement is performed for all the pixels on the diagonal of the matrix for each assembly.

A linear fit is used to parametrise the relationship between the pulse height and the threshold DAC

value given by the mean of the derivative of the S-curves for the pixels in the diagonal of the chip:

$$THL_{DAC} = p \ THL_{e^-} + q , \quad (4.3)$$

where  $THL_{DAC}$  is the threshold DAC setting and  $THL_{e^-}$  the corresponding energy (in number of electrons).

Figure 4.6 shows an example of the threshold calibration obtained for the assembly W5\_E2 (see Appendix A for all the assemblies). Each point used for the fit corresponds to the mean of the Gaussian fitted to the derivative of the sigmoid function fitting the S-curve for all the diagonal pixels combined. The RMS of the mean is used as the error on the mean. The RMS represents the threshold dispersion from one pixel to another and corresponds to  $\sim 40$  electrons.

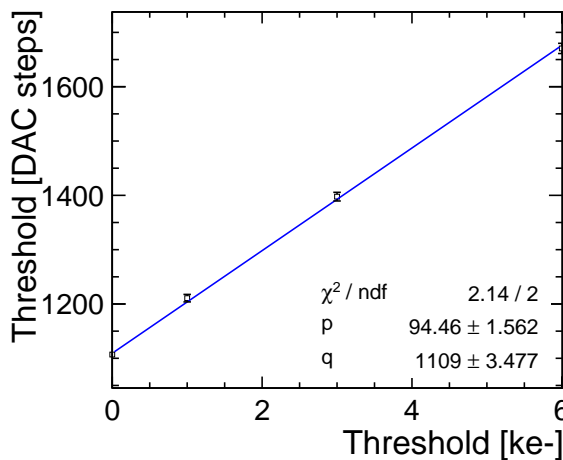


Figure 4.6: Threshold calibration for W5\_E2. Each point corresponds to the maximum gradient of the S-curve for each pulse height. A linear function as described in Equation (4.3) was used to fit the data points and obtain the parameters  $p$  and  $q$ .

The operating threshold DAC for each assembly was converted to an energy by solving Equation (4.3) for  $THL_{e^-}$  with  $THL_{DAC} = THL_{DAC}^{op}$ . The error on the evaluated threshold in energy ( $THL_{e^-}^{op}$ ) is obtained by the propagation of errors for the inverse of Equation (4.3):

$$\sigma_{THL_{e^-}(THL_{DAC})}^2 = \frac{(THL_{DAC} - q)^2}{p^4} \sigma_p^2 + \frac{1}{p^2} \sigma_q^2 + 2 \frac{THL_{DAC} - q}{p^3} \sigma_{pq}^2 , \quad (4.4)$$

where  $p, q$  are given by the linear fit using Equation (4.3) with standard deviations  $\sigma_p, \sigma_q$  and covariance  $\sigma_{pq}$ .

Table 4.4 summarises the fit parameters  $p$  and  $q$ , the operating threshold DAC and its conversion into energy deposition in number of electrons for all the assemblies listed in Table 4.4.

For further verification of these results, the Timepix3 DAC step gain for each assembly is calculated to be around  $\pm 11$  e $^-$ /step, in agreement with [3].

Without test-pulse injection, the mean of the derivative of the S-curve defines the baseline of the chip and its width the electronic noise. The standard deviation of the baseline for the pixels in the diagonal of the matrix corresponds to the threshold dispersion.

For all assemblies, the noise varies between 6 to 7 DAC values which corresponds to 70 to 80 electrons, in agreement with [3]. The error on the noise is obtained by the error propagation of Equation (4.3).

Table 4.4: Threshold fit parameters p and q, the operating threshold DAC setting and its conversion into energy deposition.

Assembly	p [DAC steps/ke <sup>-</sup> ]	q [DAC steps]	THL <sub>DAC</sub> <sup>op</sup> [DAC steps]	THL <sub>e<sup>-</sup></sub> <sup>op</sup> [e <sup>-</sup> ]
W19_G7	87.4 ± 1.4	1145.9 ± 2.9	1190	505 ± 31
W19_F7	92.0 ± 1.5	1134.9 ± 3.4	1187	566 ± 33
W19_L8	89.9 ± 1.5	1083.9 ± 3.1	1133	546 ± 31
W19_C7	90.4 ± 1.4	1096.4 ± 3.5	1148	571 ± 34
W5_E2	94.5 ± 1.6	1109.3 ± 3.5	1160	537 ± 33
W5_F1	89.0 ± 1.3	1105.3 ± 3.1	1153	536 ± 31

Table 4.5 summarises the baseline mean, the threshold DAC step, the electronic noise and its conversion into energy deposition for the assemblies listed in Table 4.4.

Table 4.5: Measured baseline mean, threshold DAC step gain, the electronic noise and its conversion into energy deposition.

Assembly	Baseline mean [DAC steps]	Threshold DAC step [e <sup>-</sup> ]	Noise [DAC steps]	Noise [e <sup>-</sup> ]
W19_G7	1143.9 ± 3.2	11.4 ± 0.2	6.9 ± 0.9	78.5 ± 10.3
W19_F7	1131.7 ± 3.8	10.9 ± 0.2	7.1 ± 0.9	76.7 ± 9.9
W19_L8	1082.0 ± 3.3	11.1 ± 0.2	7.0 ± 0.9	77.9 ± 10.2
W19_C7	1092.8 ± 3.9	11.1 ± 0.2	7.4 ± 1.1	82.0 ± 12.4
W5_E2	1106.9 ± 3.9	10.6 ± 0.2	7.2 ± 1.1	75.7 ± 11.8
W5_F1	1103.6 ± 3.4	11.2 ± 0.2	6.7 ± 0.9	75.4 ± 9.7

## 4.6.2 TOT-energy calibration

The TOT calibration parametrises the relationship between the energy deposited and the TOT measurement. Due to the non-linearity of the Timepix3 charge preamplifier, this relationship is modeled as a hyperbola. The function used to fit the data points is called a *surrogate function* and is obtained as:

$$\text{TOT} = aE + b - \frac{c}{E - t}, \quad (4.5)$$

where TOT denotes Time-over-threshold, E the deposited energy and a, b, c, t are the parameters to be found [47]. The inverse of the surrogate function is defined as:

$$E = \frac{t \cdot a - \text{TOT} - b + \sqrt{(b + t \cdot a - \text{TOT})^2 + 4 \cdot a \cdot c}}{2a}. \quad (4.6)$$

In Equation (4.5), for higher values of the energy, the relationship between TOT and E is linear with gradient a and intercept b since the term aE + b dominates. At low energy, the term c/(E - t) becomes important. The parameter c defines the amount of curvature in the function. An asymptote occurs at E = t. The point at which the fit crosses the x-axis (TOT=0) corresponds to the threshold: below the threshold no charge can be detected. The calibrated threshold is used as a data point for the surrogate fit at the crossing-point on the x-axis. The range for the TOT and the boundary between low energy (non-linear response) and high energy (linear response) depend on the clock frequency, the threshold and

the  $I_{\text{krum}}$  value.

For the calibration of the assemblies, the Timepix3 ASICs are operated in TOT mode and the test-pulse injection is used (Equation (4.1)). Test pulses with heights ranging from 0 mV to 800 mV (corresponding to 0 electrons to 16000 electrons) are sent to each pixel. For each pulse height, 100 test-pulses are sent. The sum of the TOTs and also the sum of the square of the TOTs for each pulse height is recorded. The mean of the TOT response and the standard deviations are then calculated. Finally, the data are fitted with the surrogate function as given in Equation (4.5) for each pixel, to determine the pixel-by-pixel energy calibration of the assembly.

Table 4.6 summarises the DAC settings used for the operation of the Timepix3 assemblies in test beams. The same settings are as well used for the calibration. Figure 4.7 shows the pixel-by-pixel calibration for assembly W5\_E2 operated at two different threshold DACs of 1160 (537 electrons) and 1190 (855 electrons). For a higher threshold, the curves are shifted towards higher energy values on the x-axis but the slope (parameter  $a$ ) remains the same.

Table 4.6: DAC settings for the operation and calibration of the Timepix3 assemblies. VFBK is a programmable DAC to determine the baseline voltage of the chip.

$I_{\text{krum}}$	TOT/TOA Clock	FTOA Clock	VFBK
10	40 MHz	640 MHz	150

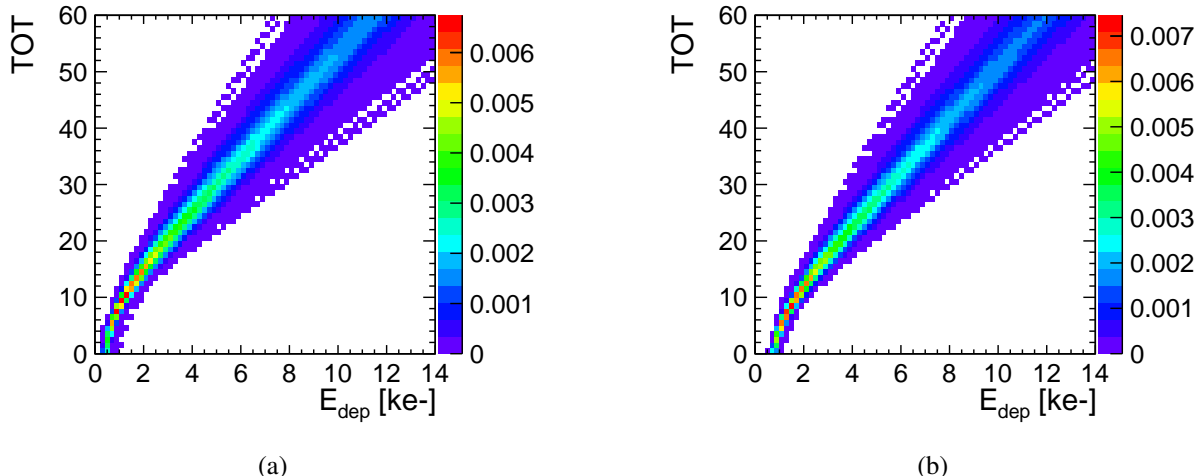


Figure 4.7: Pixel-by-pixel calibration of the TOT for assembly W5\_E2 operated at the threshold DACs of (a) THL=1160 (537 electrons) and (b) THL=1190 (878 electrons).

## 4.7 Summary

This chapter gives an overview on the Timepix3 readout ASIC which is used in the tracking planes of the CLICdp Timepix3 telescope (Chapter 6) and also employed as a test vehicle for the characterisation of thin sensors (Chapter 7) and active-edge sensors (Chapter 8). The test-pulse injection method is used to calibrate the operating threshold and the TOT value into energy depositions. In Chapter 7, the calibration is applied to the test-beam data and validated with simulations.

# CHAPTER 5

---

## Simulation and reconstruction software frameworks

---

Simulation tools have a crucial role in the development and also understanding of the performance of semiconductor devices. The simulations are validated with the data and used to predict the performance of small-pitch pixels for which data is not yet available.

This chapter describes the simulation tools used to understand the performance of Timepix3 devices. The reconstruction software, used for both data and simulation, is also presented.

### 5.1 GEANT4

GEANT4 [4], as an object-oriented simulation toolkit implemented in the C++ programming language, is widely used in high energy, nuclear and accelerator physics, medical and space sciences. As modern particle physics is going towards large-scale detectors, more accurate simulations are needed in order to understand the complex situations. GEANT4 provides software components which can be used to study basic phenomena, geometries and full-scale detector simulations for experiments. GEANT4 simulations take into account parameters such as: the geometry of the system, the materials involved, the generation of primary particles, the tracking of particles through materials and external electromagnetic fields, the physics processes involved in the possible interaction of the particles with the materials they are passing through and the response of sensitive components. The simulations of the interaction between the particles and materials are mostly validated with data. In this thesis, GEANT4 version 10.1.2 is employed for the simulations.

GEANT4 provides physics models for different type of interactions called *physics lists*. The *emstandard* physics lists provide the electromagnetic interactions of photons and charged particles with matter and is suited for the simulation of ionisation, bremsstrahlung, gamma conversion and other electromagnetic interactions of particles with energies from 1 keV up to 10 PeV [48]. This physics list is commonly used for the simulation of the energy loss in pixel detectors.

GEANT4 provides as well the Photo-Absorption Ionisation (PAI) model [49] for the precise simulation of ionisation energy loss by relativistic charged particles in very thin absorbers. Since in very thin sensors the Landau model is not suitable (see Section 3.2.3), the PAI model is based on the photo-absorption cross-section tables obtained by experimental data. In practice several classes are used to calculate the integral ionisation cross-section, the mean number of ionising collisions as well as the mean ionisation energy loss for the selected material and the given Lorentz factor.

Figure 5.1 compares the energy loss due to ionisation in 50  $\mu\text{m}$  and 450  $\mu\text{m}$  thick silicon sensors for

different GEANT4 physics lists and the Bichsel parametrisation (see Section 3.2.4). For the 50  $\mu\text{m}$  thick sensor, the *emstandard\_opt3* physics list gives a reasonable value for the most probable value ( $\Delta_p$ ) but the width ( $w$ ) of the distribution is more narrow than the Bichsel distribution. The PAI model shows a very good agreement with the Bichsel model. For the thick sensor of 450  $\mu\text{m}$ , both PAI and *emstandard\_opt3* physics lists show similar distributions as the Bichsel model.

The energy deposition given by the PAI model is very close to the one calculated by Bichsel especially for the fluctuations around the most probable value and for very thin sensors. For this reason, the PAI model is chosen to be used later for the simulations even though it requires more computation power.

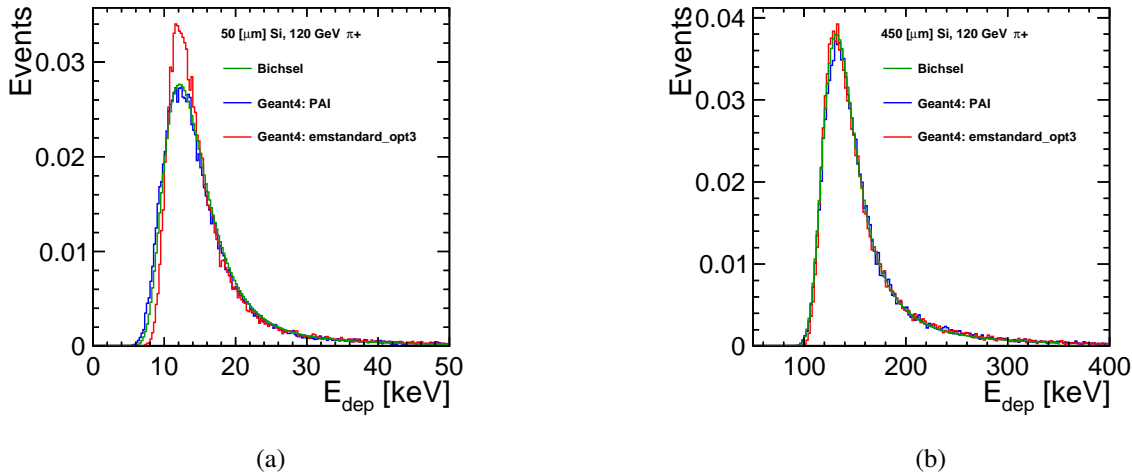


Figure 5.1: Energy-loss distribution in (a) 50  $\mu\text{m}$  and (b) 450  $\mu\text{m}$  thick silicon sensors due to the passing of 120 GeV  $\pi^+$  comparing the Bichsel model and GEANT4 using the PAI and the *emstandard\_opt3* physics lists.

## 5.2 AllPix simulation framework

AllPix [50–52] is a GEANT4-based simulation software framework. It is written in C/C++ and provides a flexible interface to define a pixel detector geometry to simulate pixelated sensors and readout chips. It is widely used for the simulation of pixel detectors in different high energy physics experiments. It allows for defining an experimental setup with its surrounding environment as realistic as possible, such as the components of a test beam setup. It also allows for the simulation of more complex geometries such as a full vertex detector.

GEANT4 provides the simulation of particles through matter: it calculates the position of the hits (the true Monte Carlo position) considering multiple scattering and the energy deposition in the sensitive volumes (sensors). The software user defines the semiconductor physics and readout chip properties in a digitiser as described below.

AllPix is used for the simulations described in Chapter 6 and Chapter 7. Figure 5.2 shows an example of the simulation for the Timepix3 telescope (described in Chapter 6) in AllPix with the device under test (DUT) in the middle of the tilted telescope planes.

### 5.2.1 Coordinate system

The convention used for the pixel detectors (in AllPix and also in the reconstruction software as described in Section 5.4) for a Timepix3-like matrix of 256  $\times$  256 pixels is shown in Figure 5.3. The pixel

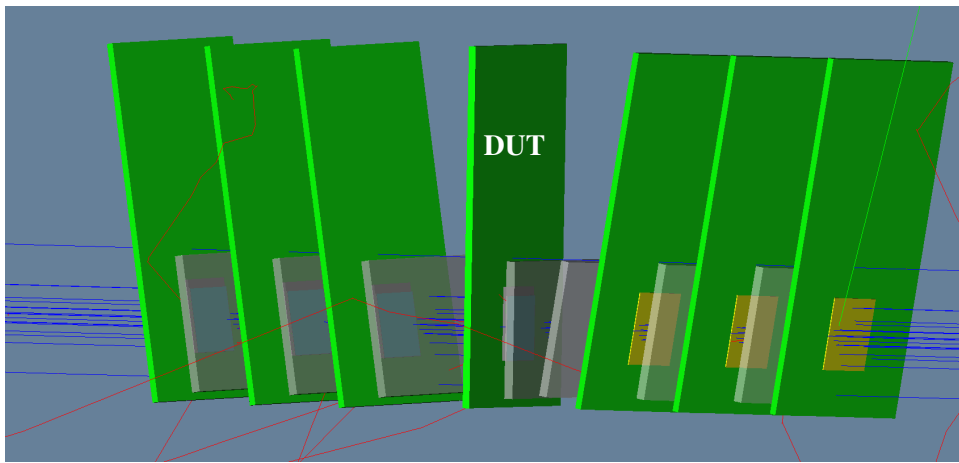


Figure 5.2: Simulation of the Timepix3 telescope in AllPix with the six tilted telescope planes and the device under test (DUT) in the center as well as particle tracks from the beam entering the telescope from the right.

coordinates (column, row) are shown in black and the local coordinates ( $x$ ,  $y$ ) in millimeters of the center of the pixels in the corners of the matrix are shown in blue. In this convention we are looking from the sensor side with the chip periphery at the bottom.

### 5.2.2 Geometry of the pixel detector

In AllPix, the pixel detector geometry can be defined by the pitch size, the thickness of the sensor and the readout chip for a hybrid configuration, the PCB properties, the mechanical support and other geometry properties related to an assembly. These parameters are usually defined in an XML file. Each detector is identified by a unique ID number. This facilitates the running of the simulation with different parameters by only changing the XML file without the need of re-compiling the code. It is also possible to define the parameters of the digitiser in this XML file.

### 5.2.3 Geometry of the simulation scenario

The simulation scenario is defined in a macro file. The position of the detectors in space is specified by the coordinates ( $x$ ,  $y$ ,  $z$ ) and the rotations around the  $x$ ,  $y$  and  $z$  axes through the centre of the detectors. The physics list used by GEANT4 is specified. The General Particle Source (GPS), which is the GEANT4 toolkit for the generation of high-energy particles, is also described in the macro file. The particle type, the beam energy, position and distributions are customisable. The simulation is done based on frames. The frame can be related to the integration time of the detectors during which the shutter is open and all the particles are detected in this specific lapse of time. For a Timepix3-like detector which is operated based on a data-driven readout (see Section 4.1), the frame length is not fully defined. For the simulation of such a readout, the beam profile is defined in such a way that pile-ups are avoided and a pixel is hit by particles only once during one simulation frame. During test beams, the particle rate is also adjusted to avoid pile-ups. Since we are mostly interested in the physics of the detector and not testing the timing capabilities of the readout system, this definition of a frame is reasonable.

Visualisation parameters are also given in the macro. Open Inventor [53] can be, for example, used to visualise the simulation scenario and also the particle tracks in the detectors.

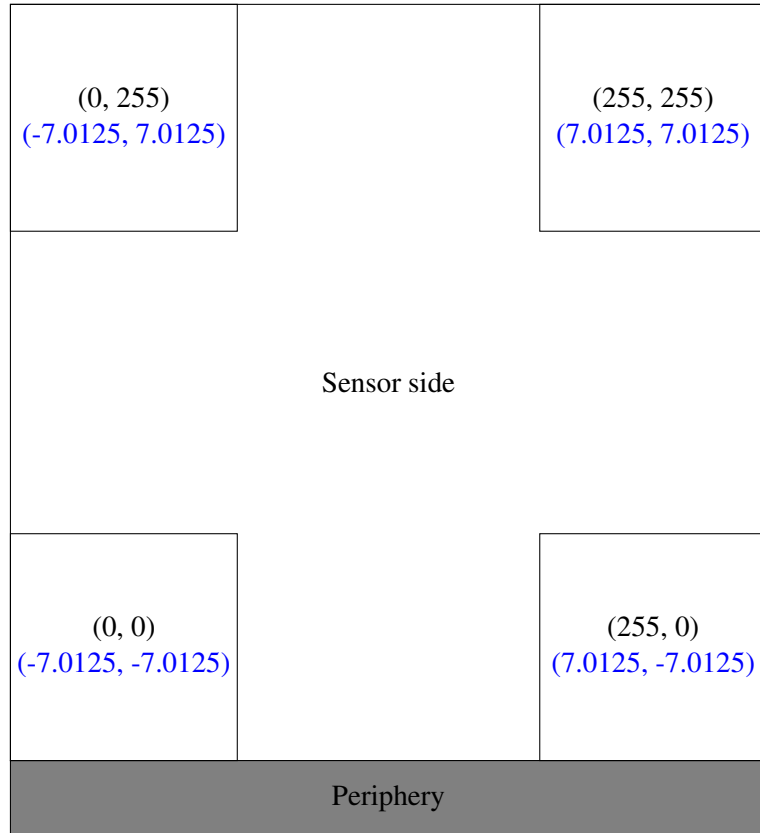


Figure 5.3: The coordinates system for a matrix of  $256 \times 256$  pixels. The pixel coordinates (column, row) are shown in black and the local coordinates ( $x, y$ ) in millimeters of the center of the pixels in the corners of the matrix are shown in blue. In this convention, we are looking from the sensor side with the periphery at the bottom.

### 5.2.4 Digitisation

The digitisation step in AllPix is responsible for the full simulation of the detector including the sensor and the readout chip. Each user defines the simulation parameters in the digitiser. This provides flexibility for the simulation of different sensor technologies and readout chip families. In this section, we describe the digitiser used for the simulation of thin sensors.

For each simulation step (G4Step) through the matter, GEANT4 provides the energy deposited in the sensitive material. The step length can be customised and for thin sensors simulations, a step of  $2 \mu\text{m}$  provides a good precision for the calculations of the energy deposition.

The semiconductor physics in a silicon detector is defined by the user in the digitiser. The drift and diffusion are performed at each step to simulate the electron-hole pair movement in the electric field. The simplified model as described in Section 3.3.2 is used for the simulation of silicon physics. In practice at each G4Step, where the energy deposition is given by GEANT4, the amount of the charges drifting towards the readout electrode is known. These charges diffuse due to the random thermal motion in the crystal lattice and do not exactly follow the electric field lines. The spread of the arrival position of a charge generated at a given Step<sub>z</sub> is described as a Gaussian distribution with standard deviation as given in Equation (3.37). Figure 5.4 schematically illustrates the digitisation in a sensor in one direction. Each GEANT4 step is shown as a circle. In 2D, at each step, the charge collected in the hit pixel and its neighbouring pixels is calculated by:

$$Q(z) = q_i(z) \cdot \frac{1}{\sqrt{2\pi}\sigma(z)} \int_{x_1}^{x_2} e^{-\frac{(x-x_{hit})^2}{2\sigma(z)^2}} dx \cdot \frac{1}{\sqrt{2\pi}\sigma(z)} \int_{y_1}^{y_2} e^{-\frac{(y-y_{hit})^2}{2\sigma(z)^2}} dy \quad (5.1)$$

where  $q_i(z)$  is the energy deposited at step  $i$  at the depth  $z$ ,  $\sigma(z)$  the standard deviation of the diffusion for a charge generated at  $z$ ,  $x_{hit}$  and  $y_{hit}$  are the coordinates where the track hits a pixel,  $x_1$  and  $x_2$  the x-coordinates and  $y_1$  and  $y_2$  the y-coordinates of the pixel where the contribution of the charge is being calculated.

For each pixel, at each step a charge deposition is calculated. All contributions due to all the steps sum up and the total charge deposited in a pixel is finally calculated.

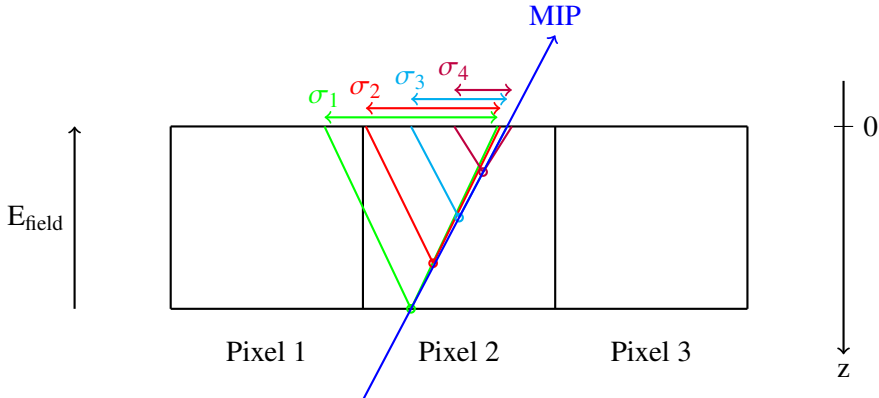


Figure 5.4: Illustration of the digitisation in a sensor. Each GEANT4 step (G4Step) is shown with a circle. The spread of the arrival position of a charge generated at the steps 1, 2, 3 and 4 is described as a Gaussian distribution with standard deviations  $\sigma_1, \sigma_2, \sigma_3$  and  $\sigma_4$ . The contribution of the diffusion in the hit and its neighbouring pixels is calculated using Equation (5.1).

In this digitiser, the effect of the weighting field as described in Section 3.4.1 is neglected. As it has been studied, the weighting field is the strongest close to the pixel. Also, the drift velocity is the highest close to the pixel. For a charge  $q_i$  drifting towards a pixel, the induced current on the pixel can be approximated by a very short pulse, which integrates to charge  $q_i$ , and it is produced when the charge actually reaches the pixel (after its drift). For a neighbouring pixel, where  $q_i$  does not terminate on its measurement electrode, a signal current is induced but the current changes sign and integrates to zero. This approximation is validated with data later in Chapter 7. However, in the presence of radiation damage in the sensor, this approximation is not valid anymore. This case is not studied for CLIC.

The digitiser also defines the parameters of the readout chip. The electronic noise (with a Gaussian distribution as described in Section 4.3) is added. The readout threshold is applied to eliminate the pixels where the charge deposition is less than the threshold. The hit energy is converted to the digital value TOT (time-over-threshold) using the readout calibrations (see Section 4.6.2).

## 5.3 TCAD simulations

Technology Computer-Aided Design (TCAD) as a simulation tool is used to optimise and develop semiconductor processing technologies as well as the device operation [35]. TCAD uses a finite element method to numerically solve the physical partial differential equations in semiconductors, such as the continuity and diffusion equations. This allows for the modeling of the structural properties and the electrical behaviour of semiconductor devices.

The TCAD simulations are performed in different steps. First, the sensor geometry is defined in a 2D or a 3D configuration. The doping profiles for the specific regions of the simulation are defined. In this step, the wafer processing is imitated as it is done in a foundry. The silicon bulk is doped to obtain the desired resistivity. The pixel implants are deposited to form pn-junctions. The aluminum contacts are placed to apply the high voltage on the backside of the sensor and the ground on the pixels. The simulation mesh is then described. The mesh divides the surfaces and volumes into small triangles. The simulation is solved numerically on this grid by respecting the boundary conditions and continuity equations between the mesh points. The number of the mesh points defines the accuracy and therefore the computation time for solving the equations. An optimised definition of the mesh is crucial for obtaining the solutions. Too coarse meshes may result in a poor accuracy of the solutions or even the calculations might not converge. For this reason, fine mesh points are described in regions with high gradients in the doping profiles and close to the pixel implants. Coarser mesh points are defined for the bulk of the sensor where the doping concentration is almost constant.

The stationary solution at a certain bias voltage is obtained after defining the geometry, the doping profiles and the mesh points. The voltage on the backside contact is ramped up in small steps. The electric field within the sensor is calculated and the depletion volume is delimited.

Finally, a transient simulation can also be performed after a particle hit in the sensor. Charge carriers are generated in the sensor by the passing of ionising particles. The charge carriers are propagated for a given time period. During their drifts towards the readout electrodes, an induced current is also generated in the contacts. The charge signal in the readout electrodes is integrated over the integration time and the signal to get the signal the readout chip would obtain.

For this study Synopsys TCAD version I-2013.12 is used to simulate the movement of charge carriers in silicon and the coupling to the readout. Also, it is used to simulate active-edge devices and results are compared with measurements in Chapter 8.

## 5.4 Reconstruction and analysis software frameworks

The offline reconstruction of the test beam data is done using two software frameworks. The EUTelescope software package [54, 55] is used to reconstruct the tracks from the telescope and extrapolate their positions on the DUT. For the analysis of the DUT data, the python-based software pyEudetAnalysis is used [56].

### 5.4.1 EUTelescope

The EUTelescope software is based on the ILCSof framework [57]. The latter provides the basic building blocks such as the LCIO (Linear Collider Input Output) data model, the geometry description toolkit GEAR and a modular application framework for event analysis, called Marlin [58].

A modular event-based analysis and reconstruction chain can be defined using Marlin processors. Each processor implements algorithms for specific tasks. The input parameters for the algorithms can be configured and loaded at runtime using *steering files* in XML format. For each event, the processors are called centrally by Marlin.

The EUTelescope framework, originally developed for the EUDET/AIDA pixel beam telescope [59], provides Marlin processors for the track reconstruction and data analysis of test beam experiments. Figure 5.5 schematically shows the analysis workflow in the EUTelescope framework starting from the raw data recorded during the test beam to particle tracks reconstruction. Since each experiment has its own data format for the DUT and also the telescope planes, the format converter is defined by the user.

This makes the framework flexible for testing different chip families with different data formats.

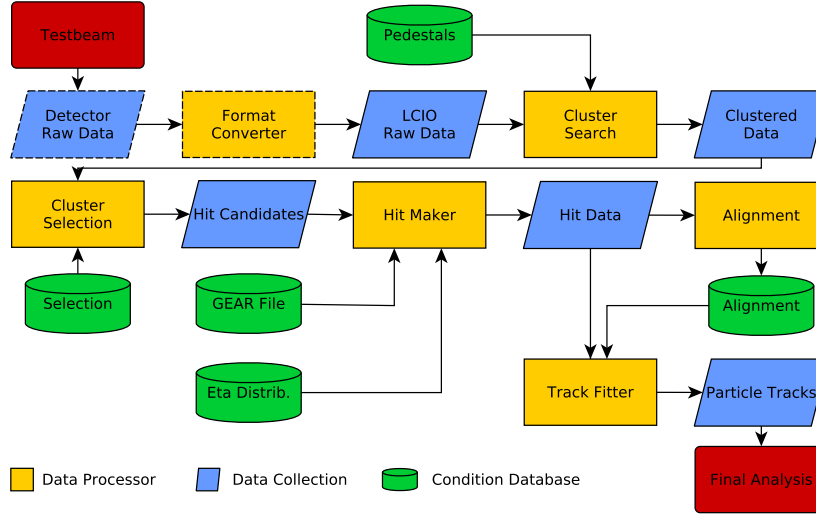


Figure 5.5: Data reconstruction and analysis workflow using the EUTelescope framework. From [60].

The EUTelescope framework was adapted for the reconstruction of the data from the Timepix3 telescope. The framework is originally written for a frame-based readout mode and had to be adapted to the data-driven readout mode which was used during the data taking. This affects mainly the definition of an event. In the frame-based mode, an event corresponds to a time frame where the shutter of the detectors are opened and all hits are integrated. When the shutter is closed, there is a dead-time where no data are acquired and all the hits are read out from the readout chips and recorded in a raw data file. In the data-driven mode, the data are acquired as soon as a pixel is hit (there is no shutter and almost no dead-time). The hits are written in the raw file with their time-stamps coming from a combination of the TOA and the FPGA timing from the SPIDR readout (see Section 4.1.1). They are not ordered in time in the raw file since the readout chip does not send them in the order they are produced. Pre-processing is needed to order the hits by their TOA and create events as described below.

The reconstruction chain for the Timepix3 telescope is performed in the following steps:

1. Converter: converts the raw files written by each telescope plane and the DUT in a binary format to an LCIO event. The converter also defines the event for the data-driven zero-suppressed readout mode and orders the hits.

In the converter processor, the hits within a time window of 3 ms are read and filled into a vector. This time window is large enough to acquire all the hits belonging to many tracks. The hits in the vector are ordered in time according to their time-stamps. An LCIO event is built by choosing the hits in the six telescope planes and the DUT with time stamps differing by at most 2.5  $\mu$ s. With this constraint, in most cases one track per event is obtained (for particle rates of  $\sim 1$  million per second) and all hits belong to the same track. Only around half of the 3 ms time window is used to reconstruct the events. The other half is combined with the next 3 ms time window in order to avoid the loss of the hits in-between the time windows.

2. Hot pixels remover: hot pixels with the maximum allowed frequency of 0.1 Hz are discarded from

the analysis.

3. Clustering: the clusters in each telescope plane are found.
4. Hit making: reconstruction of the hit position for each cluster with the  $\eta$ -correction method [36].
5. Alignment: the alignment processor uses the Millepede II algorithm [61] to align the telescope planes with respect to each other. It assumes straight tracks and consists of a least squares minimisation method. A proper definition of the geometry is important for this step.
6. Track finding: the EUTelTestFitter algorithm implemented as a Marlin processor is used for finding and fitting the tracks. This track fitting method is based on a  $\chi^2$ -minimisation as described in [62]. Due to the multiple scatterings in the telescope planes, the tracks are displaced in the order of a few micrometers, which can not be neglected since it is comparable with the expected resolution of the telescope layers. This method is separately considered for the horizontal (x) and vertical (y) planes. The goal is to determine the position of the tracks on each telescope plane and the DUT from the measured positions on the telescope planes. The  $\chi^2$  of the fit uses the additional constraint on the angles of the multiple scatterings (refer to [62] for the definition of the  $\chi^2$ ). The track positions correspond to the positions minimising the  $\chi^2$  distribution.

The track positions on the DUT can be written in a ROOT tree [63] and saved in a ROOT file. The raw data from the DUT is also written in the same file to be processed separately with the pyEudetAnalysis framework (see Section 5.4.2).

#### 5.4.2 pyEudetAnalysis

Once the telescope tracks are reconstructed using the EU Telescope framework, the analysis of the DUT can be done separately within the python-based pyEudetAnalysis framework [56]. Separating the telescope and the DUT analyses provides more flexibility on the analysis of the DUT. The tracks are reconstructed once and rerunning of the analysis on the DUT does not require to reconstruct the tracks once more.

The pyEudetAnalysis reads the reconstructed track position and the list of the pixels hit on the DUT from the ROOT file generated by EU Telescope.

The workflow for pyEudetAnalysis is very similar to EU Telescope, except for the track reconstruction step which is not needed in pyEudetAnalysis. The workflow is described in [38] and briefly summarised below:

1. Reading the output of the EU Telescope: the tracks and the pixels hit on the DUT are read from the ROOT file and stored in specified structures to be used for the analysis.
2. Hot pixel remover: noisy pixels on the DUT with a firing frequency higher than 0.01 Hz are removed from the analysis.
3. Clustering: the pixels hit on the DUT are clustered using the SciPy hierarchical `fclusterdata` algorithm [64].
4. Hit position reconstruction: pyEudetAnalysis provides several algorithms to reconstruct the position of the hits within the cluster. The  $\eta$ -correction method (see Section 3.4.3) is as well implemented which uses the TOT (charge) information to compensate for the non-linearities due to the charge sharing.

5. Track-hit alignment: the reconstructed tracks are compared to the reconstructed hit on the DUT. The hits are brought into lines with the tracks by defining translations in x and y directions during the pre-alignment procedure. The main alignment method consists of defining translations and rotations to precisely match the tracks to the matched hits. A metric is defined as the radial distance between each track and the closest hit within a distance of less than 0.5mm. The Nelder-Mead method of SciPy `optimize.minimize` [65] is used to minimise the total distance. This function automatically varies the rotation about z and the x and y translations simultaneously to find the optimal alignment.
6. Track-hit matching: the alignment constants found previously are applied to the hits. The hits on the DUT are then matched to the tracks. This is done by taking the closest hit to each track, within a radial distance of 0.1 mm. The hits which are not connected to the tracks most probably belong to the electronics noise and are not related to the passing of particles and therefore discarded in the analysis. The DUT efficiency can be studied by using this track-hit matching.



# CHAPTER 6

---

## The Timepix3 beam telescope

---

Testing in a high energy beam is a crucial step in the R&D for the pixel detector sensors and readout chips. Test beam data are used at various stages of the development for evaluating the performance of a prototype in addition to simulation tools like TCAD and GEANT4.

A telescope is used to reconstruct the tracks of the particles going through its planes. The track position is then extrapolated on the Device Under Test (DUT). This allows to compare the position of the hit on the DUT with the reconstructed track and extract the position and time resolutions as well as the efficiency of the device.

For the CLIC vertex detector R&D, the CLICdp Timepix3 telescope is used as a beam reference. This chapter gives an overview of the components of the Timepix3 telescope and its tracking performance. The telescope is implemented in AllPix simulations (c.f. Section 5.2) and its performance is compared to the data taken at the CERN SPS [66]. Finally, the tracking resolution on the DUT is extracted in simulations using the Monte Carlo information.

### 6.1 Experimental setup at the CERN SPS

The telescope is placed at the H6 beam [67] of the CERN SPS typically operated with a 120 GeV pion beam. The assemblies listed in Table 4.2 are tested as DUTs using this telescope. The beam is configured in such a way to have around  $1 - 5 \times 10^6$  particles per five-second spill. The telescope planes are positioned in a way to give the best tracking resolution for the given beam energy taking into account multiple scatterings and mechanical constraints. The optimisation is performed based on a global  $\chi^2$ -minimisation [62, 68]. The resulting optimal configuration implies a narrow spacing of all detector planes.

### 6.2 Components of the telescope

#### 6.2.1 Coordinates system

A Cartesian right-handed coordinate system is chosen to describe the geometry of the telescope. The z-direction is along the beam as shown in Figure 6.1 and the y-direction points vertically in the up direction.

### 6.2.2 Sensors and mechanics

The telescope consists of six planes of Timepix3 ASICs [3] bump bonded to 300  $\mu\text{m}$  thick p-in-n planar sensors (produced by Canberra) as shown in Figure 6.1. The sensors are depleted at a bias voltage of 30 V and nominally operated at 50 V. The Timepix3 readout chip threshold is set to  $\sim 1000$  electrons. The planes are tilted by 9° around the x and y axes [69]. Given the pixel pitch and the sensor thickness, this angle mainly leads to clusters of three pixels. Combining the TOT information, the reconstructed hit position provides sub-pixel resolution on the telescope planes. This leads to a tracking resolution of  $\sim 2 \mu\text{m}$  on the DUT.

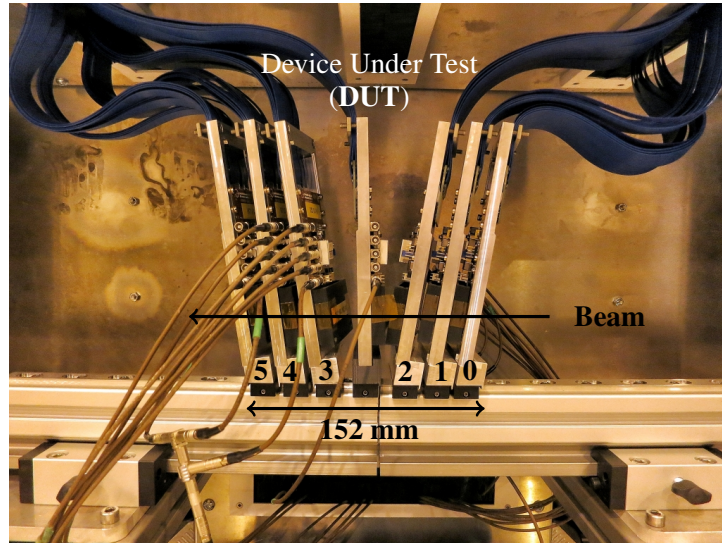


Figure 6.1: The Timepix3 beam reference telescope with six tilted planes for the tracking and the DUT in the middle inserted perpendicular to the beam direction. The telescope planes numbering convention is also shown.

The position of the telescope planes and the DUT along the beam axis using the convention as described in Figure 6.1 is given in Table 6.1. The positions correspond to the position of the center of the sensors.

Table 6.1: The position of the telescope planes and the DUT along the beam axis.

Plane number	Position [mm]
0	0
1	23.5
2	47
DUT	77
3	106.5
4	128
5	151.5

The mechanical supports for the telescope planes are optimised in order to reduce multiple scattering and therefore improve the tracking resolution. The Timepix3 assemblies are mounted on a PCB as shown in Figure 4.3(a). An aluminum support frame is used to hold the PCB. To protect the sensors from light exposure, an ABS plastic (acrylonitrile butadiene styrene) cover is used with a thickness of 2 mm and placed at a distance of 10 mm away from the PCB (in black in Figure 6.1). Table 6.2 describes the

material (with their thicknesses and radiation lengths) seen by the particles for each telescope plane. The PCB stacks up eight layers of copper interlacing with Isola IS410 type material with an average fill factor of 75% for copper. Behind the PCB, a layer of Copper is used for the cooling of the chip. The total material of a telescope plane is estimated to correspond to  $\sim 4\%$   $X_0$ .

Table 6.2: The material in each telescope plane contributing to the multiple scatterings of the traversing particles. X refers to the thickness and  $X_0$  to the radiation length.

Material	X [mm]	$X_0$ [mm]	X/ $X_0$ [%]
Cooling material for the chip (Cu)	0.1	14.4	0.69
Isola IS410 in the PCB	1.475	167.6	0.88
Copper in the PCB	0.125	14.4	0.87
ASIC (Si)	0.7	93.7	0.75
Sensor (Si)	0.3	93.7	0.32
Sensor cover (ABS plastic)	2	406.4	0.49
Total			4

### 6.2.3 Data acquisition system

The SPIDR readout system, as described in Section 4.1.1, is used for the data acquisition of the Timepix3 telescope planes. The Timepix3 readout ASICs are operated with the data-driven zero-suppressed readout mode. This system allows to record the data from all the particles from the SPS spill without dead time. The data is processed offline using the EUTelescope framework as described in Section 5.4.

## 6.3 The telescope performance

The telescope is simulated with the GEANT4-based AllPix simulation framework (c.f. Section 5.2). This allows for a better understanding of the telescope performance, extraction of the tracking resolution on the DUT and comparison to data. Since AllPix gives access to the Monte Carlo position (MC position) of the hits, the true tracking resolution can be obtained by comparing the MC position with the reconstructed track or hit positions.

### 6.3.1 Timepix3 telescope simulation in AllPix

In the simulations, the geometry of the telescope is defined in a realistic way by taking into account the positions and the rotations of the telescope planes, the thickness of the sensors and the pixel pitch. Figure 6.2 shows the geometry of the telescope as implemented in AllPix.

The mechanical supports for the telescope planes are implemented using the material as described in Table 6.2.

A digitiser for the Timepix3 readout chips bump-bonded to planar sensors is defined in AllPix. It simulates the silicon physics by calculating the drift and diffusion at each GEANT4 step as described in Section 5.2.4. The contribution of the generated charge by drift and diffusion in the hit pixel and its neighbouring pixels is calculated for each step. All contributions add-up and the charge in each pixel is calculated. The electronic noise of the Timepix3 ASIC defined by a Gaussian distribution of width  $\sim 80$  electrons sums up to the charge in each pixel. The readout threshold as obtained from the threshold calibration for the corresponding device is applied to each pixel and finally, the pixel-by-pixel

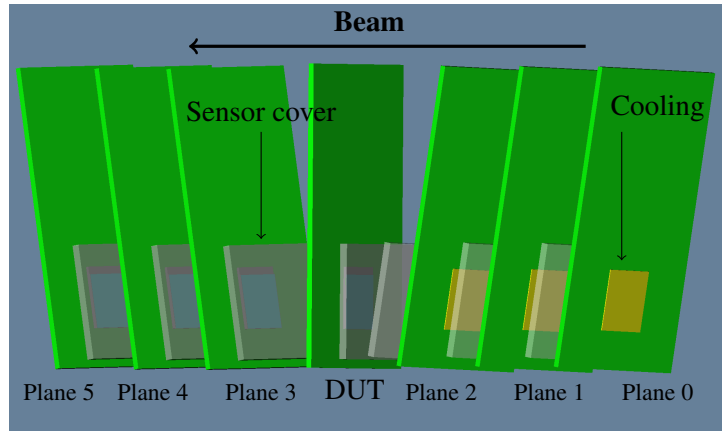


Figure 6.2: The Timepix3 beam reference telescope implemented in AllPix with six tilted planes for the tracking and the DUT in the middle inserted perpendicular to the beam direction. The telescope planes numbering convention is also shown in this figure.

TOT calibration (see Section 4.6.2) is applied to convert the energy deposition in TOT. The operation parameters as described in Section 6.2.2 are used for the AllPix simulations of the sensors of the telescope planes.

The GEANT4 General Particle Source (GPS) is used for the simulation of 120 GeV pions. The GPS generates a parallel beam with a transverse (radial) standard deviation of 5 mm.

The spread of the simulated track angles due to multiple scattering is shown in Figure 6.3. A scattering of 0.1 mrad causes a displacement of up to  $\sim 3 \mu\text{m}$  over a distance of 30 mm. The angles  $\phi$  (in horizontal direction) and  $\theta$  (in vertical direction) are given as:

$$\phi = \arctan \frac{x_2 - x_{DUT}}{z_2 - z_{DUT}}, \quad (6.1)$$

$$\theta = \arctan \frac{y_2 - y_{DUT}}{z_2 - z_{DUT}}, \quad (6.2)$$

where  $x, y$  and  $z$  are the MC positions of the hits on the plane 2 and the DUT.

The EUTelescope software framework (c.f. Section 5.4.1) is used to reconstruct the hits on the telescope planes using the  $\eta$ -correction method [36]. The tracks are fitted based on a  $\chi^2$ -minimisation method as described in Section 5.4.1.

### 6.3.2 Single-hit resolution on the telescope planes

The bias and the depletion voltages, the sensor type and the threshold values are the parameters defining the charge sharing and the cluster size distribution. Therefore they define the intrinsic resolution of the sensors.

Figure 6.4 compares the cluster size distribution and the charge of the clusters in data and simulations for the first telescope plane (plane 0). There is a good agreement between the cluster-size distributions in data and simulations. The small discrepancy might be due to the assumption on the un-calibrated threshold value used in data which affects largely the cluster-size distribution.

The hit resolution of a telescope plane is given by comparing the reconstructed hit position with the Monte Carlo position ( $x_{MC}$  and  $y_{MC}$ ) obtained by AllPix simulations. Figure 6.5 shows the hit residuals of the first telescope plane in  $x$  and  $y$  directions in simulations. The hit resolution is also considered

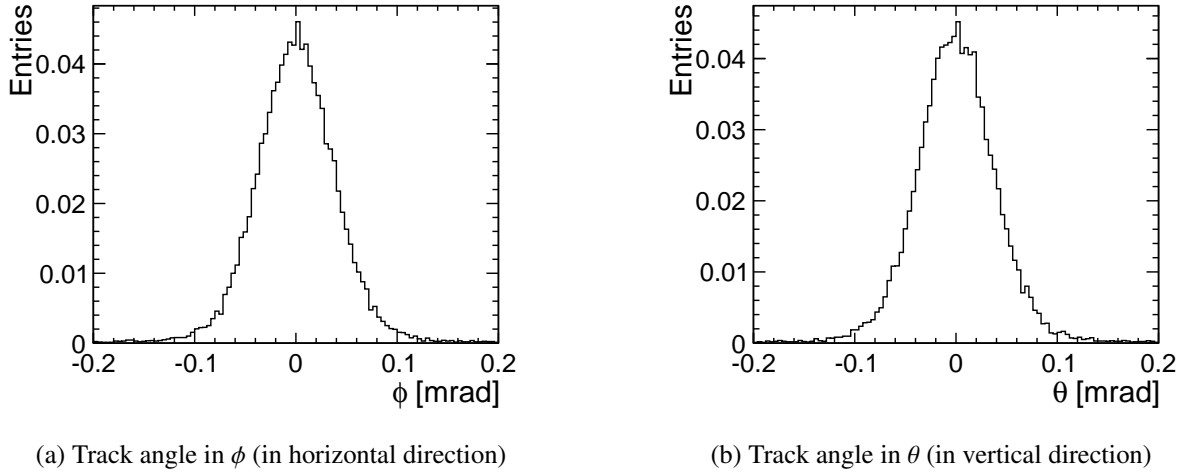


Figure 6.3: Track angular distribution in GEANT4 simulations due to multiple scatterings between the telescope plane 2 and the DUT obtained by comparing the global MC positions on both planes.

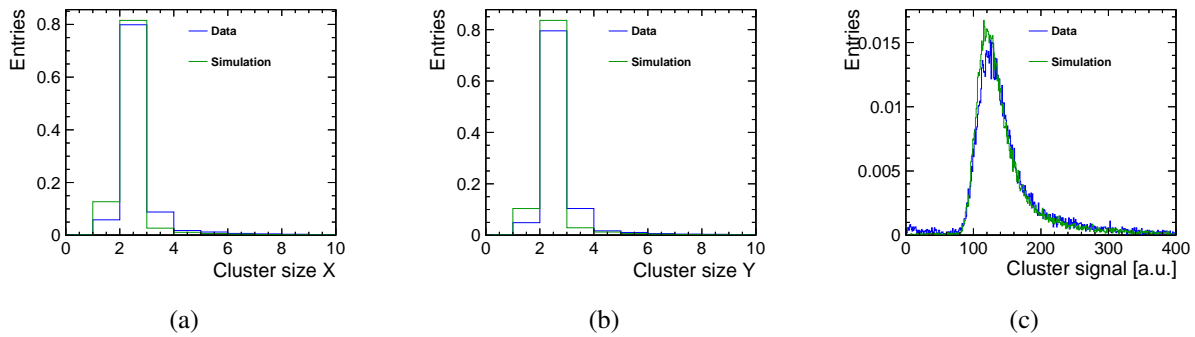


Figure 6.4: For the telescope plane 0, the cluster-size distribution in the (a) x direction and (b) y direction. (c) shows the sum of the charge in the cluster in units of TOT.

as the intrinsic resolution of the sensors. The standard deviation of a Gaussian fit to the center 95.5% of the residual distribution gives a resolution of  $\sim 2.7 \mu\text{m}$ . Since the residual distribution has a large tail, the RMS of the distribution is higher ( $\sim 5.4 \mu\text{m}$ ). The tail in the residuals distribution is due to the reconstruction of the hit positions of single-pixel clusters where the charge sharing can not be used to improve the reconstructed position.

The residuals for the first telescope plane as a function of the Monte Carlo hit  $x_{\text{MC}}$  and  $y_{\text{MC}}$  are shown in Figure 6.6. The intrinsic resolution does not depend on the position of the hit. This confirms the coherence between the geometry description in the AllPix simulations and the EUTelescope reconstruction. The shape of these distributions is due to the beam profile which is more focused in the middle of the sensors.

### 6.3.3 Biased residuals on each telescope plane

The tracks on the telescope planes are reconstructed using a  $\chi^2$ -minimisation method as described in Section 5.4.1. The biased residual on each telescope plane is defined as the difference between the measured hit and the fitted track position. It determines the precision with which the track is reconstructed and depends on the hit resolution of the telescope sensors, the number of measurements and their positions

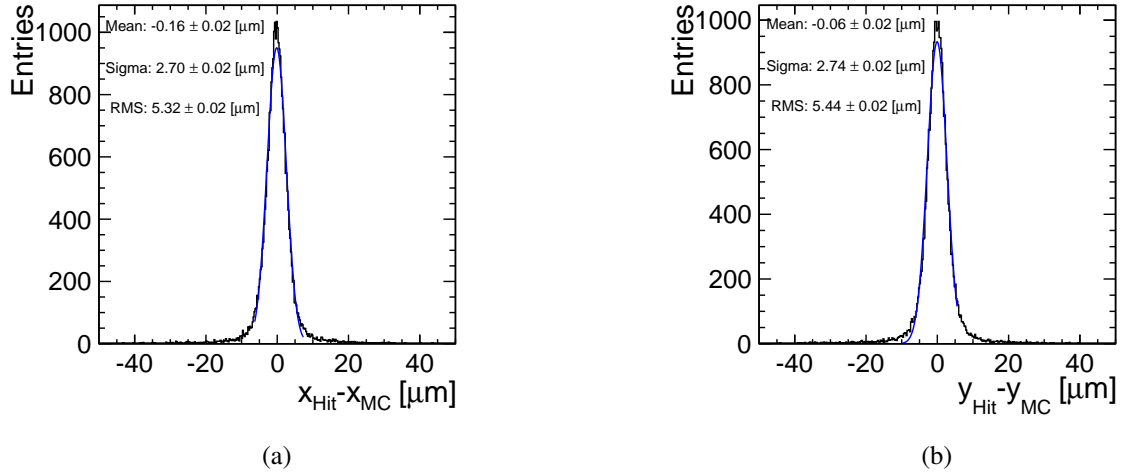


Figure 6.5: The hit residuals of a telescope plane in (a) x and (b) y directions given by comparing the MC and the reconstructed hit positions.

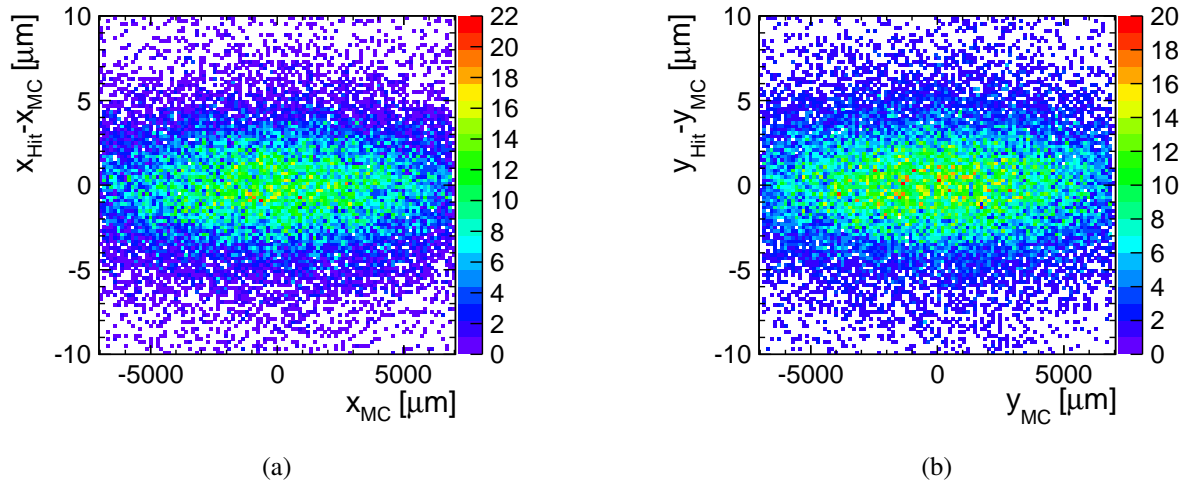


Figure 6.6: The hit residuals of the first telescope plane in (a) x and (b) y directions comparing the MC and the reconstructed hit positions as a function of the MC position.

and on the amount of multiple scattering. The residual is biased because the track fit includes the telescope plane of the measured hit.

The biased residual width  $r_b^2(z)$ , for tracks at all positions  $z = z_i$  at the telescope planes, can be expressed as [60]:

$$r_b^2(z) = \sigma_{int}^2(z) - \sigma_{t,b}^2(z), \quad (6.3)$$

where  $\sigma_{int}$  is the intrinsic hit resolution of the sensors and  $\sigma_{t,b}$  is the biased track resolution.  $\sigma_{t,b}$  determines the precision with which the particle trajectory is defined with a biased track. For the inner planes of the telescope, since more measurement points contribute to the track reconstruction,  $\sigma_{t,b}$  decreases which leads to higher values for the biased residuals. Whereas, for the outer planes where less measurement points contribute (planes 0 and 6),  $\sigma_{t,b}$  gets worse (increases) resulting in a narrower  $r_b$  distribution.

The biased residuals depend highly on the quality of the tracks. The tracks with high  $\chi^2/\text{NDF}$  go through more multiple scatterings and therefore contribute to the tails of the biased residuals. For the in-pixel analysis done in Chapter 7, the tracks with a  $\chi^2/\text{NDF}$  higher than 100 are discarded. This cut is applied for all tracks used in this analysis.

Figure 6.7 shows the  $\chi^2/\text{NDF}$  distributions in data (a) and in simulations (b) with the cut at 100 on the  $\chi^2/\text{NDF}$  as illustrated with a red line.

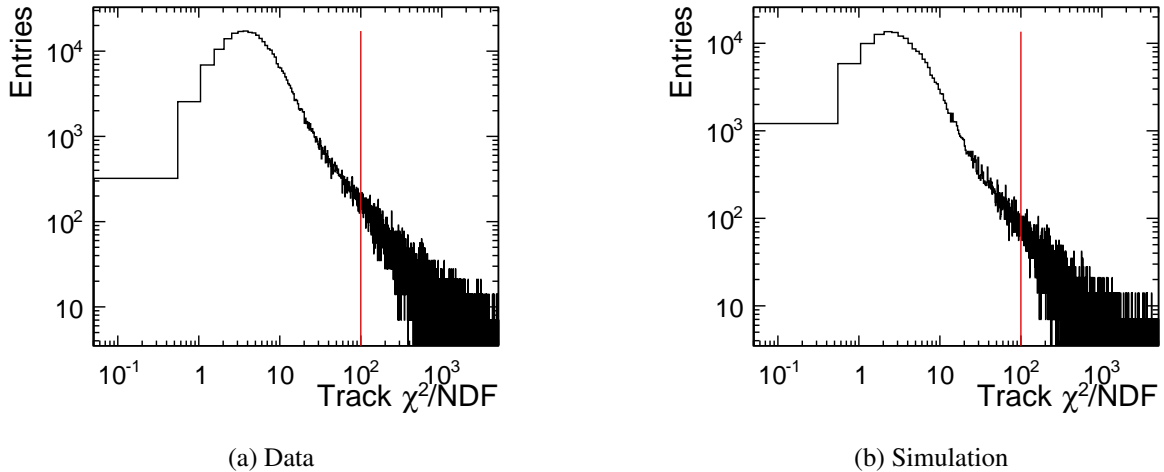


Figure 6.7:  $\chi^2/\text{NDF}$  distributions for reconstructed telescope tracks for (a) data and (b) simulation. A cut is applied to discard the tracks with  $\chi^2/\text{NDF}$  higher than 100 (illustrated with the red line).

Figure 6.8 compares the RMS of the biased residuals in data and simulations for a cut applied to discard the tracks with  $\chi^2/\text{NDF}$  higher than 100. The residual distributions are given in Figures B.1 and B.2 for data and Figures B.3 and B.4 for simulation.

As expected, the inner planes show a higher biased residual than the outer ones. The simulation is in good agreement with data ( $\sim 5 - 15\%$  deviation). This means that the hit resolution of the telescope planes and the amount of multiple scattering in the simulation are close to reality and the simulation can be used to get a good estimation of the tracking resolution on the DUT.

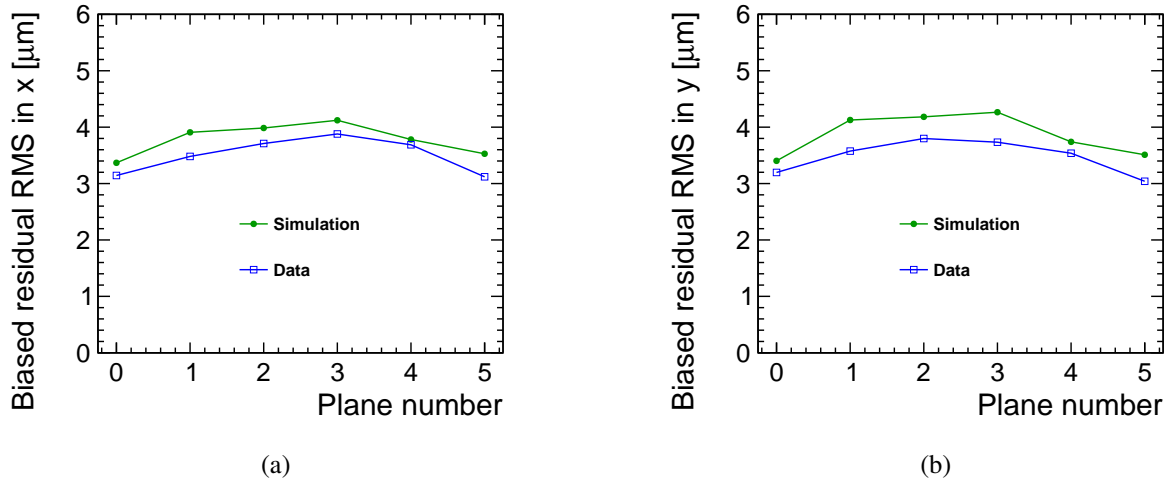


Figure 6.8: The RMS of the biased residuals  $r_b$  in the (a) x and (b) y directions comparing the data and simulation for the telescope planes. A cut is applied to discard the tracks with  $\chi^2/\text{NDF} > 100$ .

### 6.3.4 Tracking resolution on the DUT

The tracking residuals on the DUT in the x and y directions are shown in Figure 6.9. This value can only be obtained in simulations, as the MC position is needed. For this calculation, the cut of  $\chi^2/\text{NDF} < 100$  as shown in Figure 6.7 is applied for the track selection.

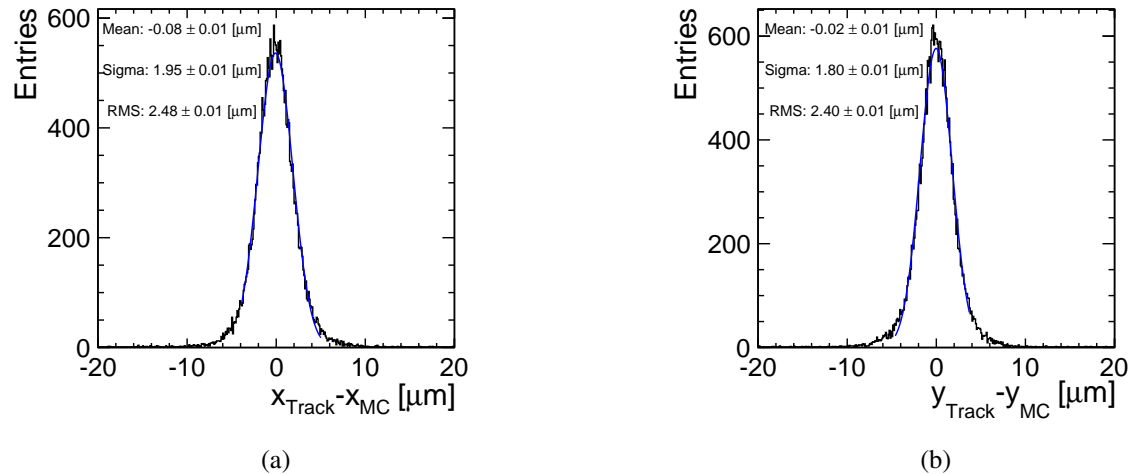


Figure 6.9: The track residuals on the DUT comparing the reconstructed track position to the true position of the particles obtained from GEANT4 in AllPix simulations in (a) x and (b) y directions.

The standard deviation of the distributions is less than 2 μm when fitted by a Gaussian on the central 95.5% of the residual distribution. The RMS of the residuals is slightly higher than 2 μm due to the tails of the distribution. A more strict cut on the  $\chi^2/\text{NDF}$  discards tracks in the tails and reduces the RMS of the distribution but also causes loss of statistics.

The tracking resolution on the DUT as a function of the  $x_{\text{MC}}$  and  $y_{\text{MC}}$  positions is shown in Figure 6.10. The resolution on the DUT does not depend on the position of the track. This confirms the coherence

between the geometry description in the AllPix simulations and the EU Telescope reconstruction. The shape of these distributions is due to the beam profile which is more focused in the middle of the sensors.

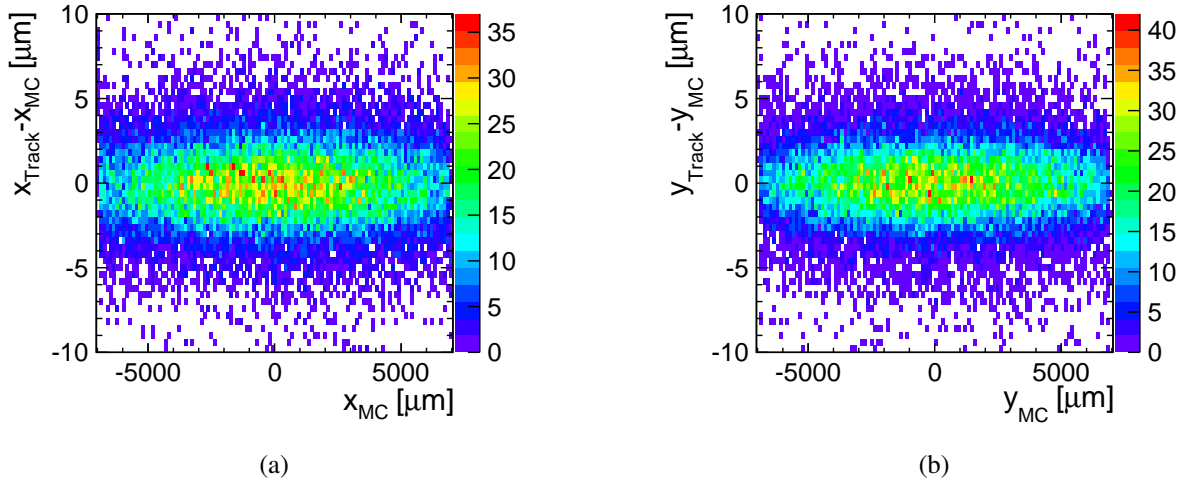


Figure 6.10: The tracking resolution on the DUT in (a) x and (b) y directions as a function of the MC position.

## 6.4 Summary

The simulations confirm that the Timepix3 telescope allows for a high-resolution track reconstruction on the DUT ( $\sim 2 \mu\text{m}$ ). This telescope is therefore suited for in-pixel studies and testing of DUTs with high resolution constraints as required for the CLIC vertex detector. In the following, the Timepix3 telescope is used to precisely characterise the performance of thin sensors.



# CHAPTER 7

---

## Thin sensors studies

---

As part of the R&D programme for the CLIC vertex detector, the performance of thin silicon sensors is quantified using the Timepix3 readout chip with 55  $\mu\text{m}$  pixel pitch. 50  $\mu\text{m}$  to 150  $\mu\text{m}$  thick planar sensors are bump-bonded to 700  $\mu\text{m}$  thick Timepix3 ASICs and tested with particle beams.

The AllPix simulation framework (described in Section 5.2) is used to simulate the performance of thin sensors and to understand the charge sharing in such sensors. A digitiser is designed in AllPix which simulates the sensor and the readout ASIC. Data are used to validate the simulations. The simulation is finally extrapolated to predict the spatial resolution for smaller pixels of 25  $\mu\text{m}$  pitch which is aimed to be achieved for the CLIC vertex detector.

### 7.1 Thin-sensor assemblies

A list of Advacam planar n-in-p thin sensors (50 – 150  $\mu\text{m}$  thick) bump-bonded to Timepix3 readout ASICs is shown in Table 7.1. These assemblies are tested using the CLICdp Timepix3 pixel-beam reference telescope at the CERN SPS with the experimental setup as described in Section 6.1.

Table 7.1: Nominal operating bias voltage, threshold in DAC and calibrated in number of electrons (measured as described in Section 4.6.1) for the Advacam planar n-in-p assemblies bump bonded to Timepix3 ASICs.

Timepix3 ID	Thickness [ $\mu\text{m}$ ]	Bias voltage [V]	Threshold [DAC]	Threshold [ $e^-$ ]
W19_G7	50	-15	1190	$505 \pm 31$
W19_F7	50	-15	1187	$566 \pm 33$
W19_L8	50	-15	1133	$546 \pm 31$
W19_C7	50	-15	1148	$571 \pm 34$
W5_E2	100	-20	1160	$537 \pm 33$
W5_F1	150	-30	1153	$536 \pm 31$

#### 7.1.1 Operating conditions

The Timepix3 readout ASICs were operated with the optimised parameters as described in Table 4.6. The nominal values for the threshold and the bias voltage are shown in Table 7.1. For the nominal bias voltage, the sensor is fully (or over) depleted. The nominal threshold set insures that the readout chip is not operating under noisy conditions. The error on the threshold is due to the threshold dispersion

after the chip equalisation. Section 4.5 describes the procedure for the selection of the nominal threshold value. These nominal values are held throughout the data taking except for the cases where the threshold or the bias voltages are scanned.

## 7.2 Experimental and simulated results for thin sensors

This section gives an overview on the performance of thin sensors. The AllPix simulations of thin sensors are validated using test-beam data.

### 7.2.1 Calibrated test beam data

The test pulse calibration as described in Section 4.6.2 is applied to the test beam data in order to convert the TOT values into energy deposited by the MIP particles in units of the number of electrons generated.

Figure 7.1 shows the TOT distribution for one, two, three and four-pixel clusters. The most-probable-value (MPV) of the TOT distributions for different cluster sizes do not fully align due to the non-linear behaviour of the Timepix3, as sharing the same deposited charge amongst several pixels results in each pixel having a higher TOT than would be expected from simply scaling the charge. The calibrated energy distribution aligns for different cluster sizes since the calibration takes into account the non-linearities of the chip as shown in Figure 7.2. For the 50  $\mu\text{m}$  thick sensor, the calibrated distributions do not align since higher deposited energies tend to give higher cluster sizes and the distributions for larger cluster sizes are biased towards larger energy depositions.

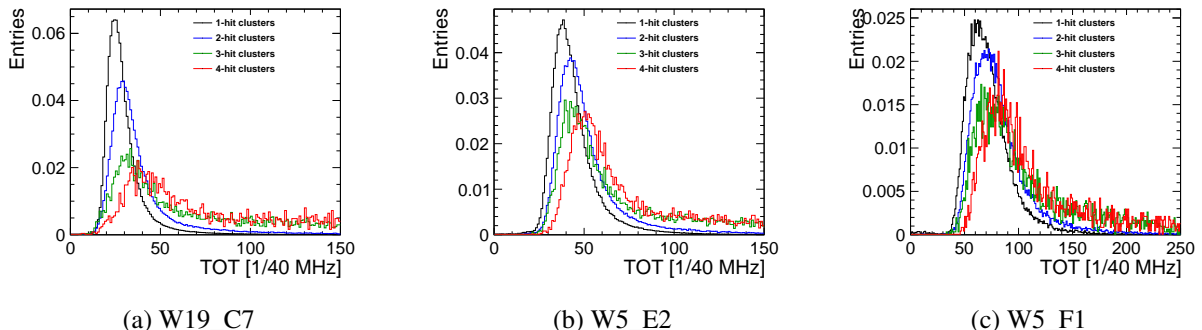


Figure 7.1: TOT distribution for one, two, three and four-pixel clusters for assemblies with (a) 50  $\mu\text{m}$ , (b) 100  $\mu\text{m}$  and (c) 150  $\mu\text{m}$  thick planar sensors.

Figure 7.3 compares the total energy deposition in a cluster in data and simulation for all cluster sizes combined. The most-probable-value and the width of the distributions in data and simulation agree. Therefore the calibration is validated using the test-beam data. For the simulation, the PAI physics list is used which provides an energy deposition spectrum similar to the Bichsel distribution (see Figure 5.1). This confirms that the Bichsel model describes well the energy deposition in thin silicon sensors.

### 7.2.2 Measurement of the depletion voltage

The depletion voltage corresponds to the voltage at which the sensor is fully depleted and the charge is collected over the full thickness of the sensor. In normal operation, only the charge created in the depletion region can be detected. The sensor should be fully depleted to collect the maximal signal charge possible. The depletion voltage can be measured in test beams by scanning the bias voltage. The

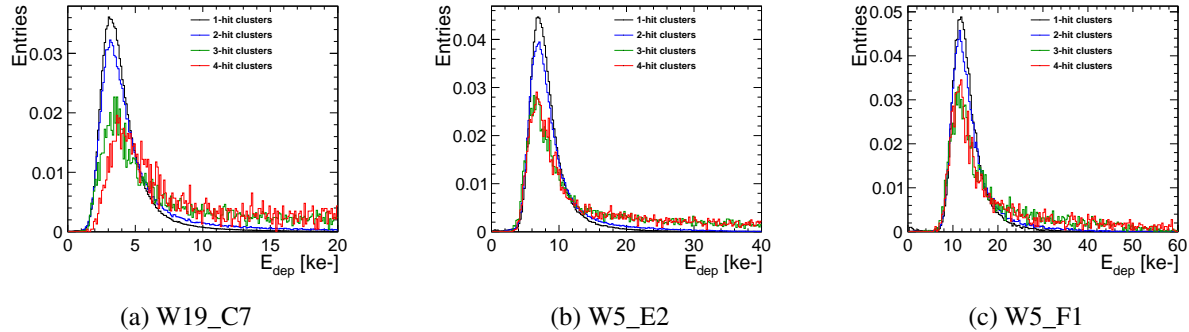


Figure 7.2: Energy deposition distribution for one, two, three and four-pixel clusters for assemblies with (a) 50  $\mu\text{m}$ , (b) 100  $\mu\text{m}$  and (c) 150  $\mu\text{m}$  thick planar sensors.

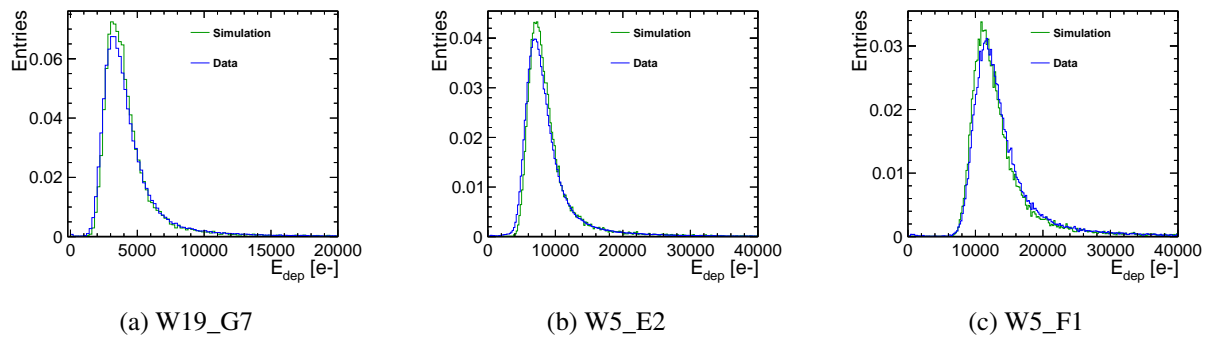


Figure 7.3: The energy deposition for all cluster sizes in simulation and data for (a) 50  $\mu\text{m}$ , (b) 100  $\mu\text{m}$  and (c) 150  $\mu\text{m}$  thick planar sensors. The assemblies are operated at nominal conditions.

depletion voltage and the sensor thickness are related by Equation (3.31). For lower bias voltages the sensor is under depleted, therefore the collected charge is reduced and is proportional to the square root of the bias voltage. After reaching the depletion voltage, the collected charge displays a plateau.

To obtain the depletion voltage, first, the distribution of the deposited energy in the sensor is fitted with a landau function convoluted with a Gaussian. The fit is done using RooFit [70] and an example is given in Figure 7.4(a). Figure 7.4(b) shows the most-probable-value (MPV) of the measured energy deposition as a function of the square root of the bias voltage. In this figure, two distinct regions can be seen: a sloped region and a plateau region. The depletion voltage of the assembly is obtained by calculating the intersection of a linear fit performed on both regions (defined by eye). The calculated depletion voltages for all assemblies are summarised in Table 7.2 and Figure C.1.

From the depletion voltage, the concentration of the dopants in the bulk is calculated to be around  $N_{\text{bulk}} \approx 1.3 \text{ m}^{-3}$  and corresponds to a resistivity of  $\rho \approx 10 \text{ k}\Omega \text{ cm}$  for all assemblies. The assemblies are confirmed to have high-resistivity silicon sensors. They are optimal for tracking detectors since it is possible to fully deplete them and high electric fields provide fast and efficient charge collection. The depletion voltage and the doping concentration are used as input for the simulation of these assemblies.

### 7.2.3 Cluster size distribution

The cluster size distribution is an indication for the amount of charge sharing in a sensor. For thicker sensors, more charge sharing is expected since the charge drifts over a longer distance and diffuses across

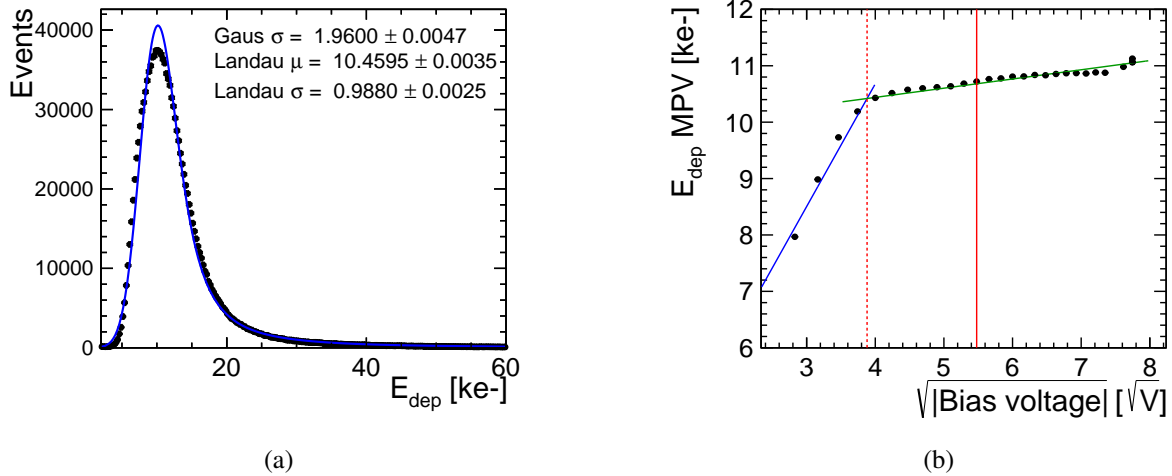


Figure 7.4: (a) The measured energy deposition distribution in a 150  $\mu\text{m}$  thick silicon sensor (W5\_F1) with a bias voltage of -30 V fitted with a Landau function convoluted with a Gaussian function. (b) The most probable value of the measured energy deposition as a function of the bias voltage for W5\_F1. Straight lines are used to fit the slope and the plateau regions. The depletion voltage corresponds to the intersection of these two regions and shown in a red dashed line. The continuous red line shows the nominal operating bias voltage.

Table 7.2: Measured depletion voltage for the assemblies described in Table 4.2 and calculated by fitting the plateau and slope regions of TOT as a function of the bias voltage.

Assembly	Depletion voltage [V]
W19_G7	-7
W19_F7	-7
W19_L8	-7
W19_C7	-7
W5_E2	-12
W5_F1	-15

a larger transverse area. The threshold of the readout electronics has a large impact on the detection of the charge sharing. The threshold should be as low as possible to avoid undetected energy deposits.

In this analysis, the hit pixels form a cluster with a distance criterion of  $\sqrt{2} \times \text{pitch}^1$ : pixels sharing common corners or edges are considered as clusters. For sensor thicknesses in the range of 50  $\mu\text{m}$ -150  $\mu\text{m}$ , clusters of size one to four are expected due to diffusion. Larger clusters are expected due to other effects such as  $\delta$ -rays. The most common cluster shapes are illustrated in Table 7.3.

Figure 7.5 compares the cluster-size distribution in simulations and data for the assemblies operated at nominal conditions. There is a good agreement between simulation and data within 2%.

The fraction of different cluster sizes depends on the operating conditions of the assemblies like the bias voltage and the threshold of the readout ASICs. Figure 7.6 shows the cluster size fraction for a 150  $\mu\text{m}$  thick sensor (assembly W5\_F1) operated at different bias voltages and thresholds.

Higher bias voltages reduce the amount of charge sharing since the drift time is lowered in a stronger

<sup>1</sup> The distance between the center of pixels sharing the same edges is 1×pitch and for pixels sharing common corners is  $\sqrt{2} \times \text{pitch}$ .

Table 7.3: Most common cluster shapes.

Shape	Cluster size	Size in $x$	Size in $y$	Name
	1	1	1	size 1 ( $1 \times 1$ )
	2	2	1	size 2 ( $2 \times 1$ )
	2	1	2	size 2 ( $1 \times 2$ )
	3	2	2	size 3 ( $2 \times 2$ )
	4	2	2	size 4 ( $2 \times 2$ )

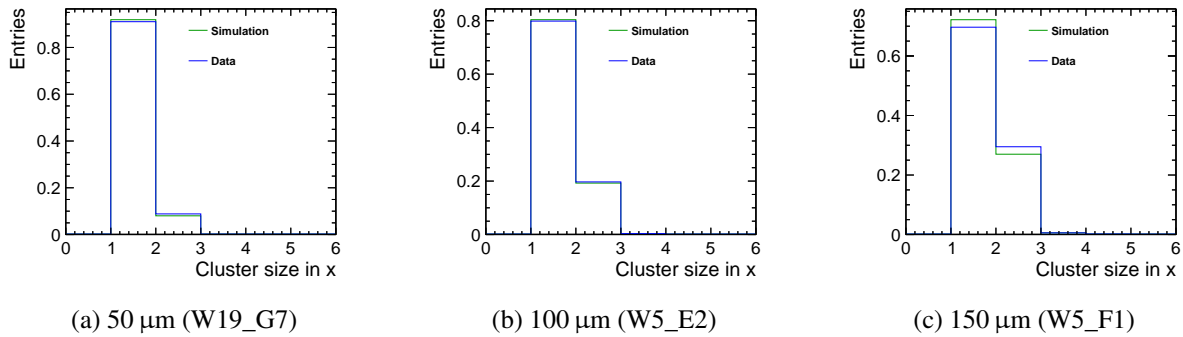


Figure 7.5: The cluster size distribution in simulation and data for 50  $\mu\text{m}$ , 100  $\mu\text{m}$  and 150  $\mu\text{m}$  thick sensors. The assemblies are operated at nominal conditions.

electric field and the charges diffuse less in the transverse direction. For very low bias voltages, the sensor is under-depleted. An increase in bias voltage in this regime increases the charge sharing. The pixel neighbouring a hit pixel is more likely to be over threshold as more charge is collected. The results for other assemblies are shown in Figure C.2.

Lowering the threshold leads to an increase in the average cluster size fraction distribution. Results for all assemblies are shown in Figure C.3.

The cluster size fraction as a function of the sensor thickness for data recorded at the nominal operating conditions is shown in Figure 7.7. Charge sharing increases with sensor thickness. The fraction of  $1 \times 2$  and  $2 \times 1$ -pixel clusters are very similar for square pixels and the curve labeled 2-pixel clusters combine these two cluster geometries. The simulation is in good agreement with data. Reasonable agreement is observed for high cluster sizes at 50  $\mu\text{m}$  sensors which can be explained by the non-linearity of the calibration curve for low energy deposition and close to the detection threshold resulting in high uncertainties in the detected charge measurements. The good agreement between data and simulation validates the digitiser as described in Section 5.2.4.

#### 7.2.4 Charge sharing as a function of the track position

The charge sharing is studied by extrapolating the track position obtained from the Timepix3 telescope to the DUT. The size of the clusters depends on the track position within the pixel. For perpendicular tracks,

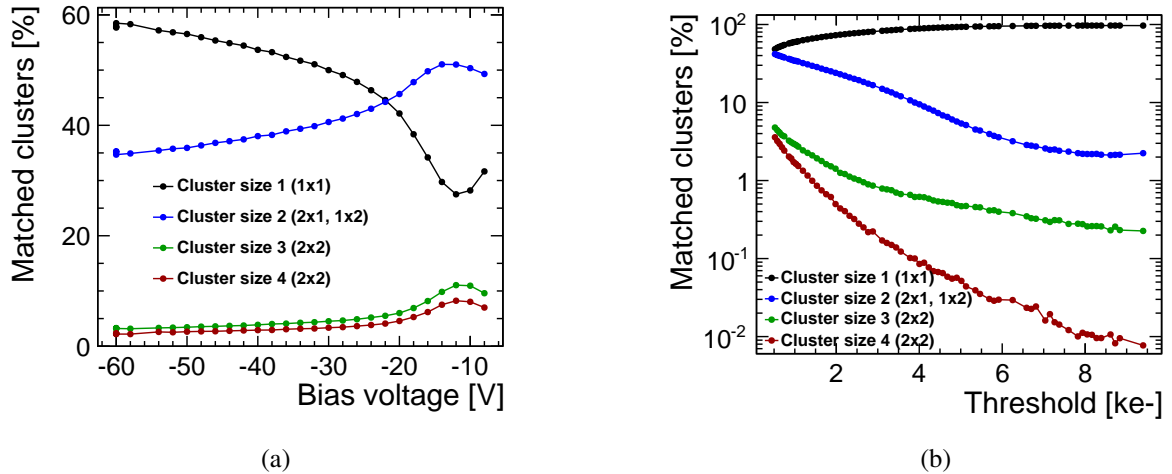


Figure 7.6: Cluster-size distribution as a function of (a) bias voltage and (b) threshold for the assembly W5\_F1 with a 150  $\mu\text{m}$  thick sensor.

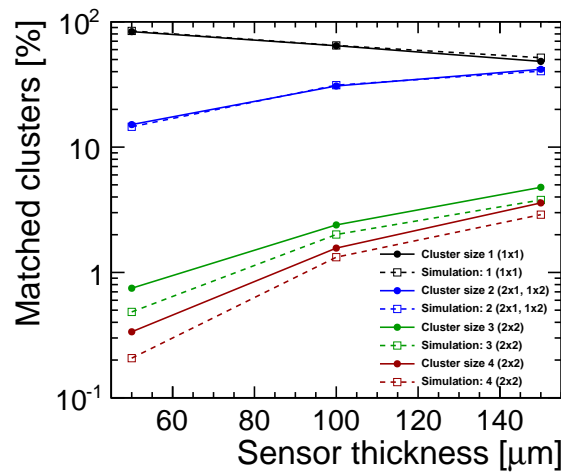


Figure 7.7: Cluster-size distribution for data and AllPix simulation as a function of sensor thickness for runs recorded under nominal operating conditions.

multi-pixel clusters are created when the track hits the edges or the corners of a pixel, leading to sharing of the charge between the pixel and its neighbouring pixels. The charge sharing is also affected by the operating threshold of the readout ASIC. Figure 7.8 illustrates the track position within the pixel for 1 to 4-pixel cluster sizes for a 50  $\mu\text{m}$  sensor. For other thicknesses, the track position within the pixel is shown in Figures C.4 to C.6. For thinner sensors, the track position has to be closer to the edges of the pixels to create two-pixel clusters.

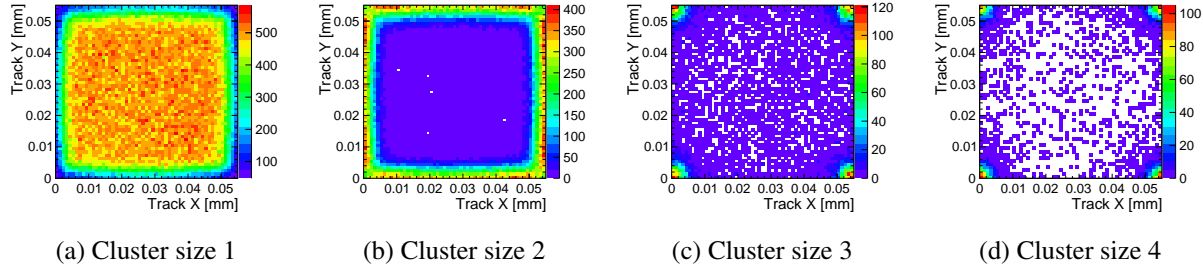


Figure 7.8: Extrapolated track position within the pixel for 1 to 4-pixel cluster sizes for a 50  $\mu\text{m}$  sensor (assembly W19\_G7). The assembly is operated at nominal conditions.

### 7.2.5 Single-point resolution

From the test-beam data, the residuals are calculated by comparing the reconstructed hit position with the extrapolated track position obtained by the telescope. This residual combines in quadrature the single-point (or hit) and the track resolutions:

$$\sigma_{\text{residual}}^2 = \sigma_{\text{hit}}^2 + \sigma_{\text{track}}^2. \quad (7.1)$$

In the following, the tracking resolution of  $\sim 2 \mu\text{m}$  is not unfolded from the residual measurements presented (see Section 6.3.4).

The residuals depend on the cluster sizes since the reconstructed hit position takes into account the number of the hit pixels in a cluster and the charge information in each pixel. Figure 7.9 illustrates the residuals for a 50  $\mu\text{m}$  thick sensor (assembly W19\_G7) for different cluster sizes. For single-pixel clusters, the hit position corresponds to the geometric center of the pixel and therefore the charge information can not improve the resolution. For multi-pixel clusters, the  $\eta$ -correction method (see Section 3.4.3) provides a more accurate interpolation of the hit position using the charge deposition (TOT) in the pixels hit and improves the resolution.

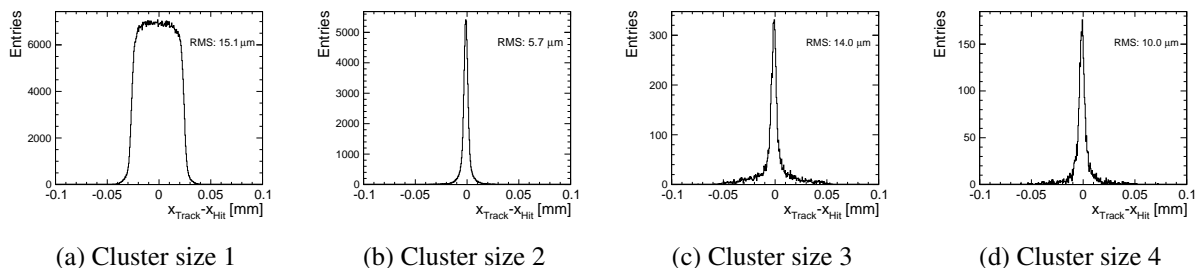


Figure 7.9: The residuals for a 50  $\mu\text{m}$  thick sensor (assembly W19\_G7) for different cluster sizes: (a) Cluster size 1 ( $1 \times 1$ ), (b) Cluster size 2 ( $2 \times 1$ ), (c) Cluster size 3 ( $2 \times 2$ ) and (d) Cluster size 4 ( $2 \times 2$ ).

The overall residual is defined by the RMS of the residual of all tracks combined. The distribution of the residuals for different sensor thicknesses operated at nominal conditions in simulation and data is shown in Figure 7.10. The wider component in the residual distributions corresponds to the single-pixel clusters. For thicker sensors, the fraction of multi-pixel clusters increases. This leads to a higher fraction of more precisely reconstructed hits and therefore the residual distribution gets narrower. There is a good agreement between simulation and data.

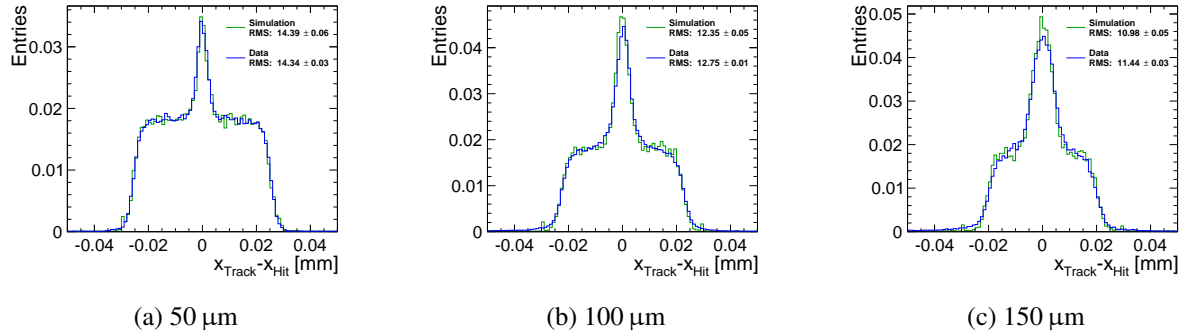


Figure 7.10: The residual distribution in the x (column) direction in simulation and data for the assemblies (a) W19\_G7, (b) W5\_E2 and (c) W5\_F1. The assemblies are operated at nominal conditions. The histograms are scaled to have unit area.

The factors affecting the fraction of different cluster sizes such as the sensor thickness and the operating conditions of the assembly (threshold and bias voltage) affect as well the residuals. Figure 7.11 shows the RMS of the residuals in the x (column) and y (row) directions for a 50  $\mu\text{m}$  thick sensor (assembly W19\_G7) as a function of the bias voltage and the threshold. The residuals follow the same trend as the cluster size distributions: higher fractions of single-pixel clusters result in larger residuals.

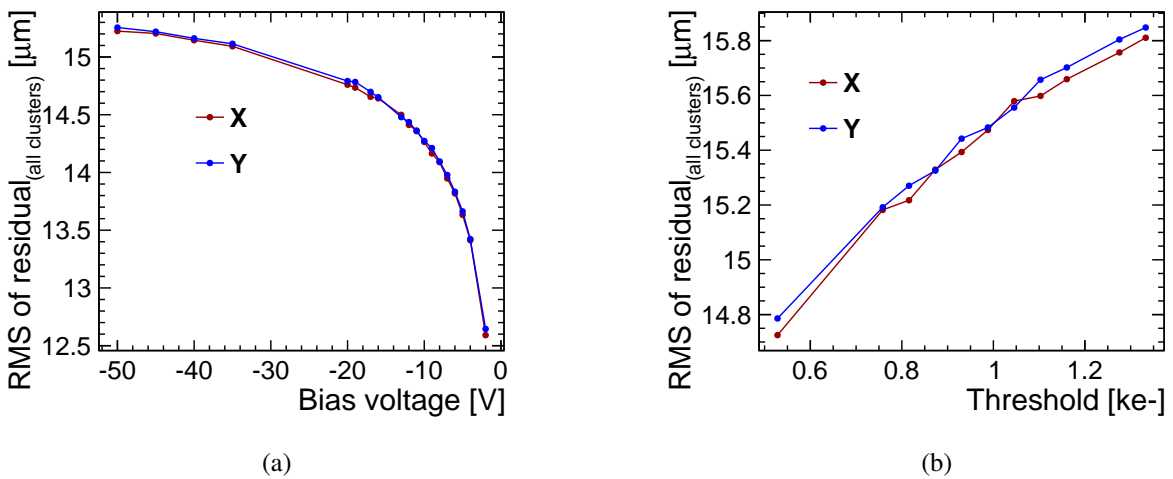


Figure 7.11: The RMS of the residuals in x (column) and y (row) directions as a function of (a) bias voltage and (b) threshold for a 50  $\mu\text{m}$  thick sensor (assembly W19\_G7).

For the assemblies operated at the nominal operating conditions, the RMS of the residuals in the x and y directions as a function of the sensor thickness are shown in Figure 7.12. For thicker sensors the fraction of multi-pixel clusters is higher and results in lower residuals. Again, a good agreement between

data and simulation is observed (less than 4% deviation).

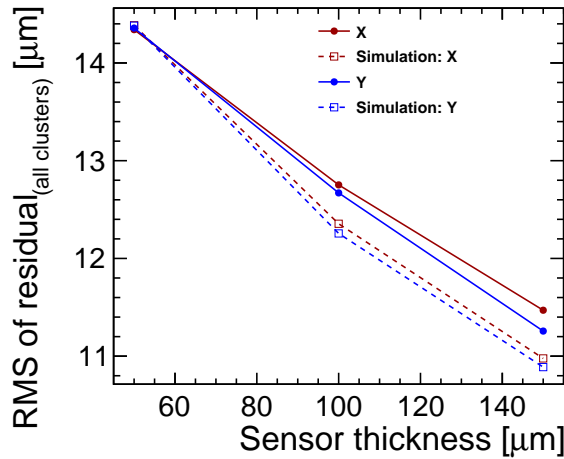


Figure 7.12: The RMS of the residuals in x and y directions as a function of the sensor thickness for assemblies operated at the nominal condition. The y-axis is zero-suppressed and the deviation between data and simulation is less than 4%.

### 7.2.6 Detection efficiency

The detection efficiency of the assemblies is defined as the fraction of total number of hits matched to tracks (within a circle of radius 0.1 mm around the predicted track position) and the total number of tracks projected to pass through the assembly. The efficiency is calculated within the matrix of  $256 \times 256$  pixels of the main sensor area. The calculation of the efficiency does not exclude the track hitting the masked or hot pixels, therefore the efficiency is slightly lower than 100% (see Table 4.3 for the number of masked pixels during the data taking).

The detection efficiency is strongly related to the operating threshold of the readout ASIC. With a lower threshold, smaller energy depositions can be measured and it is more likely to detect a particle. Figure 7.13 shows the detection efficiency for different sensor thicknesses. For thinner sensors, the energy deposition is lower and the efficiency drops more quickly by increasing the threshold than for thick sensors.

## 7.3 Extrapolation to smaller pixels

The Timepix3 readout ASIC has been used as a test vehicle for the characterisation of thin sensors. The test-beam measurements and the AllPix simulations show a good agreement. However, the Timepix3 ASIC has a pixel pitch of 55 μm and the goal for the CLIC vertex detector is to achieve pixels of pitch 25 μm. The CLICpix readout ASIC [71] implemented in 65 nm CMOS technology with a pitch of 25 μm is under development. A single-chip indium bump bonding process for 25 μm pitch is under development at SLAC [72] and a few assemblies with 50 μm and 200 μm thick planar sensors are successfully bump-bonded to CLICpix ASICs. These assemblies are currently under study [73].

Previously, we have seen a good agreement between the AllPix simulations and the data taken in the test beams for thin silicon sensors. The simulation can be used to predict the performance of thin sensors and small pitches in terms of charge sharing.

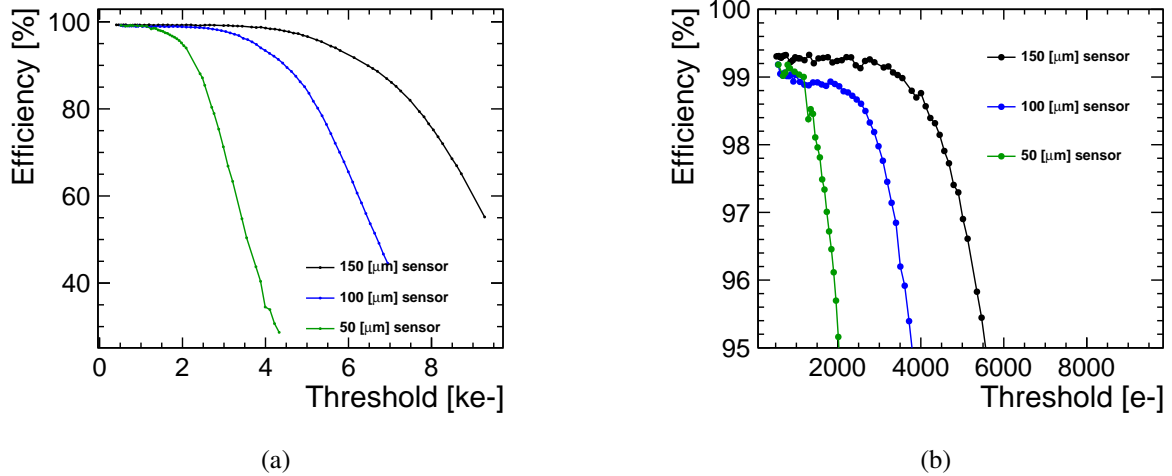


Figure 7.13: (a) Global detection efficiency as a function of the threshold of the readout ASIC for different sensor thicknesses (for the assemblies W19\_L8, W5\_E2 and W5\_F1). (b) focuses on the efficiencies between 95% and 100%.

Figure 7.14 shows the cluster-size distribution and the hit residuals (comparing the hit and the MC truth positions) for an extrapolation of the simulation to small pixels of size 10  $\mu\text{m}$  to 55  $\mu\text{m}$  with 50  $\mu\text{m}$  thick sensors with a Timepix3-type readout ASIC operated at 500 electrons threshold with 10-bit TOT measurement and an electronic noise of  $\sim 80$  electrons. The same digitiser as the one used to validate the simulation is used for the extrapolation. Even with a small pitch of 25  $\mu\text{m}$  as foreseen for the CLIC vertex detector, in such thin sensors,  $\sim 70\%$  of clusters originating from minimum ionising particles contain one pixel (the fraction of single-pixel clusters with a 55  $\mu\text{m}$  pitch is  $\sim 83\%$ ). The residual distribution is therefore dominated by the broad peak from single-pixel clusters and the resulting resolution of  $\sim 6 \mu\text{m}$  is still significantly worse than the required 3  $\mu\text{m}$ . Based on simulations, it can be concluded that the required resolution can not be achieved with planar sensors of 50  $\mu\text{m}$  thickness and 25  $\mu\text{m}$  pitch. A pixel pitch of 10  $\mu\text{m}$  allows for achieving a resolution of  $\sim 3 \mu\text{m}$  as required by CLIC. New sensor concepts with enhanced charge sharing [74] or integrated technologies with even smaller pixel pitch [75] are therefore required.

## 7.4 Summary

Test-beam measurements and GEANT4-based simulation studies for thin sensors using the Timepix3 ASIC are in good agreement. The simplified model for the diffusion of charges in silicon as described in Section 5.2.4 gives a good agreement with data in terms of energy-deposition spectrum, cluster-size distribution and residuals distribution. Therefore, the simulation is used for predicting the resolution of 50  $\mu\text{m}$  thin sensors with small pixel sizes of 25  $\mu\text{m}$ . This prediction shows the difficulty to achieve the required 3  $\mu\text{m}$  resolution with very thin planar sensors.

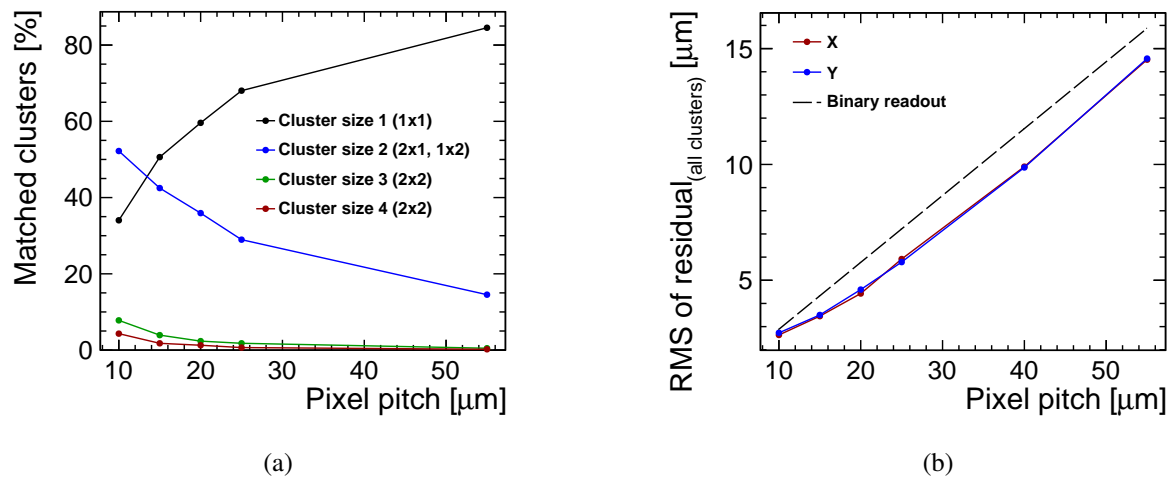


Figure 7.14: (a) Cluster-size distribution and (b) hit residuals, comparing the hit and the MC truth position, for the extrapolation of the simulation to small pixel sizes with a 50  $\mu\text{m}$  thick sensor and a threshold of  $\sim 500$  electrons. Binary readout refers to the geometric resolution of  $\text{pitch}/\sqrt{12}$ .



# CHAPTER 8

---

## Active edge sensors

---

Active-edge technology allows for seamless tiling of pixel sensors by depleting the sensors up to their physical edges. This allows for high coverage without creating overlaps between the pixel sensors and therefore reduces the material budget in the detector. The process consists of extending the backside implantation to the edge.

This technology is particularly interesting for the CLIC vertex detector where the material budget is constrained to be only 0.2%  $X_0$  per layer. Ladders of pixel detectors can be made without overlaps and with a high coverage.

In this chapter, the fabrication process for active edge sensors is described. Planar sensors produced by Advacam [44] and bump bonded to Timepix3 ASICs are tested in test beams. The signal collection and the efficiency at the edge are presented. Test beam results are compared to TCAD simulations.

### 8.1 The active-edge technology processing

Thin 50 – 150  $\mu\text{m}$  thick n-in-p planar sensors with active edges have been produced by Advacam [44] using a Deep Reactive Ion Etching (DRIE) process. The DRIE process is used to make trenches around the sensors and allows for extending the back-side implantation, and thereby the bias voltage, to the edge of the sensor by doping the sensor sides. The gradient of potential between the edge and the last pixel can be very high and could lead to a breakdown of the sensor. A guard ring (GR) consists of an n-implant with a metallic contact on top of it surrounding the pixel matrix close to the edge and thereby smoothening the potential transition between the edge and the neighbouring pixels. The guard ring can be kept floating or grounded by connecting it to the ground potential of the readout ASIC.

The active-edge sensors are bump bonded to Timepix3 readout chips (55  $\mu\text{m}$  pixel pitch) and studied in test beams and simulations. A list of produced assemblies is given in Table 8.1. These assemblies are the same as the ones studied in Chapter 4 and Chapter 7. In this chapter we focus on their edges.

Timepix3 ASICs provide an extra row of grounded pixels allowing to connect the guard ring to ground potential. Figure 8.1 shows a cross section of an active-edge sensor with and without guard ring.

Table 8.1: Details of different Advacam planar pixel sensors bump-bonded to Timepix3 readout ASICs. The edge distance is defined by the distance between the last pixel implant and the physical sensor edge.

Assembly	Thickness [μm]	Type	Edge distance [μm]	Guard-ring potential	Timepix3 ID
20-NGR-50	50	n-in-p	20	Without GR	W19_G7
23-FGR-50	50	n-in-p	23	Floating	W19_F7
28-GNDGR-50	50	n-in-p	28	Grounded	W19_L8
55-GNDGR-50	50	n-in-p	55	Grounded	W19_C7
55-GNDGR-100	100	n-in-p	55	Grounded	W5_E2
55-GNDGR-150	150	n-in-p	55	Grounded	W5_F1

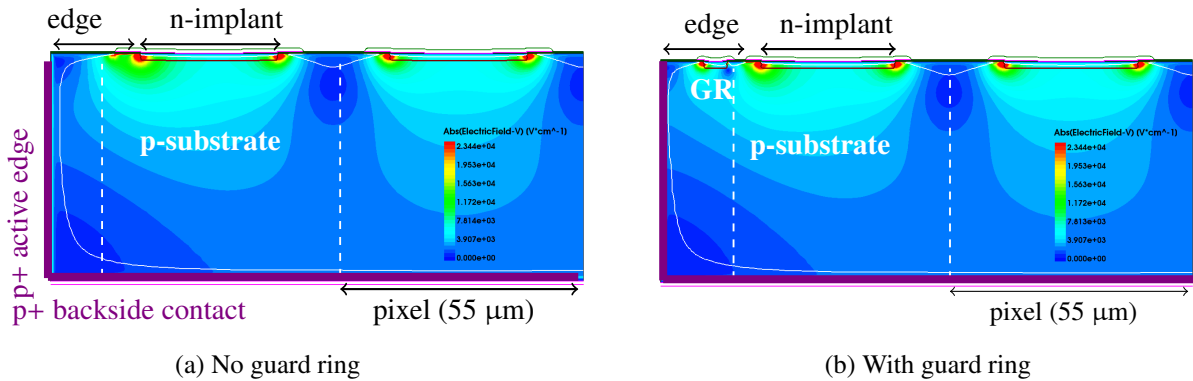


Figure 8.1: Schematic showing the cross section of a 50 μm thick sensor with active-edge technology. The pixel grid considered in the analysis is indicated with dashed lines. The electric field distribution obtained from a TCAD simulation with a bias voltage of 15 V is also illustrated. (a) does not contain any guard ring (GR) and (b) contains a guard ring at the edge.

### 8.1.1 Process flow for sensor production by the manufacturer

The process flow used by the manufacturer to produce active-edge n-in-p sensors is schematically illustrated in Figure 8.2 and described as follows [76].

- (a) First, the backside implantation is done by doping the detector wafer with borons.
- (b) The wafer is then bonded to a support wafer to perform the next steps.
- (c) By grinding and CMP (Chemical-mechanical planarisation) polishing the final detector thickness is obtained.
- (d) The dopings for the pixels and also the guard rings are implanted with phosphorus ions.
- (e) The DRIE etching is performed to uncover the edges of the detector.
- (f) Phosphorus ions are implanted to the sidewalls of the sensor to activate the edges.
- (g) Annealing of the sensor in order to activate the dopants and oxidation of the edges.
- (h) The opening of the contacts for the Aluminum patterning and the deposition of the under bump metallisation (UBM) layer for the pixels and guard rings.

- (i) The support wafer is finally removed and the backside metal is deposited. The sensor is ready to be bump bonded to the readout chip.

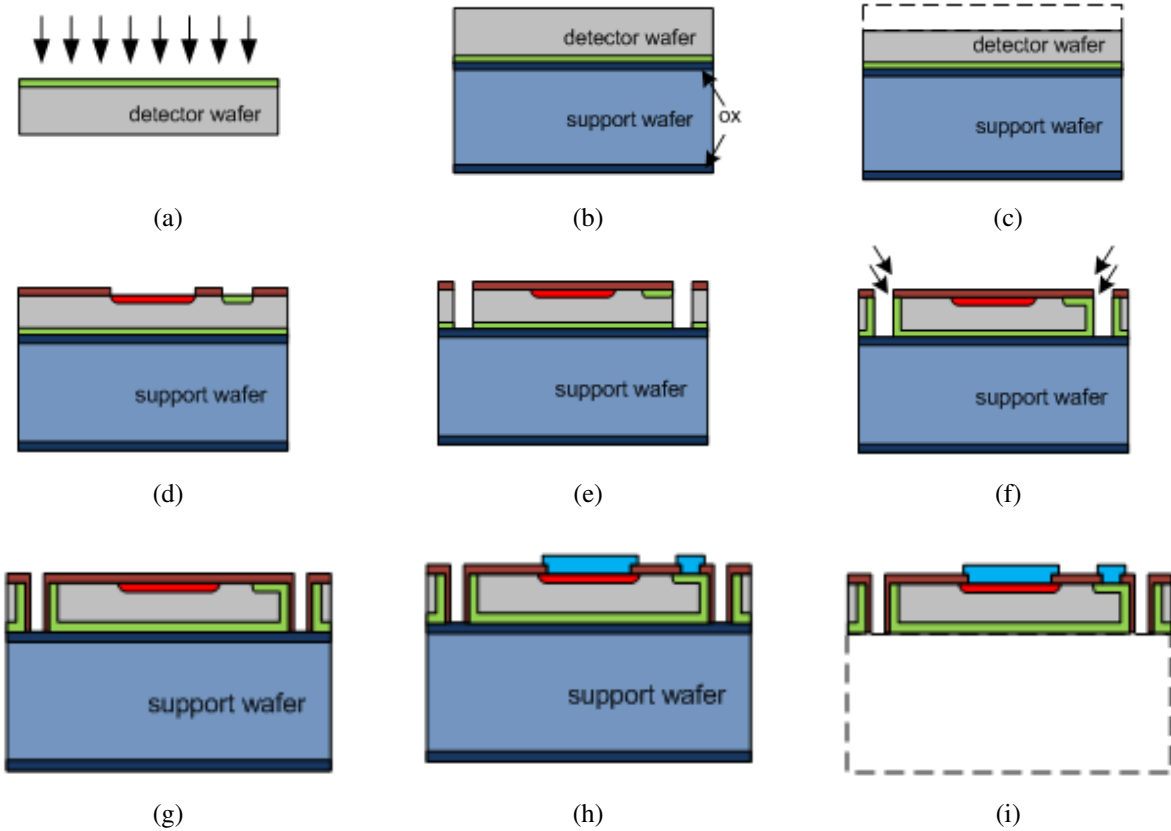


Figure 8.2: Schematic illustration of the process flow for the fabrication of planar n-in-p active edge sensors by the manufacturer [44].

### 8.1.2 Layout parameters of produced assemblies

Table 8.1 shows the assemblies tested in test-beam campaigns at the CERN SPS. The edge distance is defined by the distance between the last pixel implant and the physical sensor edge. The layouts of the assemblies are shown in Figure 8.3 and the colors defining the different sensor layers are described in Figure 8.4 and Table 8.2. The same convention is also used for describing the layers for the guard ring. Table 8.3 summarises the dimensions of the implants for the sensors. These dimensions are used for the implementation of the sensors in TCAD simulations.

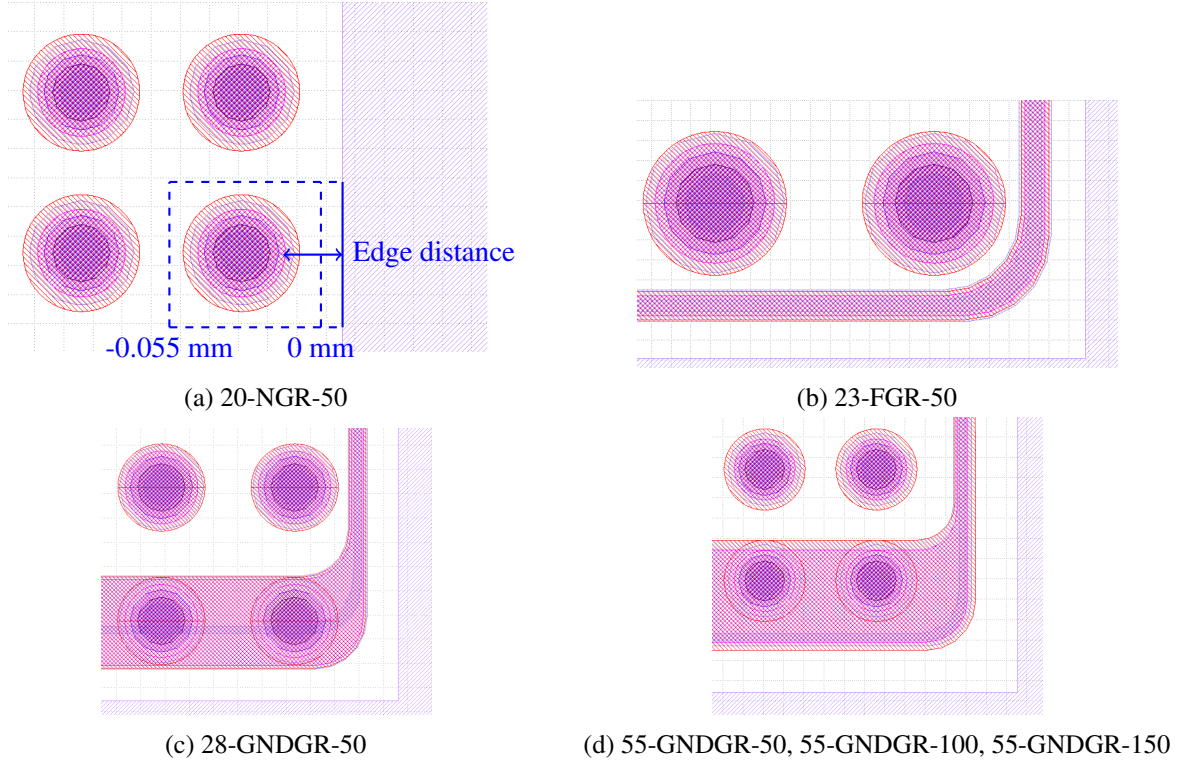


Figure 8.3: Sensor layouts for different guard-ring solutions for the assemblies described in Table 8.1. (a) shows the convention used in the following sections to express the efficiency and the charge distribution at the edge as a function of the track position. The border of the last pixel before the edge is indicated by a dashed line (at position 0 mm) and the physical sensor edge with a continuous line.

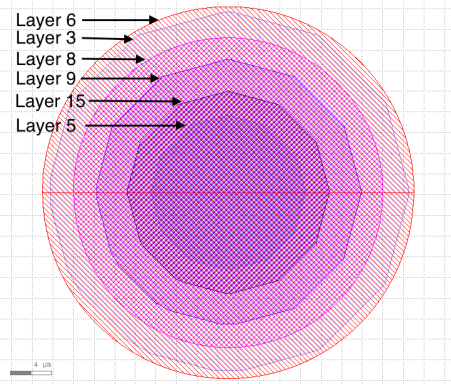


Figure 8.4: The different layers in the geometry description used for the sensor production.

Table 8.2: Layers in the geometry description used for the sensor production (Picture from 23-FGR-50).

Layer number	Layer
6	metal
3	mask to etch oxide
8	pixel implant
9	UBM
15	passivation opening
5	contact to connect Al to Si

Table 8.3: The dimensions of the different implants in the sensors listed in Table 8.1. The edge distance is the distance between the last pixel implant to the physical edge of the sensor as illustrated in Figure 8.3(a). The metal width is the diameter of the metal layer for the pixels. The doping width is the diameter of the pixel implant. The contact width is the diameter of the contact between silicon and metal. The GR offset is the distance between the physical edge of the sensor and the implant of the guard ring. GR doping width, contact width and metal with are respectively the width of the implant, the contact and the metal layer for the guard ring.

	20-NGR-50	23-FGR-50	28-GNDGR-50	55-GNDGR-50, 100, 150
Edge width [μm ]	20	23	28	55
Metal width [μm ]	40	36	36	40
Doping width [μm ]	30	30	30	30
Contact width [μm ]	15	15	15	15
GR offset [μm ]	-	10	14.5	25
GR doping width [μm ]	-	5	5	5
GR contact width [μm ]	-	3	3	3
GR metal width [μm ]	-	7	7	10

### 8.1.3 Process flow for the simulation of the active-edge designs

TCAD simulations (see Section 5.3) are used to simulate the fabrication process and the device operation of active edge sensors. The electric field and the electrostatic potential distributions within the sensor are calculated. For realistic simulations, the real dimensions of the assemblies as listed in Table 8.3 are used. Due to the computational power required for such simulations, the simulation is restricted to two pixels in a 2D configuration as shown in Figure 8.1.

The fabrication process of the sensors is simulated as follows:

1. The dimensions of the pixels, implants, contacts and metal layers are defined.
2. The silicon region is then defined for two pixels, the edge region and an extra silicon edge which will be etched later (to make the process more realistic). From the bias scan, the depletion voltage is measured for the assemblies (see Section 7.2.2) and therefore the resistivity is adjusted accordingly to  $\rho = 10 \text{ k}\Omega\text{cm}$ .

3. First a layer of  $0.2 \mu\text{m}$  thick oxide and then a layer of  $0.2 \mu\text{m}$  thick nitride are deposited on the top of the sensor.
4. The p-spray isolation technique is used to isolate the pixels from each other. Thus the silicon is implanted with borons at a concentration of  $1 \times 10^{12} \text{ cm}^{-2}$ . The implantation is done with an energy of 180 keV.
5. The nitride is etched at the positions of the implants for the pixels and the guard ring if the assembly contains one. First a mask is put on the positions where the nitride is going to stay. Then the etching is done at the implantation positions. Phosphorus (n-type material) is implanted with a concentration of  $1 \times 10^{15} \text{ cm}^{-2}$  with an energy of 120 keV.
6. The extra edge (as explained in point 2) is etched to achieve the edge distance of the assembly. In this process, first the nitride layer, then the oxide and finally the silicon layers are etched.
7. The sensor is flipped and a layer of oxide is deposited on the backside with a thickness of  $0.04 \mu\text{m}$ . Borons with a concentration of  $1 \times 10^{15} \text{ cm}^{-2}$  and an energy of 60 keV are implanted. Then the oxide is etched from the backside and the sensor is flipped again to the initial position.
8. The oxide is etched at the contact positions.
9. The meshing of the edge is refined adaptively depending on the concentration of the ions and for a thickness of  $1 \mu\text{m}$ .
10. A photoresist is deposited on the top of the sensor with a thickness of  $2 \mu\text{m}$ .
11. Borons are implanted to the edge with a concentration of  $1 \times 10^{15} \text{ cm}^{-2}$ , an energy of 60 keV and a tilt of  $15^\circ$ .
12. The photoresist is removed.
13. To activate the dopants, the sensor is annealed at a constant temperature of  $940^\circ\text{C}$  during 240 minutes.
14. The pixels and guard ring metal layer is deposited using an aluminium layer with a thickness of  $0.8 \mu\text{m}$ .
15. A layer of aluminium with a thickness of  $0.8 \mu\text{m}$  is deposited for the contact of the high-voltage on the back-side of the sensor.

The resulting doping concentration for the different layouts is shown in Figure D.1.

## 8.2 Electrical measurements and simulations

In silicon, the breakdown occurs for electric fields exceeding  $\sim 3 \times 10^5$  V/cm [77]. In active-edge sensors, since the back-side implantation as well as the bias voltage are extended to the edge of the sensor, the gradient of potential between the edge and the last pixel can be very high. This could lead to a breakdown of the sensor.

Figure 8.5 shows the measured leakage current in the different assemblies as a function of the bias voltage. For the nominal operation (at -15 V for 50  $\mu\text{m}$ , -20 V for 100  $\mu\text{m}$  and -30 V for 150  $\mu\text{m}$  thick sensors), none of the assemblies are operated beyond the breakdown voltage. The breakdown occurs earlier for the assembly without guard ring (20-NGR-50) compared to the other assemblies. The 50  $\mu\text{m}$  thick assemblies with the floating guard ring (23-FGR-50) and the grounded guard ring (28-GNDGR-50 and 55-GNDGR-50) lead to a similar breakdown. However, the floating guard ring is expected to smoothen the potential transition between the edge of the sensor and the first pixel and result in a higher breakdown voltage. This can be explained by the fact that the Timepix3 chip provides an extra row of pixels giving the possibility to connect the guard ring to the ground potential. The edge of 23-FGR-50 might get too close to the extra row of pixels leading to a high potential gradient in that region. The thicker sensors show a later breakdown.

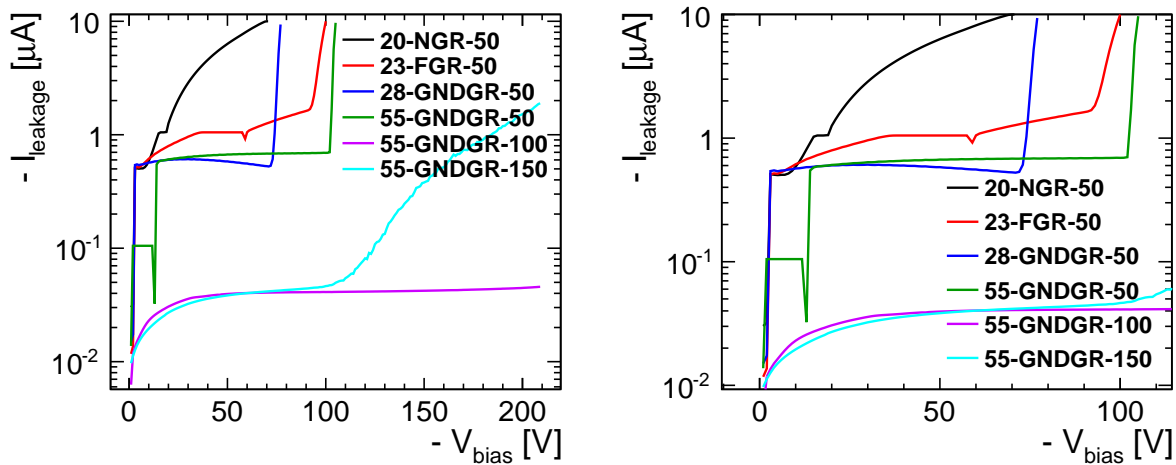


Figure 8.5: (a) Measured leakage current for active-edge assemblies listed in Table 8.1. For all assemblies, the measurements were done at the room temperature of 22° C. (b) focuses on the breakdown voltage and the leakage current for 50  $\mu\text{m}$  thick sensors.

In TCAD simulations, the electric field distribution for the sensors operated at nominal conditions are shown in Figure 8.6. In all cases, for the nominal conditions (see Table 7.1), the breakdown electric field is not reached in agreement with the simulated currents (see Figure 8.8).

The electric field and the electrostatic potential in TCAD simulations for a cut close to the n-implants (0.2  $\mu\text{m}$  from the sensor surface) are shown in Figure 8.7. Position 0  $\mu\text{m}$  corresponds to the position of the first pixel. The floating guard-ring (23-FGR-50) results in a smoother potential transition between the edge of the sensor and the first pixel.

Figure 8.8 shows the leakage current obtained from the TCAD simulations for the simulated pixel cell. In TCAD simulations, only the sensor is simulated and the effect of the readout chip and the bump bonding are not included. The readout chip can increase the temperature and the leakage current.

In simulations, the assemblies with grounded guard ring (including all sensor thicknesses) and without

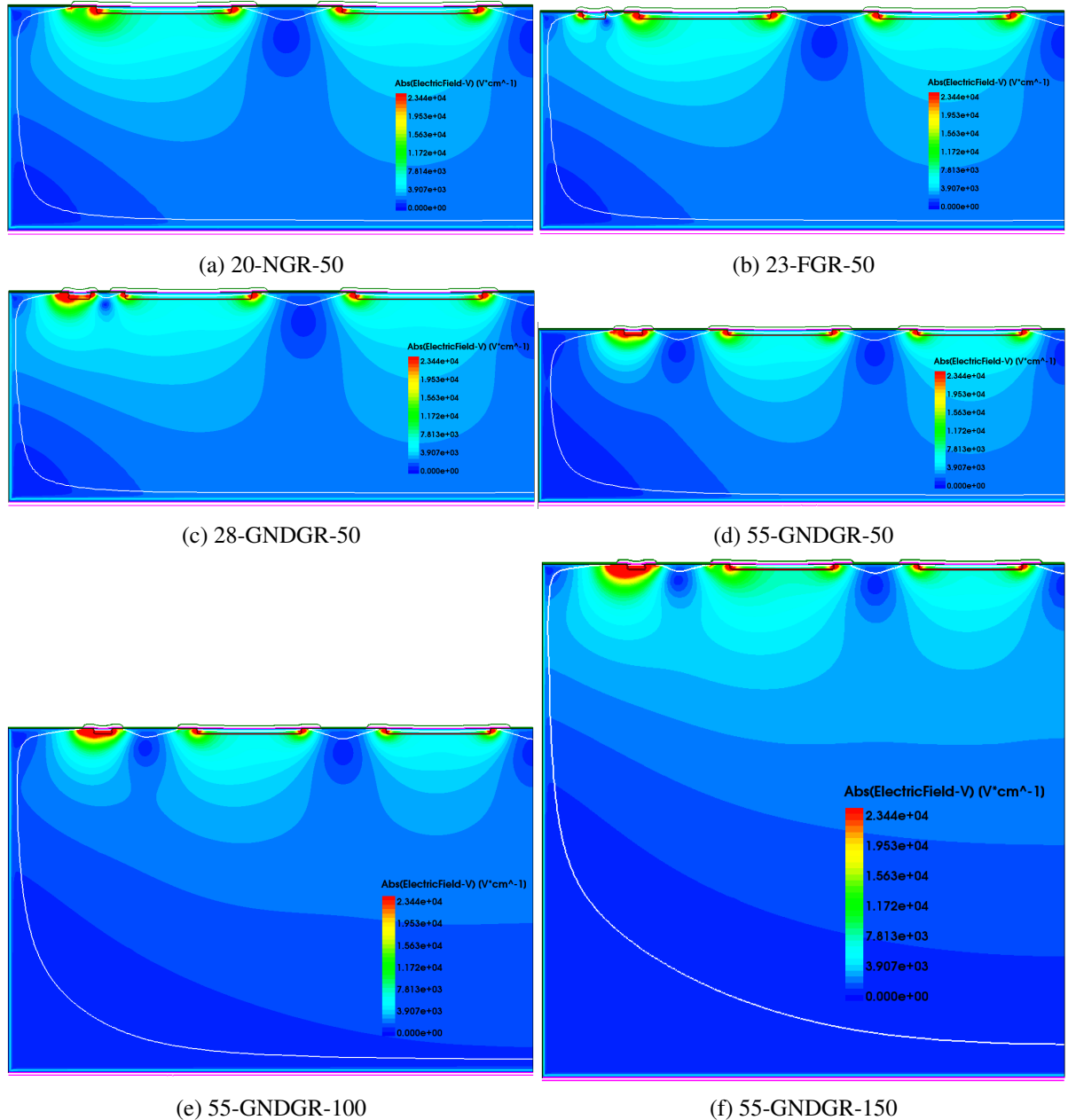


Figure 8.6: Electric field distribution in TCAD simulations for the assemblies listed in Table 8.1. The depletion region is shown with the white line.

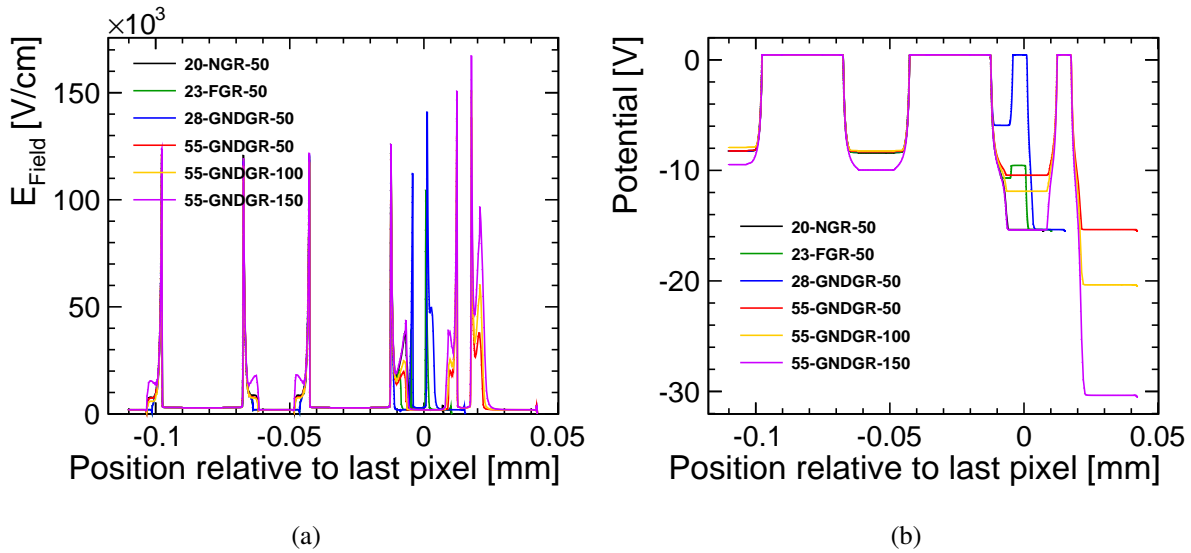


Figure 8.7: (a) The electric field and (b) the electrostatic potential for nominal bias voltage at a distance of 0.2  $\mu\text{m}$  below the sensor surface. Position 0  $\mu\text{m}$  corresponds to the position of the first pixel.

guard ring show a breakdown of the junction at around 150 V. In these sensors, the distance between the edge implant (with high voltage) and the ground implant (either the pixel or the guard ring) is similar which leads to a similar potential gradient and breakdown voltage. As expected, the floating guard ring shows a higher breakdown voltage of 240 V.

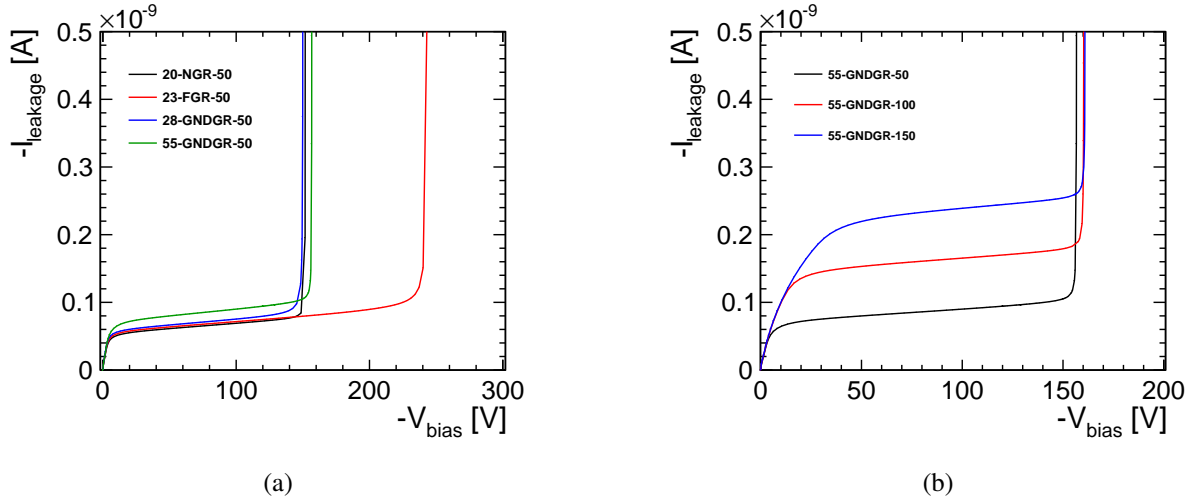


Figure 8.8: Leakage current in TCAD simulations for the pixel cell as a function of bias voltage for (a) 50  $\mu\text{m}$  thick sensors and for (b) assemblies with a grounded guard ring (refer to Table 8.1 for the details on the assemblies).

## 8.3 Edge performance in data and simulations

The active-edge assemblies are tested at the CERN SPS with 120 GeV pions (see Section 6.1), making use of the CLICdp Timepix3 beam reference telescope as described in Chapter 6. The collected charge at the edge is also simulated (as described in Section 8.3.1) and compared to the data. The edge performance is investigated in terms of the efficiency of detecting a track and the amount of collected charge as a function of the track position at the edge.

### 8.3.1 TCAD simulation of the detector response

TCAD simulations are used to study the charge collection at the edge region. The process flow as described in Section 8.1.3 is used to simulate two pixels and the edge region in a 2D configuration. The transient simulation of the active edge devices is done by a constant charge deposition corresponding to the peak of the straggling function along the particle track (see Section 3.2.2). Figure 8.9 illustrates an example of a MIP traversing the sensor at a distance of 10 µm from the left edge. The electron density 1 ns after the particle hits the sensor is shown.

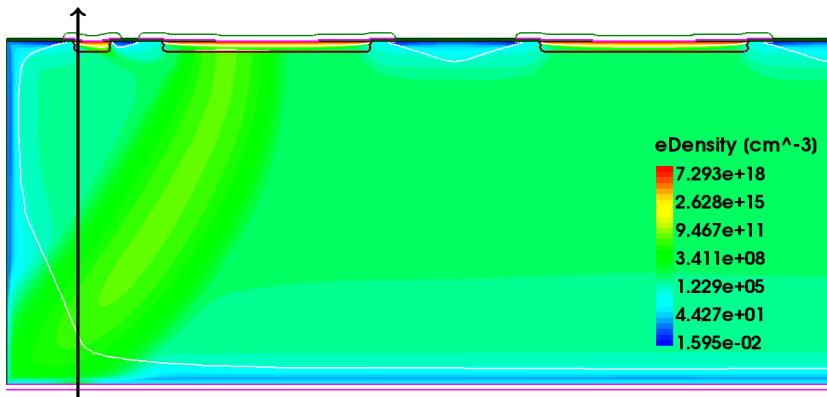


Figure 8.9: Transient simulation of a particle track traversing the sensor with a floating guard ring at a distance of 10 µm from the edge (illustrated as an arrow). The electron density 1 ns after the particle hit is shown. The region shown with a white line is the depletion region.

In simulation, hits are generated at different positions along the edge. The electrodes collect the signal pulse and integrate it over 15 ns. The peaking time of the signal is usually less than 5 ns therefore the integration time is enough to collect most of the signal.

### 8.3.2 Conventions used for the presentation of the results

The convention as illustrated in Figure 8.3(a) is used to show the performance of the different assemblies in Sections 8.3.3 and 8.3.4. The border of the last pixel (at 0 mm) is indicated with a dashed line and the physical sensor edge is shown as a continuous line. The detection efficiency is calculated by counting the number of tracks matched to hits on the DUT (with a distance criterion of 100 µm) divided by the total number of tracks projected on the DUT. The efficiency within the pixels is then mapped into a grid of 2 × 2 pixels. The x-axis shows the track position relative to the last pixel. The y-axis combines the tracks for the even rows (in the coordinates between 0 mm and 0.055 mm) and the odd rows (in the coordinates between 0.055 mm and 0.11 mm). The z-axis shows the efficiency. To increase the number of tracks close to the sensor edge, the beam was focused on only one of the edges during the data taking. An example of the track impact points for the assembly 20-NGR-50 is shown in Figure 8.10.

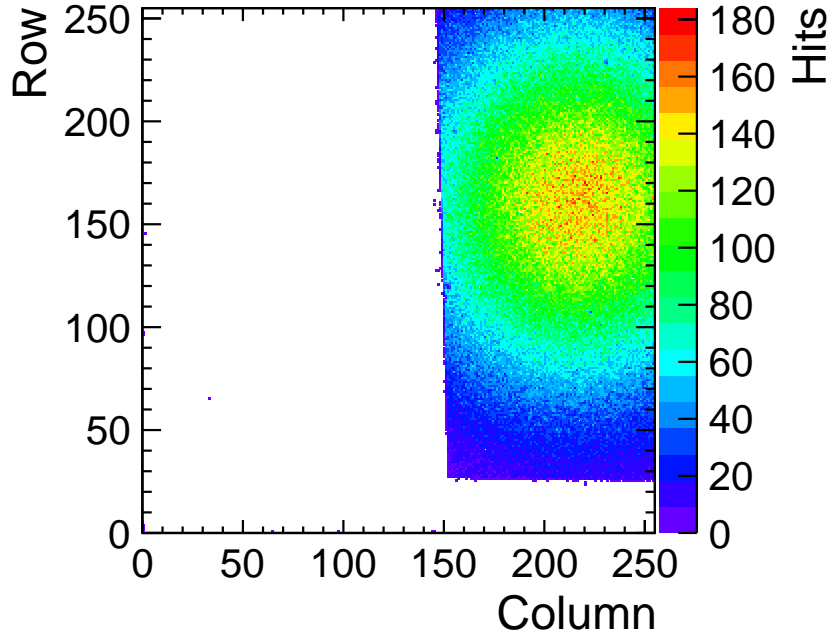


Figure 8.10: The track impact points on the assembly 20-NGR-50: the beam is focused on the edge of the assembly in order to increase the statistics for the edge performance studies.

The collected charge as a function of the track position is compared in data and TCAD simulations. In data, the deposited charge is plotted versus the track position given by the Timepix3 telescope (with a resolution of  $\sim 2 \mu\text{m}$ ). The deposited charge is obtained by applying the test-pulse calibrations to the TOT values measured in data (see Section 4.6.2). The most-probable-value (MPV) of the charge deposition in data is compared to the TCAD simulations.

To obtain the MPV of the energy deposition in data, only tracks within the central 40% of the pixel cell area are considered for all assemblies except for 28-GNDGR-50 where only the central 7% of the pixel is considered. This reduces the influence of the regions between the pixel implants in the row direction, which are not modeled in the 2D simulation. In these regions a larger loss of charge to the guard ring is expected. To calculate the MPV in data, the distribution of the deposited charge for each position is fitted with a Landau function convoluted with a Gaussian. The most probable value (MPV) of the Landau fit is then compared to the collected charge obtained in the TCAD simulations. In the TCAD simulations, a fixed amount of charge is deposited and the fluctuations of the deposited charge are not considered.

The tracking resolution of  $\sim 2 \mu\text{m}$  is applied to the hit position in TCAD simulations. This is done by convoluting a Gaussian function with a standard deviation of  $2 \mu\text{m}$  with the simulated hit position. The border of the last pixel (at 0 mm) is indicated with a dashed line and the physical sensor edge is shown as a continuous line with the convention as illustrated in Figure 8.3(a).

### 8.3.3 The performance of 50 $\mu\text{m}$ thick sensors

Exploiting the excellent tracking capabilities of the Timepix3 telescope, the efficiency at the edge of the assemblies with 50  $\mu\text{m}$  thick sensors is shown in two dimensions in Figure 8.11. The results are presented using the conventions as described in Section 8.3.2.

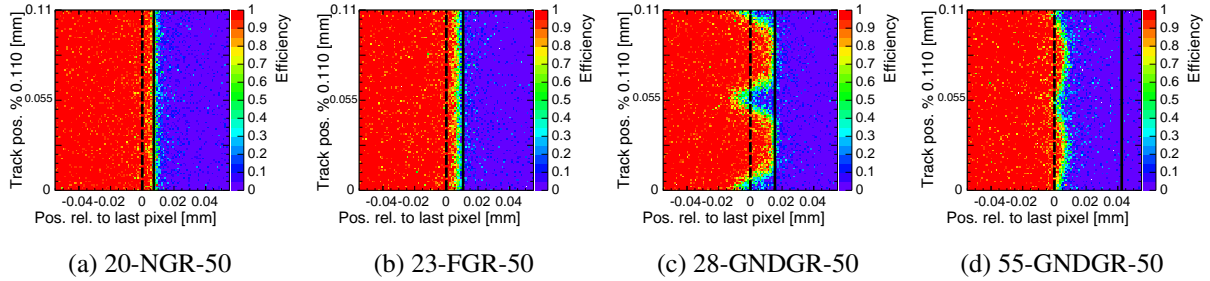


Figure 8.11: The efficiency at the edge as a function of the track positions for the assemblies having a sensor thickness of 50  $\mu\text{m}$ .

The assemblies without (20-NGR-50) and with floating guard ring (23-FGR-50) are efficient up to the physical edge of the sensor as shown in Figures 8.11(a) and 8.11(b). Figure 8.12 shows the charge collected at the edge as a function of the track position in data and TCAD simulations for 20-NGR-50 and 23-FGR-50. The charge is fully collected by the last pixel for 20-NGR-50. For 23-FGR-50, a loss of the charge near the edge is observed.

For 20-NGR-50, the TCAD simulation agrees well with the data observation as shown in Figure 8.12(a).

To simulate a floating guard ring for 23-FGR-50 in TCAD, the current on the electrode of the guard ring is set to zero. The charge drop in the edge is explained by the capacitive coupling between the guard ring and the surrounding implants. Data shows a higher charge drop in the edge than the TCAD simulations. This is expected, as the 2D simulation does not include the capacitive coupling over the full length of the guard ring.

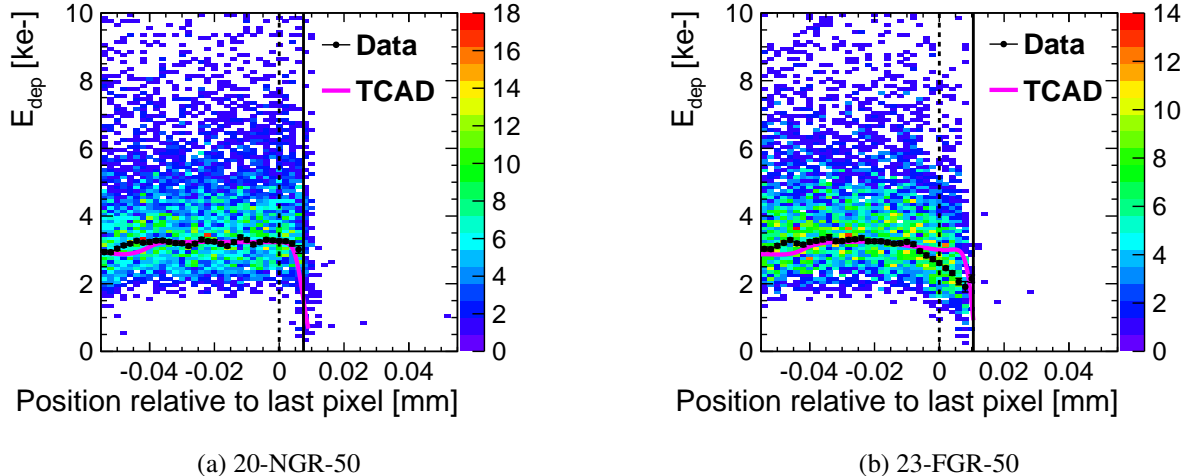


Figure 8.12: Charge collected as a function of the track position at the edge for the assemblies (a) 20-NGR-50 and (b) 23-FGR-50 in data and TCAD simulations. In data, only tracks within the central 40% of the pixel cell area are considered.

The grounded guard ring degrades significantly the detection efficiency at the edge for thin sensors of 50  $\mu\text{m}$ . For 28-GNDGR-50, the efficiency drops in-between pixels as shown in Figure 8.11(c). A large part of the charge is collected by the guard ring. For the assembly with larger edge distance (55-GNDGR-50), as shown in Figure 8.11(d), the edge is not efficient anymore.

For 28-GNDGR-50 and 55-GNDGR-50, both data and TCAD simulations show a drop in the collected

charge at the edge as shown in Figure 8.13. Most of the charge created in the edge is collected by the guard ring.

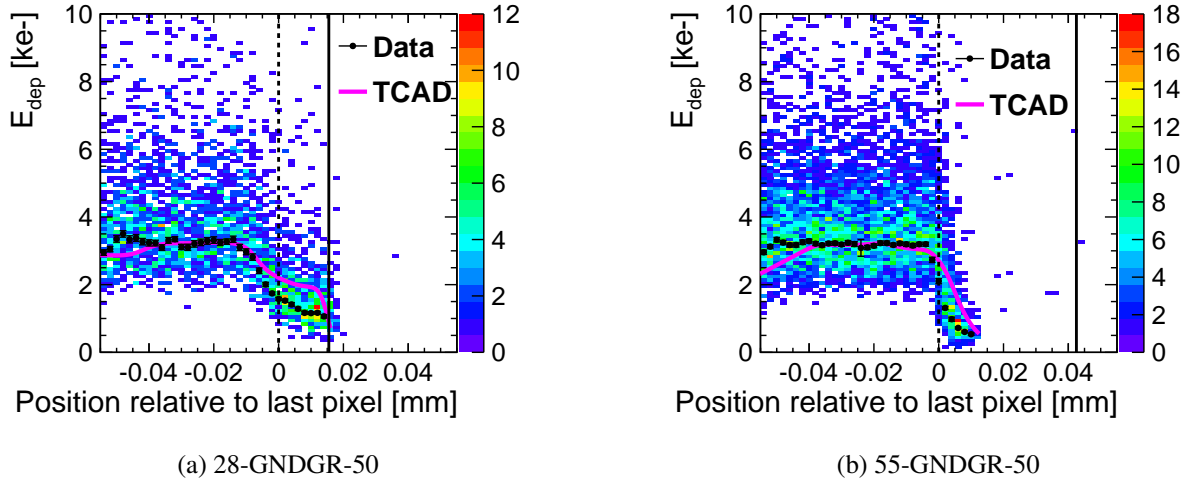


Figure 8.13: Charge collected as a function of the track position at the edge for the assemblies (a) 28-GNDGR-50 and (b) 55-GNDGR-50 in data and TCAD simulations. In data, only tracks within the central 7% for 28-GNDGR-50 and 40% for 55-GNDGR-50 of the pixel cell area are considered.

Electric field streamlines define a family of curves tangent to the velocity vector of the charge carrier flow. Figure 8.14 compares the distribution of the streamlines in the edge for different configurations of guard rings in TCAD simulations. The generated charge follows the streamlines and gets collected by the implants. In the case where there is no guard ring, all streamlines reach the first pixel. As confirmed by the data, all the charge in the edge is collected without loss. In the case of a floating guard ring, some streamlines reach the guard ring. This means that some charge is lost in the guard ring instead of being collected by the first pixel. Finally, in the case of a grounded guard ring, more streamlines end up in the guard ring. This explains also the larger drop in the collected charge and efficiency in the edge region.

For thin sensors, a floating guard ring appears to be the most suitable solution, as it shows a high detection efficiency at the edge and an acceptable breakdown behaviour.

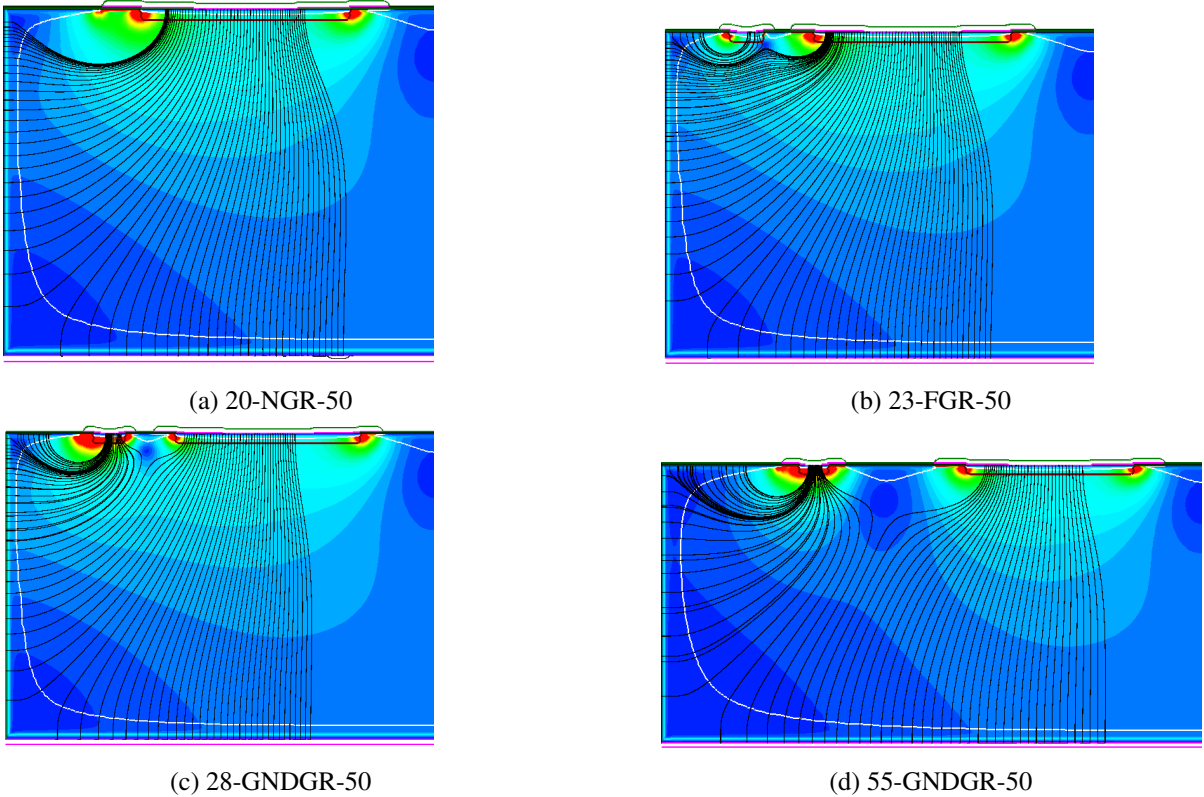


Figure 8.14: The electric field and the streamline distributions for different configurations of guard ring for 50  $\mu\text{m}$  thick sensors. The generated charges follow the streamlines. The depletion region is indicated by solid white lines.

### 8.3.4 The performance of 100 $\mu\text{m}$ and 150 $\mu\text{m}$ thick sensors

The assemblies 55-GNDGR-100 and 55-GNDGR-150 are efficient up to the edge as shown in Figure 8.15. A slight loss of the charge near the edge in data and simulations can be observed for these assemblies as shown in Figure 8.16. However, due to the large amount of the ionisation charge, the signal does not drop below the detection threshold and therefore the assembly remains efficient up to the physical edge of the sensors.

For further investigation, Figure 8.17 shows the electric field and the streamline distributions for the 100  $\mu\text{m}$  and 150  $\mu\text{m}$  thick sensors. For thicker devices, some streamlines are reaching the guard ring but most of the charge is collected by the pixels due to the thicker silicon bulk. The devices remain still efficient up to 100% even very close to the physical edge. Therefore, for the thicker sensors of 100  $\mu\text{m}$  and 150  $\mu\text{m}$ , the grounded guard ring is a suitable solution.

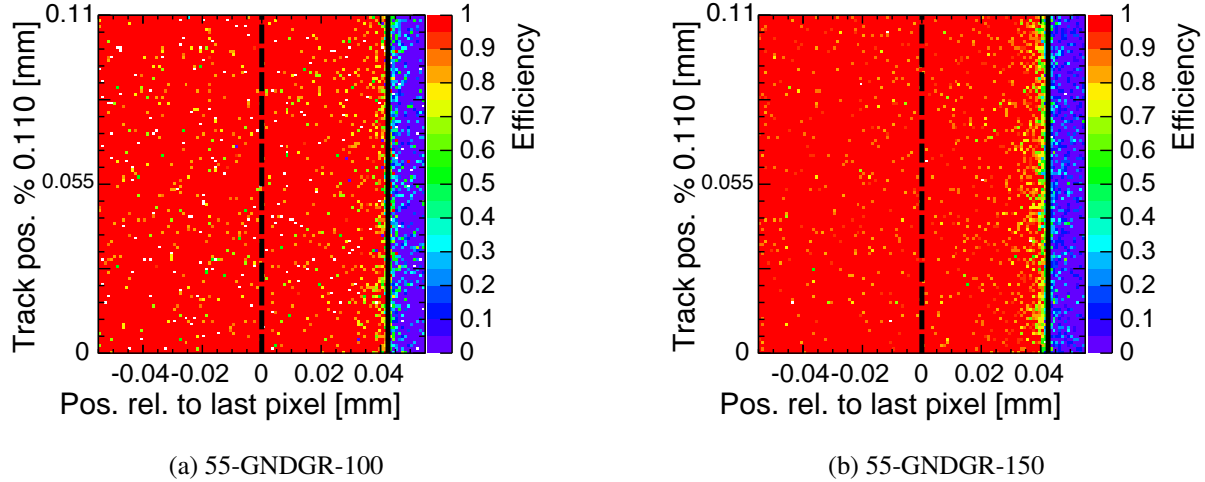


Figure 8.15: The efficiency at the edge as a function of the positions for the assemblies having sensors with thicknesses of (a)  $100\text{ }\mu\text{m}$  and (b)  $150\text{ }\mu\text{m}$ .

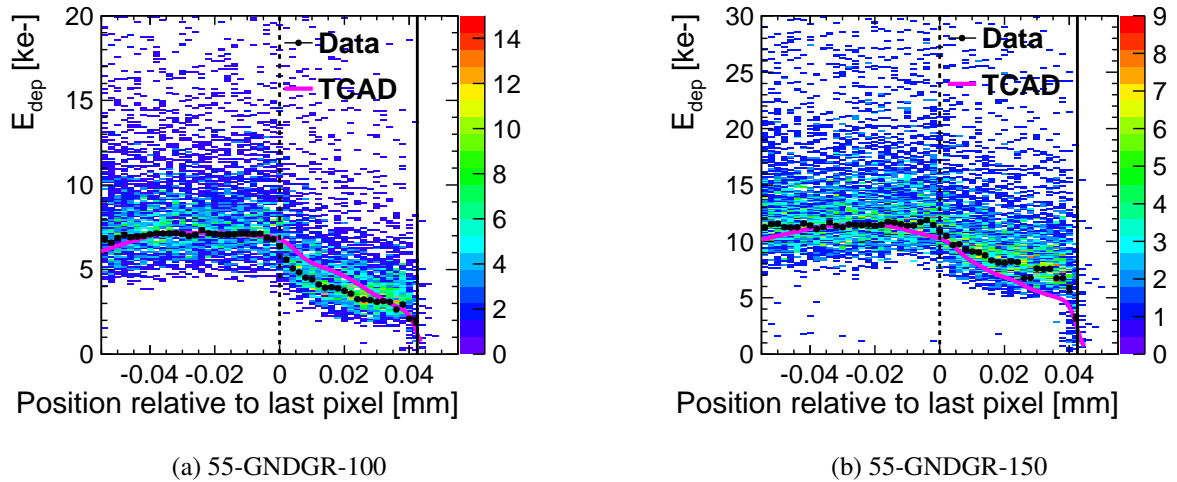


Figure 8.16: Charge collected as a function of the track position at the edge for the assemblies (a) 55-GNDGR-100 and (b) 55-GNDGR-150 in data and TCAD simulations. In data, only tracks within the central 40% of the pixel cell area are considered.

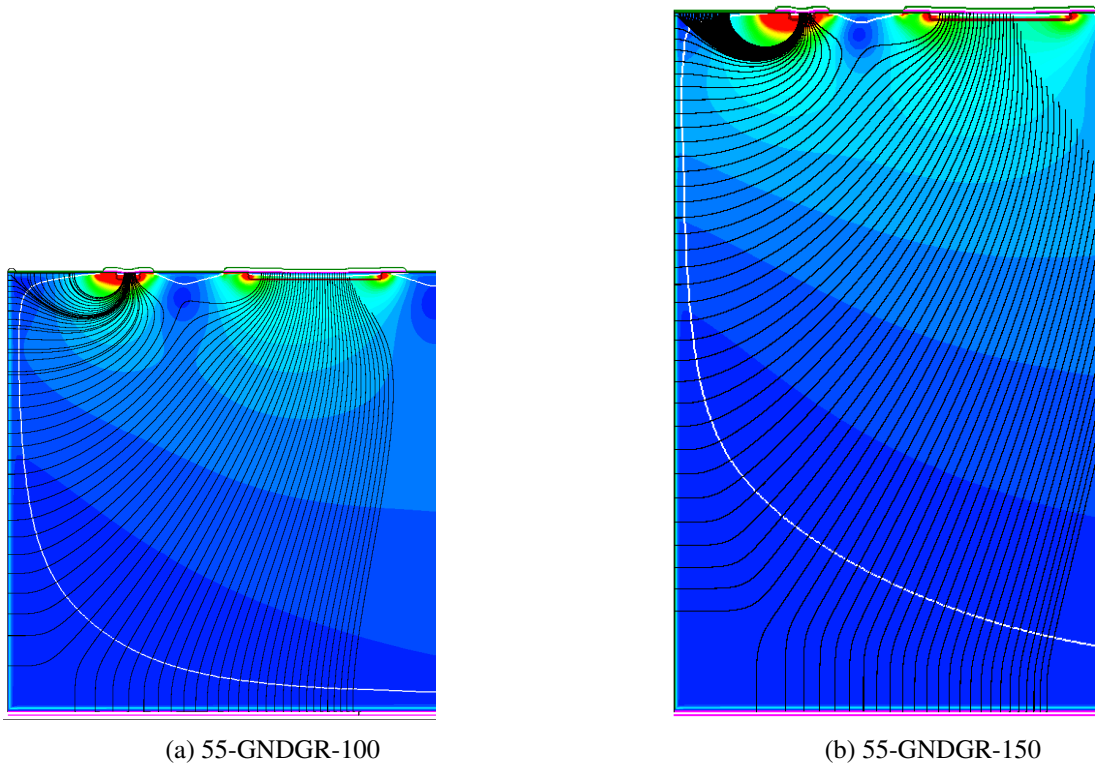


Figure 8.17: The electric field and the streamlines distributions for different configurations of guard ring for 100  $\mu\text{m}$  and 150  $\mu\text{m}$  thick sensors. The generated charges follow the streamlines. The depletion region is indicated by solid white lines.

## 8.4 Summary

Figure 8.18 summarises the edge efficiency as a function of the track position relative to the last pixel projected in one direction for the different assemblies.

For thin sensors (50  $\mu\text{m}$  thick), the grounded guard ring is not a suitable solution since the guard ring collects most of the charge in the edge and therefore lowers the efficiency. A floating guard ring appears to be the most suitable solution, as it shows a high detection efficiency at the edge and an acceptable breakdown behaviour.

For thicker sensors (100  $\mu\text{m}$  and 150  $\mu\text{m}$ ), the grounded guard ring is a suitable solution as a larger amount of charge is deposited by the passage of MIP particles. Some of the deposited charge is collected by the guard ring but these assemblies remain efficient up to the physical edge.

The TCAD simulation model developed in this thesis for active edge sensors is a powerful tool which allows to understand better the functionality of these sensors. The simulations fulfill the expectations for the operation of these devices: the floating guard ring has the highest breakdown voltage since the guard ring smoothes the potential drop between the physical edge and the first pixel. However, for reproducing a simulation which would exactly describe the loss of charge at the edge for a floating guard ring, the capacitive coupling of the guard ring to all  $\sim 1000$  edge pixels has to be taken into account.

In general, a good agreement between data and TCAD simulations is observed. The discrepancies observed can be explained by the effects not modeled in the simulations. The doping profiles used by the manufacturer are not known for the TCAD simulations. This might affect the electric field distribution inside the sensors. The depletion region in simulations can therefore be slightly different

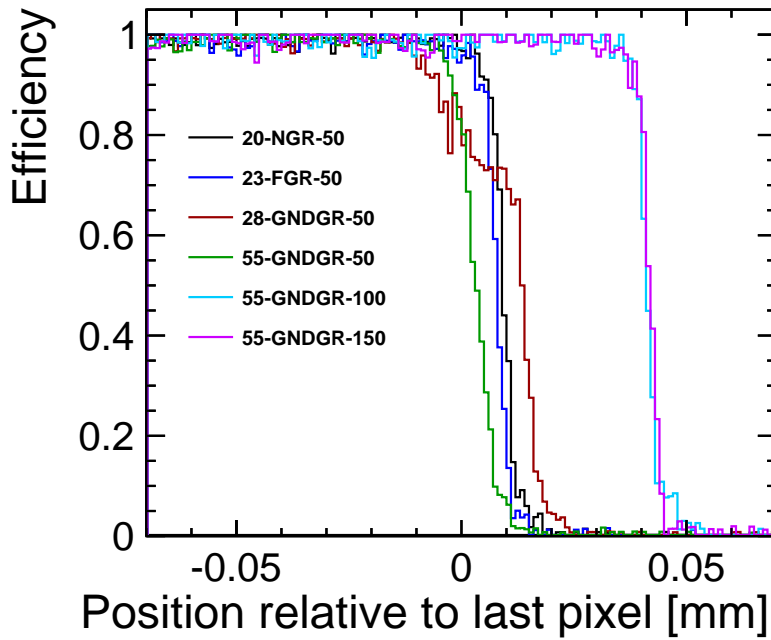


Figure 8.18: The edge efficiency in data as a function of the track position relative to the edge projected in one direction.

than in reality and therefore affecting the collected charge at the edge. The energy loss fluctuations are also not considered in the simulations. In addition, the Timepix3 chip has a non-linear behaviour for low energy depositions. Therefore the quality of the calibration also has an impact on the agreement between data and simulations especially for low-energy depositions. Finally, the TCAD model is only implemented in 2D and the coupling to other pixels and the sensor edge is not fully simulated. A 3D simulation could help with a more precise modeling of the capacitive coupling between the guard ring and the neighbouring pixels.



# CHAPTER 9

---

## Conclusions

---

The vertex detector plays a key role to fully exploit the physics potential at CLIC. To meet the challenging demands on the precision physics, pixel detectors with high spatial resolution of  $\sim 3 \mu\text{m}$  and low material content of  $\sim 0.2\% X_0$  per vertex layer are required. Full detector simulations have shown that the material budget of the detector must be as low as possible to achieve a high flavour-tagging performance. To attain both requirements on the resolution and the material content, hybrid pixel-detector solutions with  $50 \mu\text{m}$  thick sensors coupled to  $50 \mu\text{m}$  thick readout ASICs and  $25 \mu\text{m}$  pixel pitch are foreseen.

In the scope of this thesis, the prospects of planar silicon pixel sensors to meet the challenging requirements in the vertex detector in terms of spatial resolution and material budget have been assessed. Thin active-edge sensors with thicknesses varying between  $50 \mu\text{m}$  to  $150 \mu\text{m}$  have been studied in test-beam and laboratory measurements. All studies were accompanied by simulations.

The high-performance Timepix3 pixel readout ASIC, with  $55 \mu\text{m}$  pitch, was chosen as a test vehicle for the characterisation of the sensors. With its low noise at the front-end of  $\sim 80$  electrons, it allowed for operating the chip at low thresholds of  $\sim 500$  electrons. It provided an accurate test-pulse injection functionality that was used for the energy calibration of the chip and thereby for an absolute measurement of the energy deposited in the thin sensors.

First, the spatial resolution achievable with thin sensors was investigated. The devices under test (DUTs) were measured in a Timepix3-based beam telescope during test-beam campaigns at the CERN SPS. All of the assemblies have shown an excellent detection efficiency. In general, a more precise reconstruction of the track's passing point was possible for multi-pixel clusters by weighting the energy deposits in the involved pixels. The  $\eta$ -algorithm has given better results by taking into account the non-linearities due to the charge sharing. The results however have shown that the amount of charge sharing in such thin sensors is very low, limiting the achievable resolution.

For a deeper understanding of the test-beam results, the telescope setup with the DUTs has been implemented in the GEANT4-based simulation framework, AllPix. A digitiser, describing the charge transport in planar silicon sensors, has been developed. The tracking resolution of the telescope on the DUT of  $\sim 2 \mu\text{m}$  has been extracted from the simulation and validated by comparing the observed residuals on the telescope planes with the corresponding simulation results. The validated simulation framework has then been used to simulate the different assemblies with different thicknesses. A good agreement between data and simulation was seen for cluster-size distribution, the position resolution and the energy deposition spectrum. The charge sharing model as described in the digitiser of the simulations has been validated with data. The GEANT4 PAI physics list to simulate the energy deposition in thin sensors, which provides a similar spectrum as the Bichsel model, was in agreement with the data. From the agreement between the energy deposition in data and simulation it was concluded that the test-pulse

calibration provided enough precision for tracking purposes.

For the CLIC vertex detector, a hit resolution of  $\sim 3 \mu\text{m}$  is wished to be achieved with pixels of  $25 \mu\text{m}$  pitch and a sensor thickness of  $50 \mu\text{m}$ . Since data were not available for such a configuration, the simulations were extrapolated to small pixels. In the future, these results could be used as input for the digitiser in full detector simulations. The results have shown that achieving high resolution with such thin sensors is very challenging. New detector concepts with enhanced charge sharing or even smaller pixel pitch will therefore be required.

Finally, the efficiency of active-edge sensors were studied. Assemblies with different edge widths and guard ring configurations were investigated in test-beam. A two-dimensional TCAD simulation of the edge was implemented which allowed for a better understanding of the fabrication process and the operation of such devices.

At the nominal operating conditions, none of the assemblies were operated beyond the breakdown voltage. Most of the assemblies were found to be efficient up to the physical edge of the sensor. For thin sensors of  $50 \mu\text{m}$ , the configurations without guard ring or with floating guard ring were the most suitable designs. A grounded guard ring was disfavoured due to the loss of efficiency close to the edge for thin sensors. However, for thicker sensors of  $100 \mu\text{m}$  and  $150 \mu\text{m}$ , the grounded guard ring was showing high efficiencies up to the sensor trench due to the thicker silicon bulk.

The two-dimensional TCAD simulations have shown a good description of the trends and were in agreement with data. The remaining discrepancies in terms of breakdown behaviour and the charge collected at the edge between simulations and data are attributed to the simplifications due to the two-dimensional simulations.

# Bibliography

---

- [1] M. Aicheler et al.,  
*A Multi-TeV Linear Collider Based on CLIC Technology: CLIC Conceptual Design Report*, CERN-2012-007. SLAC-R-985. KEK-Report-2012-1. PSI-12-01. JAI-2012-001 (2012) (cit. on pp. 1, 3).
- [2] L. Linssen et al., *Physics and Detectors at CLIC: CLIC Conceptual Design Report*, arXiv:1202.5940. CERN-2012-003. ANL-HEP-TR-12-01. DESY-12-008. KEK-Report-2011-7 (2012) (cit. on pp. 1, 3–5, 9).
- [3] T. Poikela et al.,  
*Timepix3: a 65K channel hybrid pixel readout chip with simultaneous ToA/ToT and sparse readout*, *Journal of Instrumentation* **9**.05 (2014) C05013 (cit. on pp. 1, 35, 37, 38, 42, 56).
- [4] S. Agostinelli et al., *GEANT4: A Simulation toolkit*, *Nucl. Instrum. Meth.* **A506** (2003) 250 (cit. on pp. 1, 11, 45).
- [5] M. Bicer et al., *First Look at the Physics Case of TLEP*, *JHEP* **01** (2014) 164, arXiv: [1308.6176 \[hep-ex\]](https://arxiv.org/abs/1308.6176) (cit. on p. 3).
- [6] S. L. Glashow, *Partial Symmetries of Weak Interactions*, *Nucl. Phys.* **22** (1961) 579 (cit. on p. 3).
- [7] S. Weinberg, *A Model of Leptons*, *Phys. Rev. Lett.* **19** (1967) 1264 (cit. on p. 3).
- [8] A. Salam, “Weak and Electromagnetic Interactions”, *Elementary particle theory, Relativistic groups and analyticity*, Proceedings of the Eighth Nobel Symposium, (Aspenäsgården, Lerum, 19th–25th May 1968), ed. by N. Svartholm, Stockholm: Almqvist & Wiksell, 1968 367 (cit. on p. 3).
- [9] G. ’t Hooft and M. J. G. Veltman, *Regularization and Renormalization of Gauge Fields*, *Nucl. Phys.* **B44** (1972) 189 (cit. on p. 3).
- [10] M. Thomson, *Modern particle physics*, Cambridge: Cambridge University Press, 2013, URL: <http://cds.cern.ch/record/1529540> (cit. on p. 3).
- [11] *Standard Model*, Website: [http://en.wikipedia.org/wiki/File:Standard\\_Model\\_of\\_Elementary\\_Particles.svg](http://en.wikipedia.org/wiki/File:Standard_Model_of_Elementary_Particles.svg) (cit. on p. 4).
- [12] G. Aad et al., *Observation of a new particle in the search for the Standard Model Higgs boson with the ATLAS detector at the LHC*, *Physics Letters B* **716.1** (2012) 1, ISSN: 0370-2693, URL: [//www.sciencedirect.com/science/article/pii/S037026931200857X](http://www.sciencedirect.com/science/article/pii/S037026931200857X) (cit. on p. 4).
- [13] S. Chatrchyan et al.,  
*Observation of a new boson at a mass of 125 GeV with the CMS experiment at the LHC*, *Physics Letters B* **716.1** (2012) 30, ISSN: 0370-2693, URL: [//www.sciencedirect.com/science/article/pii/S0370269312008581](http://www.sciencedirect.com/science/article/pii/S0370269312008581) (cit. on p. 4).

- [14] M. J. Boland et al., *Updated baseline for a staged Compact Linear Collider* (2016), ed. by P. Lebrun et al., arXiv: [1608.07537 \[physics.acc-ph\]](https://arxiv.org/abs/1608.07537) (cit. on pp. 5–7).
- [15] H. Abramowicz et al., *Higgs Physics at the CLIC Electron-Positron Linear Collider* (2016), arXiv: [1608.07538 \[hep-ex\]](https://arxiv.org/abs/1608.07538) (cit. on p. 5).
- [16] D. Dannheim and A. Sailer, *Beam-Induced Backgrounds in the CLIC Detectors*, LCD-Note-2011-021 (Apr. 2012), URL: <https://cds.cern.ch/record/1443516> (cit. on pp. 8–10).
- [17] H. Abramowicz et al., *Forward Instrumentation for ILC Detectors*, *JINST* **5** (2010) P12002, arXiv: [1009.2433 \[physics.ins-det\]](https://arxiv.org/abs/1009.2433) (cit. on p. 8).
- [18] H. Abramowicz et al., *Instrumentation of the very forward region of a linear collider detector*, *IEEE Trans. Nucl. Sci.* **51** (2004) 2983 (cit. on p. 8).
- [19] *CLIC detector model*, URL: <http://clicdp.web.cern.ch/content/clic-detector> (cit. on p. 9).
- [20] N. Alipour Tehrani and P. Roloff, *Optimisation Studies for the CLIC Vertex-Detector Geometry*, CLICdp-Note-2014-002 (July 2014), URL: [http://cds.cern.ch/record/1742993](https://cds.cern.ch/record/1742993) (cit. on pp. 10, 12).
- [21] N. A. Tehrani, *Optimisation studies for the CLIC vertex-detector geometry*, *JINST* **10.07** (2015) C07001 (cit. on pp. 10, 11, 13).
- [22] *LCFIPlus*, URL: <https://confluence.slac.stanford.edu/display/ilc/LCFIPlus> (cit. on p. 10).
- [23] F. Duarte Ramos, H. Gerwig and M. Villarejo Bermudez, *CLIC inner detectors cooling simulations*, LCD-Note-2013-007 (Jan. 2014), URL: [http://cds.cern.ch/record/1572989](https://cds.cern.ch/record/1572989) (cit. on p. 11).
- [24] H. Spieler, *Semiconductor Detector Systems*, Semiconductor Science and Technology, Oxford: Oxford Univ. Press, 2005 (cit. on pp. 16, 17, 22, 27–29).
- [25] J. Beringer et al., *Review of Particle Physics (RPP)*, *Phys. Rev.* **D86** (2012) 010001 (cit. on pp. 18, 19).
- [26] L. Landau, *On the energy loss of fast particles by ionization*, *J. Phys.(USSR)* **8** (1944) 201 (cit. on p. 19).
- [27] P. V. Vavilov, *Ionization losses of high-energy heavy particles*, *Sov. Phys. JETP* **5** (1957) 749 (cit. on p. 19).
- [28] H. Bichsel, *Straggling in Thin Silicon Detectors*, *Rev. Mod. Phys.* **60** (1988) 663 (cit. on pp. 19, 20).
- [29] G. R. Lynch and O. I. Dahl, *Approximations to multiple Coulomb scattering*, *Nucl. Instrum. Meth.* **B58** (1991) 6 (cit. on p. 20).
- [30] L. Rossi et al., *Pixel detectors: from fundamentals to applications*, Particle Acceleration and Detection, Berlin: Springer, 2006, URL: [http://cds.cern.ch/record/976471](https://cds.cern.ch/record/976471) (cit. on pp. 21, 22, 30).
- [31] C. Jacoboni et al., *A review of some charge transport properties of silicon*, *Solid-State Electronics* **20.2** (1977) 77, ISSN: 0038-1101, URL: <http://www.sciencedirect.com/science/article/pii/0038110177900545> (cit. on p. 21).

- [32] G. F. Knoll, *Radiation Detection and Measurement*; 4th ed. New York, NY: Wiley, 2010 (cit. on p. 23).
- [33] S. Gadomski, *Model of the SCT detectors and electronics for the ATLAS simulation using Geant4* (2001), URL: <http://cds.cern.ch/record/684197> (cit. on p. 26).
- [34] S. Ramo, *Currents induced by electron motion*, Proc. Ire. **27** (1939) 584 (cit. on p. 28).
- [35] *Synopsys TCAD*, URL: <http://www.synopsys.com/tools/tcad/Pages/default.aspx> (cit. on pp. 29, 49).
- [36] E. Belau et al., *The Charge Collection in Silicon Strip Detectors*, Nucl. Instrum. Meth. **214** (1983) 253 (cit. on pp. 32, 33, 52, 58).
- [37] R. Turchetta, *Spatial resolution of silicon microstrip detectors*, Nucl. Instrum. Meth. **A335** (1993) 44 (cit. on p. 32).
- [38] N. Alipour Tehrani et al., *Test beam analysis of ultra-thin hybrid pixel detector assemblies with Timepix readout ASICs*, CLICdp-Note-2016-001 (Feb. 2016), URL: <http://cds.cern.ch/record/2133128> (cit. on pp. 33, 52).
- [39] X. Llopart et al., *Timepix, a 65k programmable pixel readout chip for arrival time, energy and/or photon counting measurements*, Nucl. Instrum. Meth. **A581** (2007) 485 (cit. on p. 35).
- [40] *Medipix Collaboration*, URL: <http://medipix.web.cern.ch/medipix/> (cit. on p. 35).
- [41] F. Krummenacher, *Pixel detectors with local intelligence: an IC designer point of view*, Nuclear Instruments and Methods in Physics Research Section A: Accelerators, Spectrometers, Detectors and Associated Equipment **305.3** (1991) 527, ISSN: 0168-9002, URL: <http://www.sciencedirect.com/science/article/pii/016890029190152G> (cit. on p. 35).
- [42] J. Visser et al., *SPIDR: a read-out system for Medipix3 & Timepix3*, JINST **10.12** (2015) C12028 (cit. on p. 37).
- [43] *Xilinx Virtex-7 FPGA Family*, URL: <http://www.xilinx.com/products/silicon-devices/fpga/virtex-7.html> (cit. on p. 37).
- [44] X. Wu et al., *Recent advances in processing and characterization of edgeless detectors*, Journal of Instrumentation **7.02** (2012) C02001 (cit. on pp. 38, 77, 79).
- [45] N. Alipour Tehrani et al., *Calibration of ultra-thin hybrid pixel detector assemblies with Timepix readout ASICs*, CLICdp-Note-2015-003 (Sept. 2015), URL: <http://cds.cern.ch/record/2054922> (cit. on p. 40).
- [46] X. Llopart Cudie, Medipix Collaboration private communication, 2016 (cit. on p. 41).
- [47] J. Jakubek et al., *Pixel detectors for imaging with heavy charged particles*, Nuclear Instruments and Methods in Physics Research Section A: Accelerators, Spectrometers, Detectors and Associated Equipment **591.1** (2008) 155, Radiation Imaging Detectors 2007 Proceedings of the 9th International Workshop on Radiation Imaging Detectors, ISSN: 0168-9002, URL: <http://www.sciencedirect.com/science/article/pii/S0168900208004245> (cit. on p. 43).

## Bibliography

---

- [48] J. Apostolakis et al.,  
*Geometry and physics of the Geant4 toolkit for high and medium energy applications*,  
Radiation Physics and Chemistry **78**.10 (2009) 859, Workshop on Use of Monte Carlo Techniques  
for Design and Analysis of Radiation Detectors, ISSN: 0969-806X,  
URL: <http://www.sciencedirect.com/science/article/pii/S0969806X09001650>  
(cit. on p. 45).
- [49] J. Apostolakis et al., *An implementation of ionisation energy loss in very thin absorbers for the GEANT4 simulation package*, Nucl. Instrum. Meth. **A453** (2000) 597 (cit. on p. 45).
- [50] M. Benoit and A. Lounis, *Étude des détecteurs planaires pixels durcis aux radiations pour la mise à jour du détecteur de vertex d'ATLAS*, presented 10 Jun 2011,  
PhD thesis: U. Paris-Sud 11, Dept. Phys., Orsay, 2011,  
URL: <http://cds.cern.ch/record/1474878> (cit. on p. 46).
- [51] AllPix, URL: <https://github.com/ALLPix/allpix> (cit. on p. 46).
- [52] AllPix TWiki, URL: <https://twiki.cern.ch/twiki/bin/view/Main/AllPix> (cit. on p. 46).
- [53] Open Inventor Website, URL: <http://www.openinventor.com> (cit. on p. 47).
- [54] I. Rubinskiy, *EUTelescope. Offline track reconstruction and DUT analysis software.*,  
EUDET-Memo-2010-12 (Dec. 2010),  
URL: <http://www.euDET.org/e26/e28/e86887/e107460/EUDET-Memo-2010-12.pdf>  
(cit. on p. 50).
- [55] EUTelescope Software Developers Website, URL: <http://eutelescope.web.cern.ch/>  
(cit. on p. 50).
- [56] pyEudetAnalysis, URL: <https://github.com/pyEudetAnalysis/pyEudetAnalysis>  
(cit. on pp. 50, 52).
- [57] S. J. Aplin, J. Engels and F. Gaede, *A production system for massive data processing in ILCSoft* (2009) (cit. on p. 50).
- [58] F. Gaede, *Marlin and LCCD: Software tools for the ILC*, Nucl. Instrum. Meth. **A559** (2006),  
Proceedings of the 10th International Workshop on Advanced computing and analysis techniques  
in physics research, ACAT05, Zeuthen, Germany, May 22-27, 2005 (cit. on p. 50).
- [59] I. Rubinskiy and H. Perrey, *An EUDET/AIDA Pixel Beam Telescope for Detector Development*,  
PoS **TIPP2014** (2014) 122 (cit. on p. 50).
- [60] Jansen, Hendrik et al., *Performance of the EUDET-type beam telescopes*,  
EPJ Techn Instrum **3**.1 (2016) 7,  
URL: <http://dx.doi.org/10.1140/epjti/s40485-016-0033-2> (cit. on pp. 51, 61).
- [61] V. Blobel, *Software alignment for tracking detectors*,  
Nuclear Instruments and Methods in Physics Research Section A: Accelerators, Spectrometers,  
Detectors and Associated Equipment **566**.1 (2006) 5, ISSN: 0168-9002,  
URL: <http://www.sciencedirect.com/science/article/pii/S0168900206007984>  
(cit. on p. 52).
- [62] A. F. Zarnecki and P. Nizurawski, *EUDET Telescope Geometry and Resolution Studies* (2007),  
arXiv: [physics/0703058 \[PHYSICS\]](https://arxiv.org/abs/physics/0703058) (cit. on pp. 52, 55).

- [63] R. Brun and F. Rademakers, *ROOT — An object oriented data analysis framework*, Nuclear Instruments and Methods in Physics Research Section A: Accelerators, Spectrometers, Detectors and Associated Equipment **389**.1 (1997) 81, ISSN: 0168-9002, URL: <http://www.sciencedirect.com/science/article/pii/S016890029700048X> (cit. on p. 52).
- [64] *SciPy hierarchical fclusterdata*, URL: <http://docs.scipy.org/doc/scipy/%20reference/generated/scipy.cluster.hierarchy.fclusterdata.html> (cit. on p. 52).
- [65] *SciPy optimize minimize*, URL: <http://docs.scipy.org/doc/scipy/reference/generated/scipy.optimize.minimize.html> (cit. on p. 53).
- [66] *CERN SPS*, URL: <http://sba.web.cern.ch/sba/> (cit. on p. 55).
- [67] *H6 beam line*, URL: <http://sba.web.cern.ch/sba/BeamsAndAreas/resultbeam.asp?beamline=H6> (cit. on p. 55).
- [68] *Online tool for optimising the placement of the telescope planes*, URL: <http://skulis.web.cern.ch/skulis/telescope/> (cit. on p. 55).
- [69] K. Akiba et al., *The Timepix Telescope for High Performance Particle Tracking*, Nucl. Instrum. Meth. **A723** (2013) 47, arXiv: 1304.5175 [physics.ins-det] (cit. on p. 56).
- [70] K. Cranmer et al., *HistFactory: A tool for creating statistical models for use with RooFit and RooStats* (2012) (cit. on p. 67).
- [71] P. Valerio, R. Ballabriga and M. Campbell, *Design of the 65 nm CLICpix demonstrator chip*, LCD-Note-2012-018 (Nov. 2012), URL: <https://cds.cern.ch/record/1507691> (cit. on p. 73).
- [72] A. Tomada and C. Kenney, SLAC private communication, 2015 (cit. on p. 73).
- [73] N. A. Tehrani, *Recent results with HV-CMOS and planar sensors for the CLIC vertex detector*, Nuclear Instruments and Methods in Physics Research Section A: Accelerators, Spectrometers, Detectors and Associated Equipment (2016) , ISSN: 0168-9002, URL: <http://www.sciencedirect.com/science/article/pii/S0168900216305393> (cit. on p. 73).
- [74] H. Jansen, *A Pascalian lateral drift sensor*, Nuclear Instruments and Methods in Physics Research Section A: Accelerators, Spectrometers, Detectors and Associated Equipment **831** (2016) 242, Proceedings of the 10th International “Hiroshima” Symposium on the Development and Application of Semiconductor Tracking Detectors, ISSN: 0168-9002, URL: <http://www.sciencedirect.com/science/article/pii/S016890021600142X> (cit. on p. 74).
- [75] Y. Arai et al., *Development of SOI pixel process technology*, Nucl. Instrum. Meth. **A636**.1 (2011) S31 (cit. on p. 74).
- [76] *Advacam sensor wafer fabrication*, URL: <http://www.advacam.com/en/services/sensor-wafer-fabrication> (cit. on p. 78).
- [77] S. M. Sze, *Physics of semiconductor devices*; 2nd ed. New York, NY: Wiley, 1981 (cit. on p. 83).



# **Appendix**



## APPENDIX A

---

### Pixel readout ASICs and assembly calibration

---

The threshold DAC value can be translated into an effective energy as described in Chapter 4. Figure A.1 shows the calibration for the assemblies listed in Table 4.2.

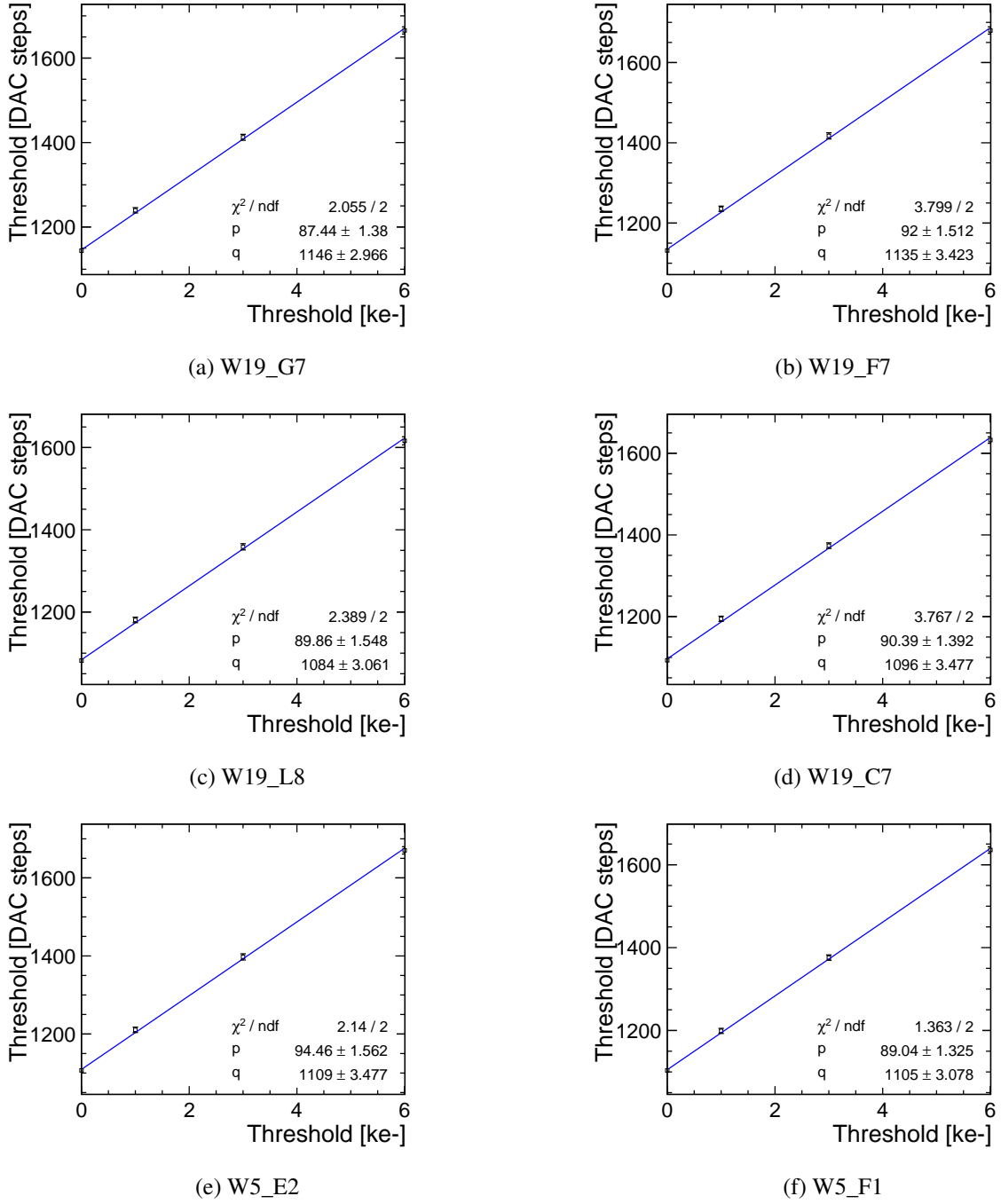


Figure A.1: Threshold calibration for the assemblies listed in Table 4.2. Each point corresponds to the maximum gradient of the S-curve for each pulse height. A linear function as described in Equation (4.3) was used to fit the data points and obtain the parameters  $p$  and  $q$ .

## APPENDIX B

---

### Telescope

---

Biased residual distributions for the different telescope planes are shown here. The biased residual on each telescope plane is defined as the difference between the measured hit and the fitted track position. A cut is applied to discard the tracks with  $\chi^2/\text{NDF}$  higher than 100.

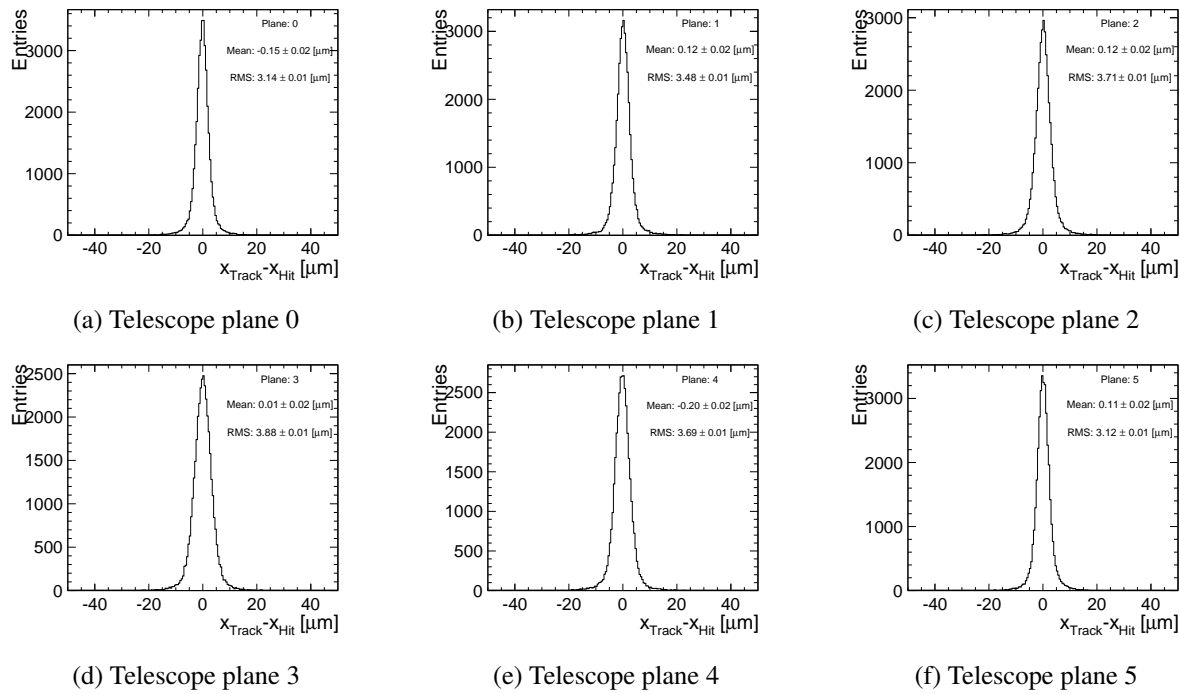


Figure B.1: Biased residual distribution in x-direction obtained in data for each telescope plane. The RMS of the residual is also shown.

## Appendix B Telescope

---

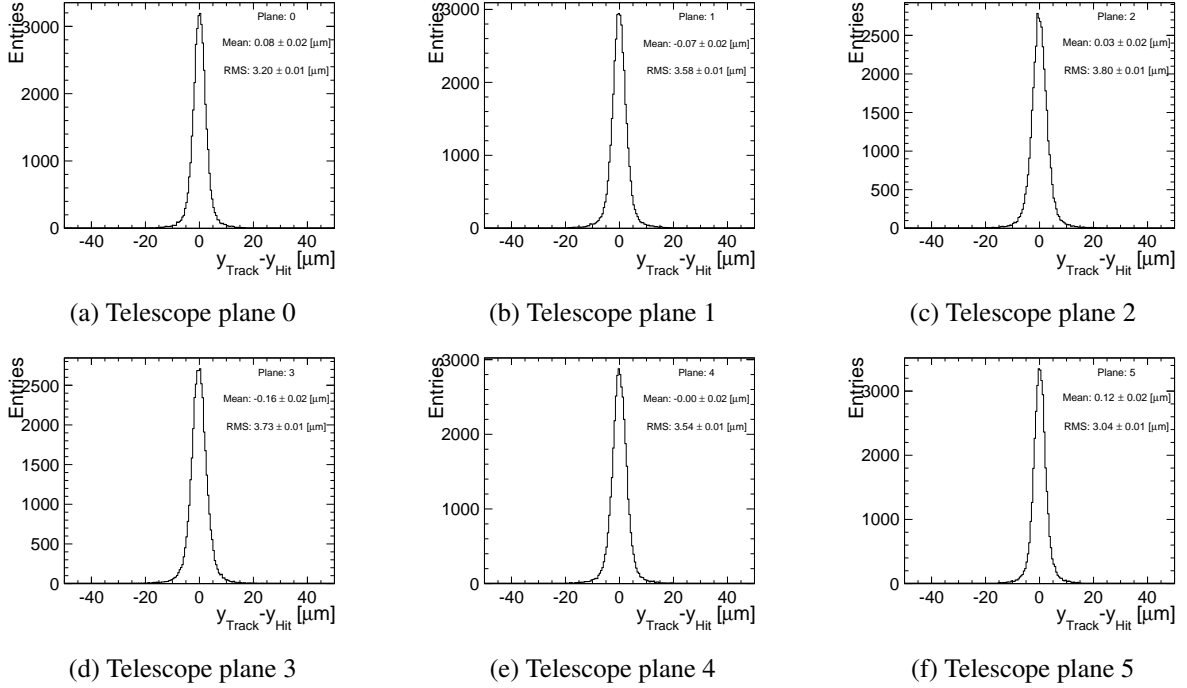


Figure B.2: Biased residual distribution in y-direction obtained in data for each telescope plane. The RMS of the residual is also shown.

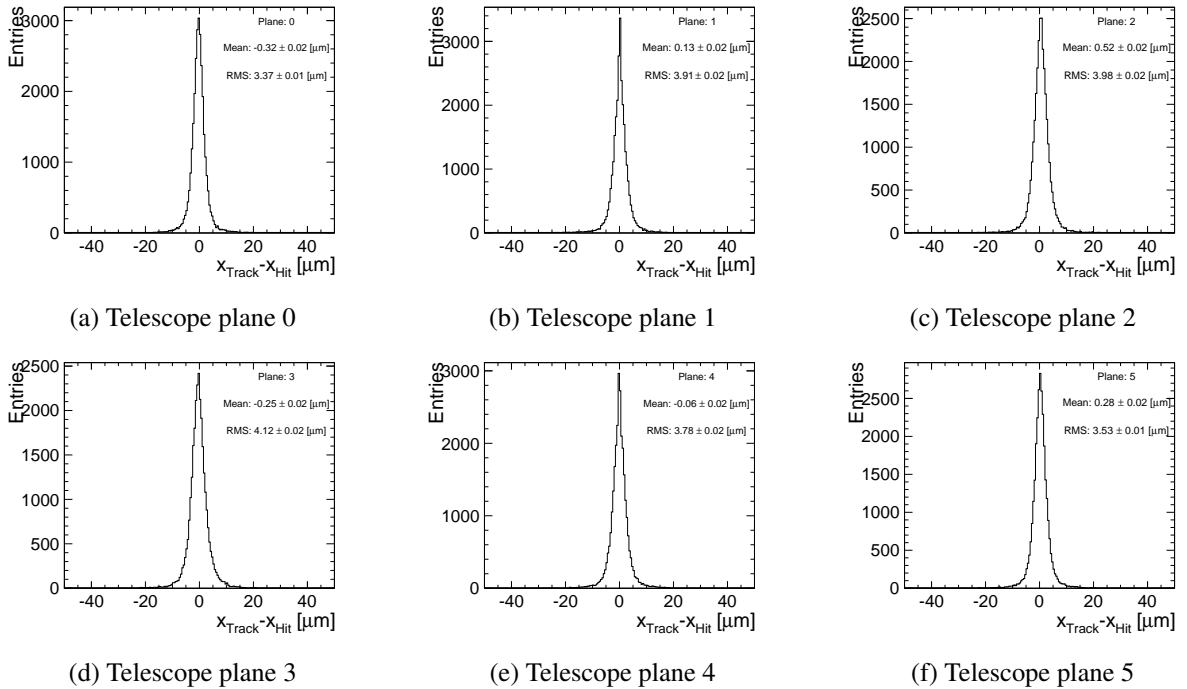


Figure B.3: Biased residual distribution in x-direction obtained in AllPix simulations for each telescope plane. The RMS of the residual is also shown.

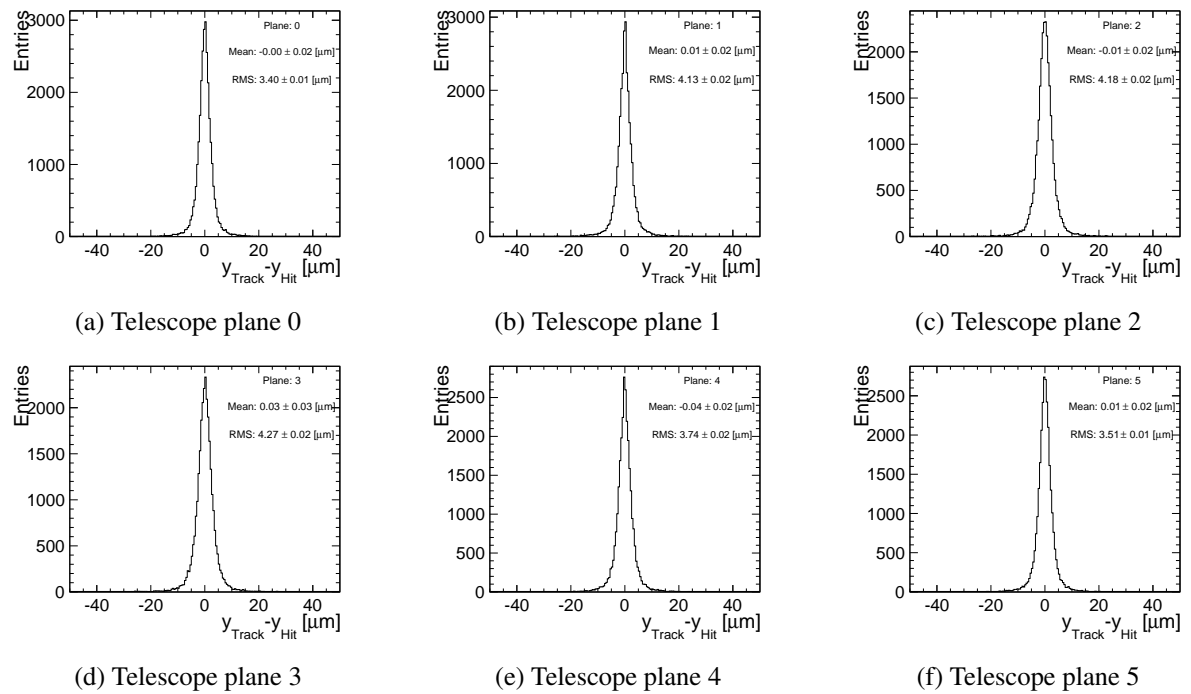
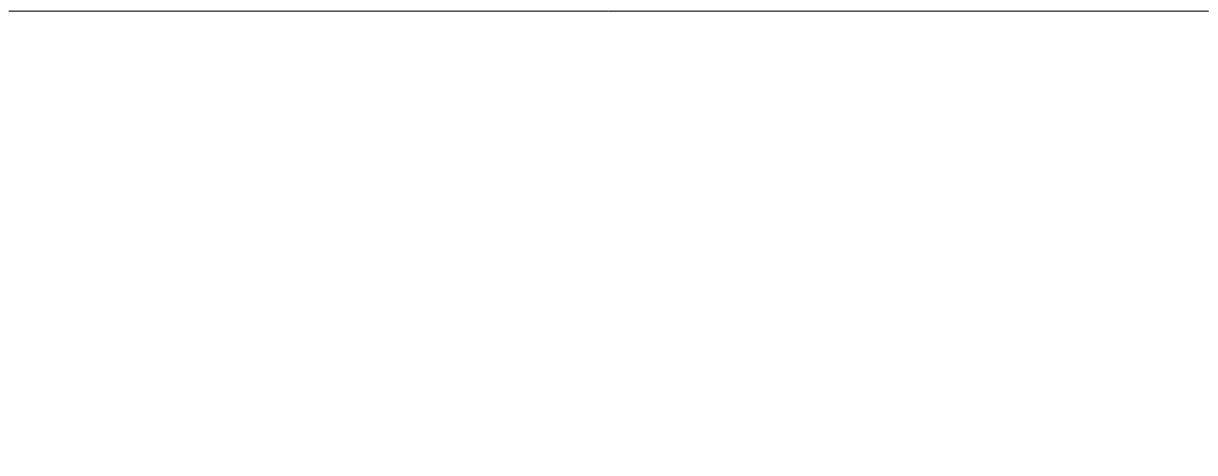


Figure B.4: Biased residual distribution in y-direction obtained in AllPix simulations for each telescope plane. The RMS of the residual is also shown.



# APPENDIX C

---

## Thin Sensors

---

### C.1 Depletion voltage

The measured depletion voltage for all assemblies listed in Table 7.1. Section 7.2.2 describes the method used for calculating the depletion.

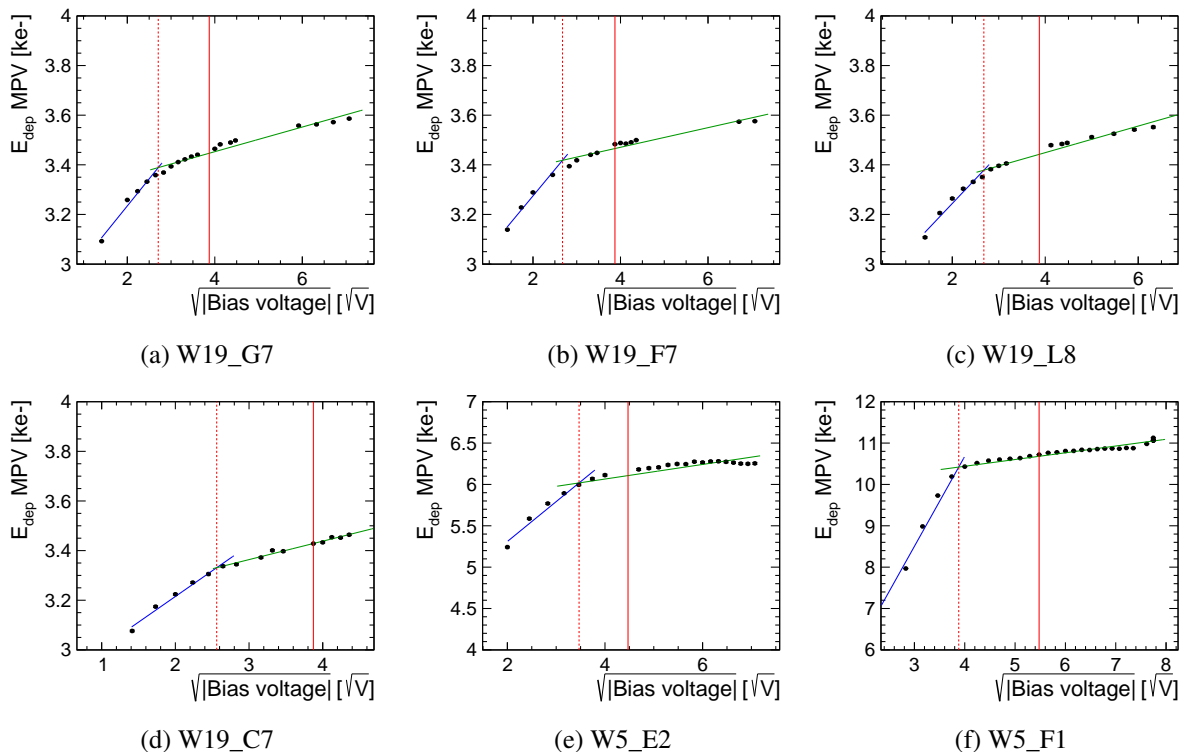


Figure C.1: The most probable value of the measured energy deposition as a function of the bias voltage for the assemblies listed in Table 7.1. Straight lines are used to fit the slope and the plateau regions. The depletion voltage corresponds to the intersection of these two regions and shown in a red dashed line. The continuous red line shows the nominal operating bias voltage.

## C.2 Cluster size distribution

The dependence of the cluster-size distribution on the bias voltage and the operating threshold is shown for the assemblies listed in Table 7.1.

### C.2.1 Cluster size distribution as a function of the bias voltage

For higher bias voltages, the average cluster size decreases as shown in Figure C.2.

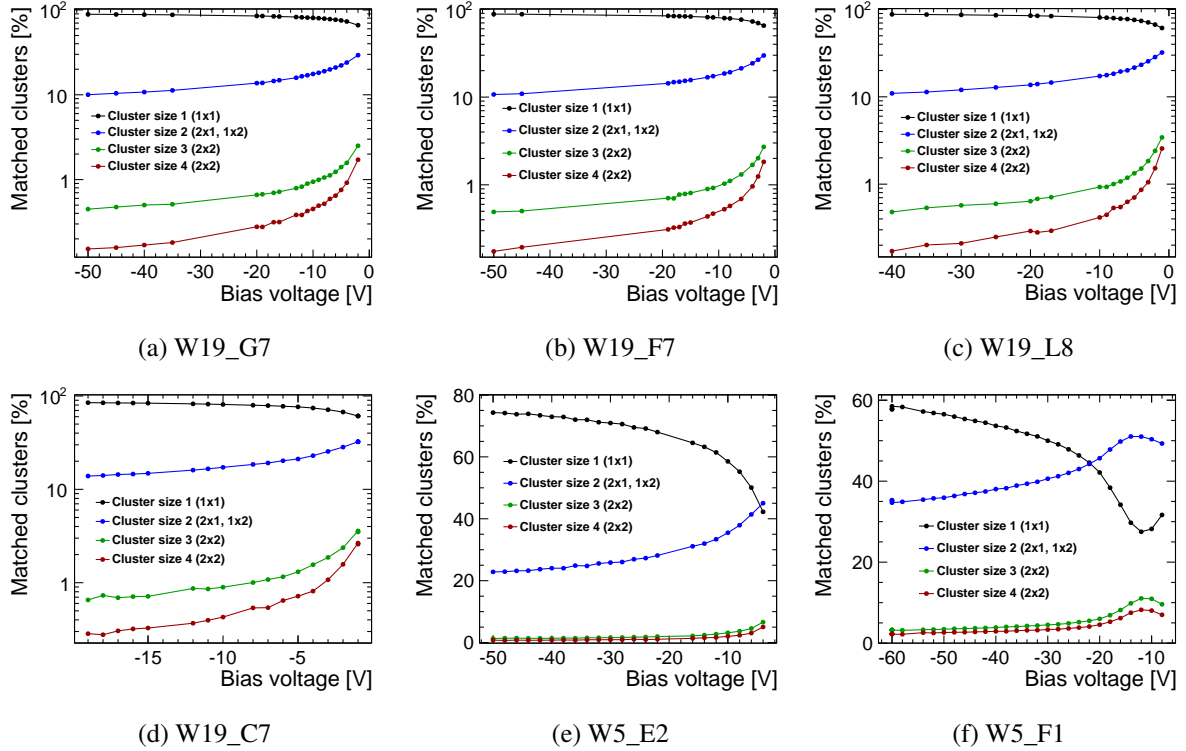


Figure C.2: Cluster size distribution as a function of the applied voltage for assemblies listed in Table 7.1.

### C.2.2 Cluster size distribution as a function of the operating threshold

Lowering the threshold leads to an increase in the average cluster size fraction distribution as shown in Figure C.3.

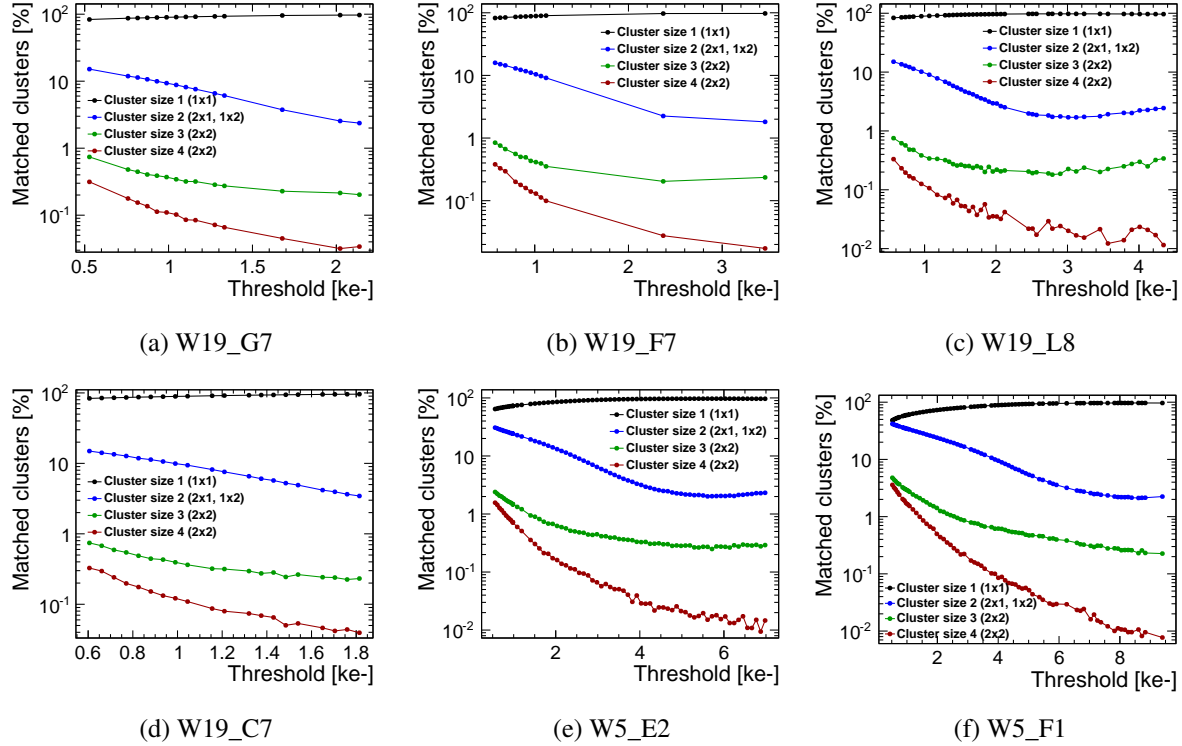


Figure C.3: Cluster sizes distribution as a function of the operating threshold for assemblies listed in Table 7.1.

### C.3 Charge sharing as a function of the track position

Figures C.4 to C.6 illustrate the track position within the pixel for 1 to 4-pixel cluster sizes for a 50 – 150  $\mu\text{m}$  sensors.

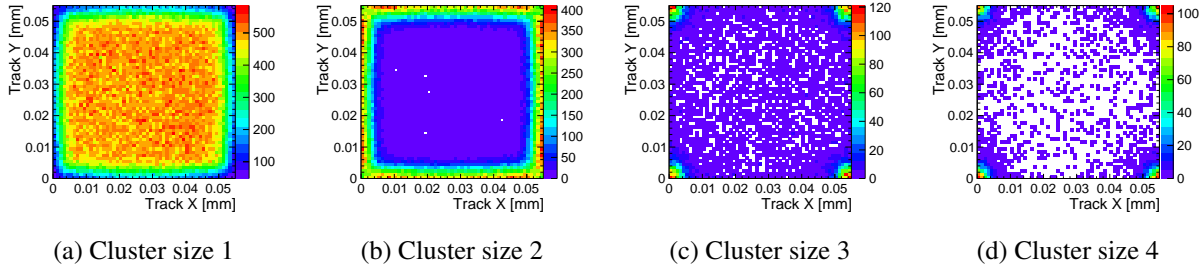


Figure C.4: Extrapolated track position within the pixel for 1 to 4-hit cluster sizes for a 50  $\mu\text{m}$  sensor (assembly W19\_G7). The assembly is operated at the nominal conditions.

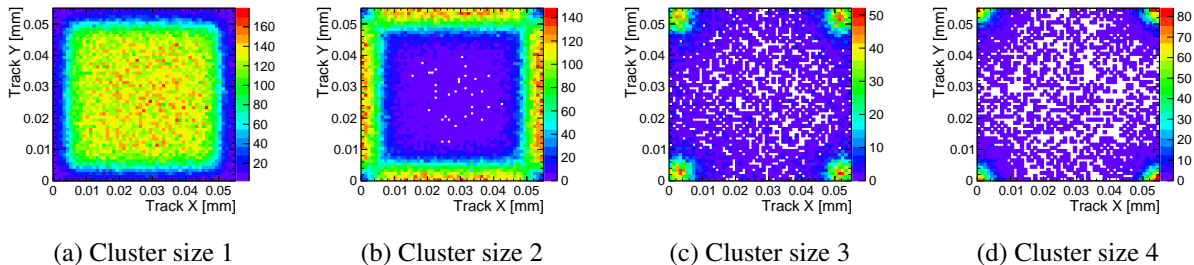


Figure C.5: Extrapolated track position within the pixel for 1 to 4-hit cluster sizes for a 100  $\mu\text{m}$  sensor (assembly W5\_E2). The assembly is operated at the nominal conditions.

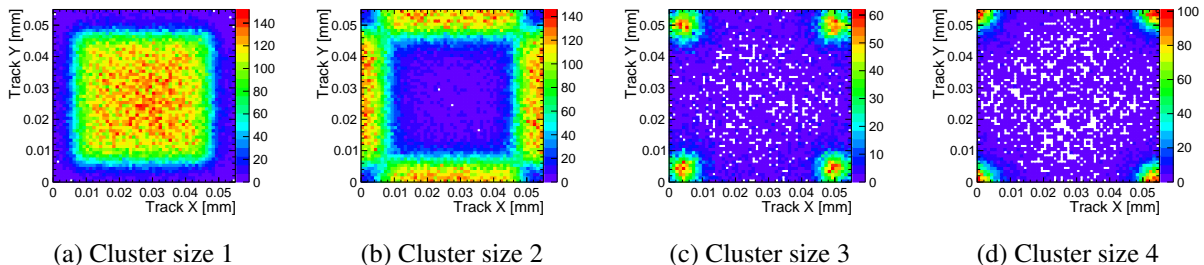


Figure C.6: Extrapolated track position within the pixel for 1 to 4-hit cluster sizes for a 150  $\mu\text{m}$  sensor (assembly W5\_F1). The assembly is operated at the nominal conditions.

## APPENDIX D

---

### Active edge sensors

---

TCAD simulation of active edge sensors using the process flow as described in Section 8.1.1. Figure D.1 shows the concentration of the dopants. The nominal bias voltage is also applied to the sensors and the region shown with a white line corresponds to the depletion region.

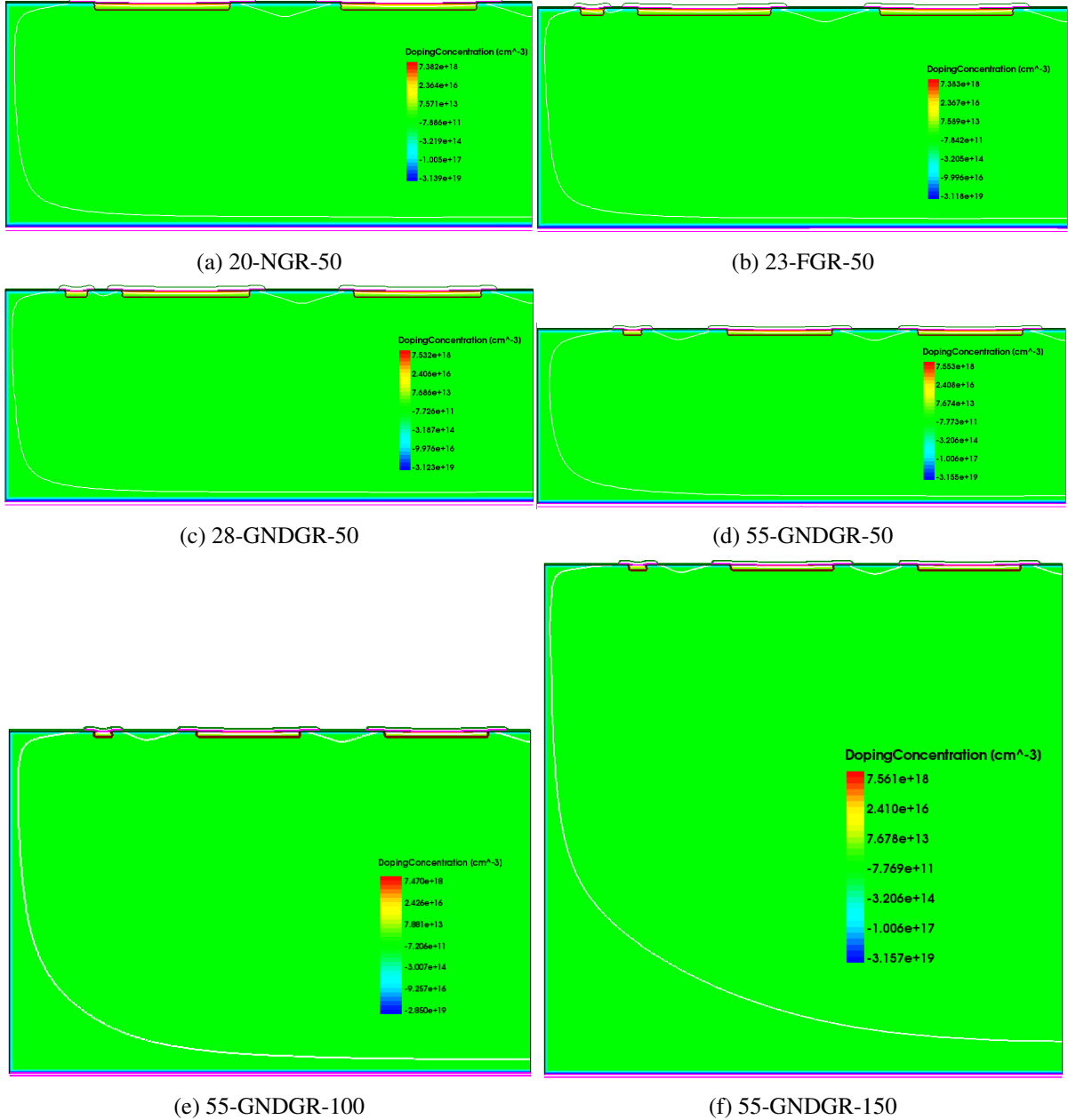


Figure D.1: Doping concentration in TCAD simulations for the assemblies listed in Table 8.1. The region shown with a white line is the depletion region.

# List of Figures

---

2.1	The building blocks of matter according to the Standard Model [11]. . . . .	4
2.2	The three implementation stages of CLIC near CERN with center-of-mass energies of 380 GeV, 1.5 TeV and 3 TeV [14]. . . . .	5
2.3	Standard Model Higgs boson production mechanisms at CLIC [2]. . . . .	5
2.4	Cross sections for the main Higgs production mechanisms for a $M_H = 126$ GeV Higgs boson as a function of the $e^+e^-$ center-of-mass energy in a lepton collider. These values correspond to unpolarised beams and the effect of beamstrahlung is not included [14]. .	6
2.5	Schematic layout of the CLIC accelerator complex at $\sqrt{s} = 3$ TeV. Each linac is fed by a drive-beam generation complex [14]. . . . .	7
2.6	Schematic layout of the CLIC detector concept [19]. . . . .	9
2.7	The schematic view of the disks geometry with 5 single-sided layers in the barrel region and 4 single-sided disks in the endcap region. . . . .	10
2.8	(a) Sketch showing the airflow cooling strategy within the vertex detector [23]. (b) Schematic view of the vertex detector for the <i>spirals</i> geometry. (c) Schematic view of the vertex detector for the <i>double_spirals_v2</i> . In the GEANT4 simulations [4], a double-sided layer is implemented as two silicon sensors on top of each other with an overall thickness of 2 mm. From [21]. . . . .	11
2.9	(a) b-tag and (b) c-tag efficiency for jets in dijet events at $\sqrt{s} = 200$ GeV with different polar angles for the <i>disks</i> geometry [20]. . . . .	12
2.10	Beauty-tagging performance for dijet events at 200 GeV. (a) Comparison between <i>disks</i> and <i>spirals</i> in terms of the ratio of the misidentification probabilities for charm background. (b) Comparison of the beauty-tagging performance between the <i>spirals</i> and <i>double_spirals</i> geometries. (c) Comparison of the beauty-tagging performance between the <i>double_spirals</i> and <i>double_spirals_v2</i> geometries. For (a) the misidentification ratio for each polar angle is shown separately. For (b) and (c), dijet events with a mixture of polar angles between 10° and 90° are considered. From [21]. . . . .	13
3.1	Illustration of the band structures for electron energies in insulators, semiconductors and metals. $E_F$ represents the Fermi energy level and $E_g$ the bandgap. . . . .	16
3.2	Lattice structure of silicon. The building block of the lattice is formed by a central atom bonded to four equidistant neighbours as shown in shaded gray. From [24]. . . . .	16
3.3	(a) Introducing a group five impurity, such as phosphorus, creates a lightly bound electron that can move under the influence of an electric field. (b) Introducing a group three impurity, such as boron, creates an unpaired silicon bond which can attract a neighbouring electron and results in a hole moving throughout the silicon lattice. From [24]. . . . .	17
3.4	Straggling function in silicon for 500 MeV pions, normalized to unity at the most probable value $\Delta_p$ . $w$ is the full-width-at-half-maximum [25]. This calculation is based on the Bichsel method (see Section 3.2.4). . . . .	19

3.5	Mobility for electrons and holes as a function of an applied electric field calculated with Equation (3.11). . . . .	22
3.6	Charge density distribution for a simplified pn-junction where $N_a$ and $N_d$ are the acceptor and the donor concentrations. . . . .	23
3.7	(a) Drift time and (b) diffusion standard deviation for n and p-type carriers for a charge created at the depth $z$ in the sensor. The diffusion is shown for different bias voltages and does not depend on the carrier type. The depletion voltage is $ V_D =4$ V and the drift time is calculated considering a bias voltage of $ V_B =15$ V. . . . .	26
3.8	The electric field and the mobility as a function of the depth for (a) n-type carriers and (b) p-type carriers. . . . .	27
3.9	Schematic layout of a hybrid pixel detector. A pixellated sensor is bump-bonded to a readout chip. Wire-bonds are used for external connections. From [24]. . . . .	27
3.10	The charge induced on two parallel plates for two configurations of the position of a charge $q$ . From [24]. . . . .	28
3.11	The weighting field and potential on electrode $k$ . . . . .	29
3.12	The hit probability density function for two neighbouring pixels (pixel 0 and pixel 1) when a binary readout is used to acquire the sensor pulse. . . . .	31
3.13	The hit probability density function for two neighbouring pixels (pixel 0 and pixel 1) considering charge sharing between the two pixels when a binary readout is used to acquire the sensor pulse as explained in the text. . . . .	31
3.14	$\sigma_{\text{Total}}$ calculated using Equation (3.46) with a pixel pitch of (a) $p = 25 \mu\text{m}$ and (b) $p = 55 \mu\text{m}$ where $s$ is the width of the charge sharing region as shown in Figure 3.13. . .	32
3.15	The hit probability density function for two neighbouring pixels (pixel 0 and pixel 1) considering charge sharing between the two pixels using an analogue readout to acquire the sensor pulse. . . . .	32
4.1	Schematic overview of basic signal flow in a Timepix-like hybrid pixel detector. The energy deposited in the sensor by the incident radiation is converted to an electrical signal. The signal is integrated in the preamplifier, shaped by the pulse shaper and compared to a programmable threshold by the discriminator. The digital part of the readout chip digitises the signal for storage and analysis using counters for timing and energy measurements. . . . .	36
4.2	Schematic overview of the Time-over-threshold (TOT) and Time-of-arrival (TOA) measurements for the Timepix3 readout chips. From [3]. . . . .	37
4.3	(a) Timepix3 chip board and (b) SPIDR readout board (from [3]). . . . .	38
4.4	Spread of pixel responses for the assembly W19_L8 during equalisation for the local threshold set at its minimum value (mask 0000), to its maximum value (mask 1111) and after equalisation. . . . .	39
4.5	(a) An example of a measured S-curve fitted with a sigmoid function and (b) the sigmoid's derivative fitted with a Gaussian function for the assembly W5_E2 using a pulse height of 1000 electrons for the pixel (0, 0) (see the coordinates system in Figure 5.3). This measurement is performed for all the pixels on the diagonal of the matrix for each assembly. . . . .	41
4.6	Threshold calibration for W5_E2. Each point corresponds to the maximum gradient of the S-curve for each pulse height. A linear function as described in Equation (4.3) was used to fit the data points and obtain the parameters $p$ and $q$ . . . . .	42
4.7	Pixel-by-pixel calibration of the TOT for assembly W5_E2 operated at the threshold DACs of (a) THL=1160 (561 electrons) and (b) THL=1190 (878 electrons). . . . .	44

5.1	Energy-loss distribution in (a) 50 $\mu\text{m}$ and (b) 450 $\mu\text{m}$ thick silicon sensors due to the passing of 120 GeV pions ( $\pi^+$ ) comparing the Bichsel model and GEANT4 using the PAI and the emstandard_opt3 physics lists. . . . .	46
5.2	Simulation of the Timepix3 telescope in AllPix with the six tilted telescope planes and the device under test (DUT) in the center as well as particle tracks from the beam entering the telescope from the right. . . . .	47
5.3	The coordinates system for a matrix of $256 \times 256$ pixels. The pixel coordinates (column, row) are shown in black and the local coordinates (x, y) in millimeters of the center of the pixels in the corners of the matrix are shown in blue. In this convention, we are looking from the sensor side with the periphery at the bottom. . . . .	48
5.4	Illustration of the digitisation in a sensor. Each GEANT4 step (G4Step) is shown with a circle. The spread of the arrival position of a charge generated at the steps 1, 2, 3 and 4 is described as a Gaussian distribution with standard deviations $\sigma_1$ , $\sigma_2$ , $\sigma_3$ and $\sigma_4$ . The contribution of the diffusion in the hit and its neighbouring pixels is calculated using Equation (5.1). . . . .	49
5.5	Data reconstruction and analysis workflow using the EUTelescope framework. From [60]. . . . .	51
6.1	The Timepix3 beam reference telescope with six tilted planes for the tracking and the DUT in the middle inserted perpendicular to the beam direction. The telescope planes numbering convention is also shown. . . . .	56
6.2	The Timepix3 beam reference telescope implemented in AllPix with six tilted planes for the tracking and the DUT in the middle inserted perpendicular to the beam direction. The telescope planes numbering convention is also shown in this figure. . . . .	58
6.3	Track angular distribution in GEANT4 simulations due to multiple scatterings between the telescope plane 2 and the DUT obtained by comparing the global MC positions on both planes. . . . .	59
6.4	For the telescope plane 0, the cluster-size distribution in the (a) x direction and (b) y direction. (c) shows the sum of the charge in the cluster in units of TOT. . . . .	59
6.5	The hit residuals of a telescope plane in (a) x and (b) y directions given by comparing the MC and the reconstructed hit positions. . . . .	60
6.6	The hit residuals of the first telescope plane in (a) x and (b) y directions comparing the MC and the reconstructed hit positions as a function of the MC position. . . . .	60
6.7	$\chi^2/\text{NDF}$ distributions for reconstructed telescope tracks for (a) data and (b) simulation. A cut is applied to discard the tracks with $\chi^2/\text{NDF}$ higher than 100 (illustrated with the red line). . . . .	61
6.8	The RMS of the biased residuals $r_b$ in the (a) x and (b) y directions comparing the data and simulation for the telescope planes. A cut is applied to discard the tracks with $\chi^2/\text{NDF}$ higher than 100. . . . .	62
6.9	The track residuals on the DUT comparing the reconstructed track position to the true position of the particles obtained from GEANT4 in AllPix simulations in (a) x and (b) y directions. . . . .	62
6.10	The tracking resolution on the DUT in (a) x and (b) y directions as a function of the MC position. . . . .	63
7.1	TOT distribution for one, two, three and four-pixel clusters for assemblies with (a) 50 $\mu\text{m}$ , (b) 100 $\mu\text{m}$ and (c) 150 $\mu\text{m}$ thick planar sensors. . . . .	66

7.2	Energy deposition distribution for one, two, three and four-pixel clusters for assemblies with (a) 50 $\mu\text{m}$ , (b) 100 $\mu\text{m}$ and (c) 150 $\mu\text{m}$ thick planar sensors. . . . .	67
7.3	The energy deposition for all cluster sizes in simulation and data for (a) 50 $\mu\text{m}$ , (b) 100 $\mu\text{m}$ and (c) 150 $\mu\text{m}$ thick planar sensors. The assemblies are operated at nominal conditions. . . . .	67
7.4	(a) The measured energy deposition distribution in a 150 $\mu\text{m}$ thick silicon sensor (W5_F1) with a bias voltage of -30 V fitted with a Landau function convoluted with a Gaussian function. (b) The most probable value of the measured energy deposition as a function of the bias voltage for W5_F1. Straight lines are used to fit the slope and the plateau regions. The depletion voltage corresponds to the intersection of these two regions and shown in a red dashed line. The continuous red line shows the nominal operating bias voltage. . . . .	68
7.5	The cluster size distribution in simulation and data for 50 $\mu\text{m}$ , 100 $\mu\text{m}$ and 150 $\mu\text{m}$ thick sensors. The assemblies are operated at nominal conditions. . . . .	69
7.6	Cluster-size distribution as a function of (a) bias voltage and (b) threshold for the assembly W5_F1 with a 150 $\mu\text{m}$ thick sensor. . . . .	70
7.7	Cluster-size distribution for data and AllPix simulation as a function of sensor thickness for runs recorded under nominal operating conditions. . . . .	70
7.8	Extrapolated track position within the pixel for 1 to 4-pixel cluster sizes for a 50 $\mu\text{m}$ sensor (assembly W19_G7). The assembly is operated at nominal conditions. . . . .	71
7.9	The residuals for a 50 $\mu\text{m}$ thick sensor (assembly W19_G7) for different cluster sizes: (a) Cluster size 1 ( $1 \times 1$ ), (b) Cluster size 2 ( $2 \times 1$ ), (c) Cluster size 3 ( $2 \times 2$ ) and (d) Cluster size 4 ( $2 \times 2$ ). . . . .	71
7.10	The residual distribution in the x (column) direction in simulation and data for the assemblies (a) W19_G7, (b) W5_E2 and (c) W5_F1. The assemblies are operated at nominal conditions. The histograms are scaled to have unit area. . . . .	72
7.11	The RMS of the residuals in x (column) and y (row) directions as a function of (a) bias voltage and (b) threshold for a 50 $\mu\text{m}$ thick sensor (assembly W19_G7). . . . .	72
7.12	The RMS of the residuals in x and y directions as a function of the sensor thickness for assemblies operated at the nominal condition. The y-axis is zero-suppressed and the deviation between data and simulation is less than 4%. . . . .	73
7.13	(a) Global detection efficiency as a function of the threshold of the readout ASIC for different sensor thicknesses (for the assemblies W19_L8, W5_E2 and W5_F1). (b) focuses on the efficiencies between 95% and 100%. . . . .	74
7.14	(a) Cluster-size distribution and (b) hit residuals, comparing the hit and the MC truth position, for the extrapolation of the simulation to small pixel sizes with a 50 $\mu\text{m}$ thick sensor and a threshold of $\sim 500$ electrons. Binary readout refers to the geometric resolution of pitch/ $\sqrt{12}$ . . . . .	75
8.1	Schematic showing the cross section of a 50 $\mu\text{m}$ thick sensor with active-edge technology. The pixel grid considered in the analysis is indicated with dashed lines. The electric field distribution obtained from a TCAD simulation with a bias voltage of 15 V is also illustrated. (a) does not contain any guard ring (GR) and (b) contains a guard ring at the edge. . . . .	78
8.2	Schematic illustration of the process flow for the fabrication of planar n-in-p active edge sensors by the manufacturer [44]. . . . .	79

8.3	Sensor layouts for different guard-ring solutions for the assemblies described in Table 8.1. (a) shows the convention used in the following sections to express the efficiency and the charge distribution at the edge as a function of the track position. The border of the last pixel before the edge is indicated by a dashed line (at position 0 mm) and the physical sensor edge with a continuous line. . . . .	80
8.4	The different layers in the geometry description used for the sensor production. . . . .	81
8.5	(a) Measured leakage current for active-edge assemblies listed in Table 8.1. For all assemblies, the measurements were done at the room temperature of 22° C. (b) focuses on the breakdown voltage and the leakage current for 50 µm thick sensors. . . . .	83
8.6	Electric field distribution in TCAD simulations for the assemblies listed in Table 8.1. The depletion region is shown with the white line. . . . .	84
8.7	(a) The electric field and (b) the electrostatic potential for nominal bias voltage at a distance of 0.2 µm below the sensor surface. Position 0 µm corresponds to the position of the first pixel. . . . .	85
8.8	Leakage current in TCAD simulations for the pixel cell as a function of bias voltage for (a) 50 µm thick sensors and for (b) assemblies with a grounded guard ring (refer to Table 8.1 for the details on the assemblies). . . . .	85
8.9	Transient simulation of a particle track traversing the sensor with a floating guard ring at a distance of 10 µm from the edge (illustrated as an arrow). The electron density 1 ns after the particle hit is shown. The region shown with a white line is the depletion region. . . . .	86
8.10	The track impact points on the assembly 20-NGR-50: the beam is focused on the edge of the assembly in order to increase the statistics for the edge performance studies. . . . .	87
8.11	The efficiency at the edge as a function of the track positions for the assemblies having a sensor thickness of 50 µm. . . . .	88
8.12	Charge collected as a function of the track position at the edge for the assemblies (a) 20-NGR-50 and (b) 23-FGR-50 in data and TCAD simulations. In data, only tracks within the central 40% of the pixel cell area are considered. . . . .	88
8.13	Charge collected as a function of the track position at the edge for the assemblies (a) 28-GNDGR-50 and (b) 55-GNDGR-50 in data and TCAD simulations. In data, only tracks within the central 7% for 28-GNDGR-50 and 40% for 55-GNDGR-50 of the pixel cell area are considered. . . . .	89
8.14	The electric field and the streamlines distributions for different configurations of guard ring for 50 µm thick sensors. The generated charges follow the streamlines. The depletion region is indicated by solid white lines. . . . .	90
8.15	The efficiency at the edge as a function of the positions for the assemblies having sensors with thicknesses of (a) 100 µm and (b) 150 µm. . . . .	91
8.16	Charge collected as a function of the track position at the edge for the assemblies (a) 55-GNDGR-100 and (b) 55-GNDGR-150 in data and TCAD simulations. In data, only tracks within the central 40% of the pixel cell area are considered. . . . .	91
8.17	The electric field and the streamlines distributions for different configurations of guard ring for 100 µm and 150 µm thick sensors. The generated charges follow the streamlines. The depletion region is indicated by solid white lines. . . . .	92
8.18	The edge efficiency in data as a function of the track position relative to the edge projected in one direction. . . . .	93

A.1	Threshold calibration for the assemblies listed in Table 4.2. Each point corresponds to the maximum gradient of the S-curve for each pulse height. A linear function as described in Equation (4.3) was used to fit the data points and obtain the parameters $p$ and $q$ . . . . .	106
B.1	Biased residual distribution in x-direction obtained in data for each telescope plane. The RMS of the residual is also shown. . . . .	107
B.2	Biased residual distribution in y-direction obtained in data for each telescope plane. The RMS of the residual is also shown. . . . .	108
B.3	Biased residual distribution in x-direction obtained in AllPix simulations for each telescope plane. The RMS of the residual is also shown. . . . .	108
B.4	Biased residual distribution in y-direction obtained in AllPix simulations for each telescope plane. The RMS of the residual is also shown. . . . .	109
C.1	The most probable value of the measured energy deposition as a function of the bias voltage for the assemblies listed in Table 7.1. Straight lines are used to fit the slope and the plateau regions. The depletion voltage corresponds to the intersection of these two regions and shown in a red dashed line. The continuous red line shows the nominal operating bias voltage. . . . .	111
C.2	Cluster size distribution as a function of the applied voltage for assemblies listed in Table 7.1. . . . .	112
C.3	Cluster sizes distribution as a function of the operating threshold for assemblies listed in Table 7.1. . . . .	113
C.4	Extrapolated track position within the pixel for 1 to 4-hit cluster sizes for a 50 $\mu\text{m}$ sensor (assembly W19_G7). The assembly is operated at the nominal conditions. . . . .	114
C.5	Extrapolated track position within the pixel for 1 to 4-hit cluster sizes for a 100 $\mu\text{m}$ sensor (assembly W5_E2). The assembly is operated at the nominal conditions. . . . .	114
C.6	Extrapolated track position within the pixel for 1 to 4-hit cluster sizes for a 150 $\mu\text{m}$ sensor (assembly W5_F1). The assembly is operated at the nominal conditions. . . . .	114
D.1	Doping concentration in TCAD simulations for the assemblies listed in Table 8.1. The region shown with a white line is the depletion region. . . . .	116

# List of Tables

---

2.1	Nominal beam parameters for CLIC at $\sqrt{s} = 3$ TeV and LHC at $\sqrt{s} = 13$ TeV . . . . .	7
2.2	Vertex detector geometries implemented in simulations. . . . .	11
3.1	Summary of the variables used in the Bethe-Bloch formula. From [25]. . . . .	18
3.2	Calculated $\Delta_p$ and $w$ for silicon sensors with various thicknesses using Equations (3.4) to (3.7). . . . .	20
3.3	Parameters for the mobility as described in Equation (3.11) with T the absolute temperature and E the absolute value of the electric field. . . . .	21
4.1	Overview of the main parameters of the Timepix3 readout ASIC. . . . .	36
4.2	Details of different Advacam planar pixel sensors bump-bonded to Timepix3 readout ASICs and studied in calibration and test beams. . . . .	38
4.3	The number of masked pixels after the equalisation and the manual adjustment of the threshold. . . . .	40
4.4	Threshold fit parameters p and q, the operating threshold DAC setting and its conversion into energy deposition. . . . .	43
4.5	Measured baseline mean, threshold DAC step gain, the electronic noise and its conversion into energy deposition. . . . .	43
4.6	DAC settings for the operation and calibration of the Timepix3 assemblies. VFBK is a programmable DAC to determine the baseline voltage of the chip. . . . .	44
6.1	The position of the telescope planes and the DUT along the beam axis. . . . .	56
6.2	The material in each telescope plane contributing to the multiple scatterings of the traversing particles. X refers to the thickness and $X_0$ to the radiation length. . . . .	57
7.1	Nominal operating bias voltage, threshold in DAC and calibrated in number of electrons (measured as described in Section 4.6.1) for the Advacam planar n-in-p assemblies bump bonded to Timepix3 ASICs. . . . .	65
7.2	Measured depletion voltage for the assemblies described in Table 4.2 and calculated by fitting the plateau and slope regions of TOT as a function of the bias voltage. . . . .	68
7.3	Most common cluster shapes. . . . .	69
8.1	Details of different Advacam planar pixel sensors bump-bonded to Timepix3 readout ASICs. The edge distance is defined by the distance between the last pixel implant and the physical sensor edge. . . . .	78
8.2	Layers in the geometry description used for the sensor production (Picture from 23-FGR-50). . . . .	81

- 8.3 The dimensions of the different implants in the sensors listed in Table 8.1. The edge distance is the distance between the last pixel implant to the physical edge of the sensor as illustrated in Figure 8.3(a). The metal width is the diameter of the metal layer for the pixels. The doping width is the diameter of the pixel implant. The contact width is the diameter of the contact between silicon and metal. The GR offset is the distance between the physical edge of the sensor and the implant of the guard ring. GR doping width, contact width and metal with are respectively the width of the implant, the contact and the metal layer for the guard ring. . . . .

81

# Acknowledgements

---

The realisation of the present work has been made possible through valuable assistance, counsels and contributions of experts and collaborators to whom I feel myself obliged to pay my sincere gratitudes.

First of all, I would like to pay my most heartfelt tributes to my professor, Günther Dissertori, for providing me with the opportunity to pursue my PhD studies in physics at the ETH Zürich. I will never forget the unrelenting and precious support, guidance and comments.

My acknowledgement and appreciations go to Dominik Dannheim, as well, who in capacity as my supervisor at CERN, oversaw my work during three years of close collaboration, through exertion of notable care and skill in monitoring the Research Project on the Vertex Detector R&D.

I have to offer my unqualified and heartfelt gratitude to Lucie Linssen, as the group leader of the EP-LCD group, who never hesitated to provide me with excellent and invaluable opportunities to work in her dynamic and creative group at CERN and for her encouragements to pursue and fulfill my PhD studies.

I owe a lot to the EP-LCD group in general for their contribution to my work and also all the memorable time we have shared during gatherings lunches, coffee breaks and social events. More particularly, I express my gratitude to:

- Konrad Elsener for various instructive discussions, support and for reviewing the chapter on the CLIC experiment.
- Andreas Nurnberg, who always was present for providing his counsel and advice and all his help and patience for reading meticulously my thesis and giving me instructive comments and drawing conclusions.
- The Medipix collaboration, especially to Michael Campbell, Xavi Llopart Cudie and Jérôme Alozy for guidance and advice about the Timepix chips.
- Daniel Hynds and Adrian Fiergolski for the various discussions and test-beams we have shared. Edinei Santin, for reviewing the chapter on pixel readout ASICs.
- Mathieu Benoît for leading me to the pixel world through test-beams, TCAD simulations and AllPix simulations.
- Rosa Simoniello, for sharing the office and many discussions.

I would like to thank my friends with whom I have shared great memorable moments and I could count on them for any kind of support. My friends from Lausanne whom I met during my studies at EPFL and we shared many years on the university benches and now we share so many great events. And also to my friends I have met at CERN.

Finally, I would like to thank my amazing family: my parents, Mahmanzar and Behzad, for their unconditional love and support throughout all my life, for all their sacrifices without which I could not imagine where I would be now. My beloved sister and brother, Yassaman and Alireza, for always being present by my side and encouraging me.